Coherent optical & electro-optical signal processor circuit architectures for photonic integration

by
Mehedi Hasan

Thesis submitted to the University of Ottawa
in partial Fulfillment of the requirements for the

Doctor of Philosophy
in Electrical and Computer Engineering

School of Electrical Engineering and Computer Science
Faculty of Engineering
University of Ottawa

Abstract

The capacity of optical communications networks continues to grow unabated. Applications for streaming video, social networking and cloud computing, are driving exponential growth of the traffic carried over the world's ICT networks, which has been sustained thus far through the proliferation of datacenters and efficient, effective use of existing optical fibre. To meet increasing capacity demands requires increasingly sophisticated modulation formats and spectral management to achieve effective use of the available spectrum provided by an optical fibre. Moreover, the technology developed for optical communications is finding broader application to other sectors such as data centres, 5&6 G wireless; lidar and radar.

Ultimately, some essential signal processing functions must occur at speeds beyond purely electronic means even when accounting for anticipated technological development. The option is to perform signal processing in the optical domain. Optical signal processors are fundamentally analog and linear in nature. To provide high performance, an analogue processor must be well controlled in a way analogous to the numerous and sophisticated controllers employed by the process industry. Consequently, a further extension of control to deeper levels within the physical layer reaching the optical layer will be necessary. For example, current reconfigurable optical add-drop multiplexers are coloured and directional and the wavelength division multiplexing channel grid, transponders modulation format, and the routing are all fixed. Through optimization of the interface between the physical components, sensors, and processors elastic optical network technology can be achieved by employing colour-, direction-, contention-, grid-less, filter-, gap-less reconfigurable optical add-drop multiplexers, flexible channels centre frequencies and width, flexible sub-carriers in super-channels, flexible modulation formats and forward error control coding transponders, and impairment-aware wavelength routing and spectral assignment.

The aim of this thesis is to advance the state-of-the-art in photonic circuits and subsystems via proposing new architecture; study of the feasibility of photonic integration and, proof of concept implementations using available resources. The goal is to introduce new architectural concepts that make effective use of physical components and/or optical processors with reduced energy

consumption, reduced footprint and offer speed beyond all-electronic implementations. The thesis presents four case studies based on one or more published papers and supplementary material that advance the goal of the thesis.

The first study presents a coherent electro-optic circuit architecture that generates N spatially distinct phase-correlated harmonically related carriers using a generalized Mach-Zehnder Interferometer with its $N\times1$ combiner replaced by an $N\times N$ optical Discrete Fourier Transform. The architecture subsumes all Mach-Zehnder Interferometer-based architectures in the prior art given an appropriate selection of output port(s) and dimension N, although the principal application envisaged is phase-correlated subcarrier generation for next-generation optical transmission systems. The theoretical prediction is then verified experimentally using laboratory available photonic integrated circuit fabricated for other applications. Later on, a novel extension of the circuit architecture is introduced by replacing the optical Discrete Fourier Transform network using the combination of a properly chosen phase shifter and single MMI coupler. The second study proposes two novel architectures for an on-chip ultra-high-resolution panoramic spectrometer and presents their design, analysis, integration feasibility, and verification by simulation. The target application is to monitor the power of a wavelength division multiplexed signals in both fixed and flex grid over entire C-band with minimum scan time and better than 1 GHz frequency accuracy. The two architectures combine in synchrony a scanning comb filter stage and channelized coarse filter. The fine filtering is obtained using a ring resonator while the coarse filtering is obtained using an arrayed waveguide grating with appropriate configuration. The fully coherent first architecture is optimised for compactness but relies on a repeatable fabrication processes to match the optical path lengths between a Mach-Zehnder interferometer and a multiple input arrayed waveguide grating. The second architecture is less compact than the first but is robust to fabrication tolerances as it does not require the path length matching. The third study proposes a new circuit architecture for single sideband modulation or frequency conversion which employs a cascade Mach-Zehnder modulator architecture departing from the orthodox dual parallel solution. The theoretical analysis shows that the circuit has 3-dB optical and 3-dB electrical advantage over the orthodox solution. The 3-dB electrical advantage increases the linear operating range of Mach-Zehnder modulator before RF amplifier saturation. An experimental verification of the proposed architecture is provided using an available photonic integrated circuit. The proposed circuit can also perform complex modulation. An alternative implementation based on polarization

modulators is also described. The fourth study presents the theoretical modelling of a photonic generation of broadband radio frequency phase shifter. The proposed phase shifter can generate any phase without bound: the complex transmission of the phase shifter follows a trajectory that rotates on a unit circle and may encircle the origin any number of times in either direction, which has great utility in the tuning of RF-photonic systems. The proposed concept is then verified experimentally using off the shelf low frequency electronic components.

“*Recite in the name of your Lord who created; Who taught by the pen; Taught man that which he knew not*”

Acknowledgements

I would like to thank the Almighty who gives me a healthy life and the ability to finish all requirements of my PhD. My heart-felt thanks and greetings to my supervisor, Professor Dr. Trevor Hall, for his continuous support throughout this journey. His support was in a form of a supervisor, sometimes as a mentor, as a guardian and as a friend. Without his continuous guidance this thesis would not have been possible. I have learned from his passion for and dedication to research. His generosity can not be expressed in words. His encouragement and quick response to any problems I have faced; have been a great motivation for me to continue this valuable work. I am lucky to work under such an extremely talented and knowledgeable person's supervision. I must have to admire one thing that, whenever I sent him an email at late night, I received replied even at the weekends; sacrificing his leisure time. Thanks to Mr. Peng Liu for his kind assistance over the past few years, especially his help with experimental work in the lab. I also would like to thank all the administrative staff working at the University of Ottawa and members of my research group and laboratory. I thank all the co-authors who contributed at different stages of this long journey, especially Professor Sophie Larochelle from University of Laval and Professor Karin Hinzer from University of Ottawa. Thank you to all the thesis examiners who have agreed to be part of the committee during this pandemic period. I am grateful to all of you. I am grateful to the Canadian government for not only issuing my study permit and visa in time but also for providing significant amount of research grant in the form of a Vanier scholarship. I am indebted to my dearest wife for inspiring me to undertake higher studies and helping me with taking care of my family, especially my daughter so that I could focus on my study. My beautiful daughter shares the same age as my PhD studies. She patiently waited always while her father studied. Special love for my little princess. Finally, I give a special thanks to my parents who sacrificed much for me throughout my life. I am grateful to them for allowing me to come far away from home for my higher studies and for all the mental support I needed for this long journey. I am indebted to all my relatives and friends for their continuous support, closely or remotely, during my study.

Publications

GRANTED/ FILED PATENT APPLICATION

1. T. Hall, **M. Hasan**, M. Rad, and D. Patrick, "Optical performance monitor," *U.S. patent application* 62/868,450 (June 28, 2019).

PAPERS PUBLISHED, ACCEPTED or SUBMITTED IN REFEREED JOURNALS

1. **M. Hasan** and T. J. Hall, "Photonic generation of broadband RF phase shift with unbound phase trajectory" in preparation.
2. **M. Hasan,** G. M. Hasan, and T. J. Hall, "Experimental realization of a universal RF photonic integrated circuit," in preparation.
3. **M. Hasan**, M. Rad, P. Liu, E. Bernier and T. J. Hall, "Circuit design and integration feasibility of a high-resolution broadband on-chip spectral monitor," submitted to *Opt. Express* (2020).
4. **M. Hasan,** M. Rad, G. M. Hasan, P. Liu, P. Dumais, E. Bernier and T. J. Hall, "Ultra-high resolution wideband On-chip spectrometer," *IEEE Photonics J.* 12, 1-17 (2020).
5. **M. Hasan**, O. Jafari, X. Guan, L. A. Rusch, S. Larochelle, and T. J. Hall, "Experimental demonstration of SSB modulation/ frequency conversion using cascaded silicon MZM" *IEEE Photo. Technol. Lett.* 32 (18), 1147-1150 (2020).
6. **M. Hasan** and T. J. Hall, "Complex modulation using tandem polarization modulators," *J. Mod. Optics* 64(20), 2268-2272 (2017).
7. **M. Hasan**, J. Hu, H. Nikkah and T. J. Hall, "A photonic circuit for complementary frequency shifting, in-phase quadrature/single sideband modulation and frequency multiplication: analysis and integration feasibility," *J. Mod. Optics* 64 (14), 1386-1397 (2017).
8. T. J. Hall and **M. Hasan**, "Universal discrete Fourier optics RF photonic integrated circuit architecture," *Opt. Express* 24(7),7600-7610 (2016).
9. **M. Hasan** and T. Hall, "Cascade photonic integrated circuit architecture for electro-optic I-Q / SSB modulation or frequency conversion," *Opt. Lett.* 40(21), 5038-5041 (2015).

PAPERS PUBLISHED AND ACCEPTED IN REFEREED CONFERENCES

1. **M. Hasan**, M. Rad, G. M. Hasan, H. Ghorbani, P. Liu, P. Dumais, E. Bernier and T. J. Hall, "Circuit architecture and integration feasibility of a high-resolution broadband on-chip spectral sensor," Advanced Photonic Congress, OSA, Montreal, Canada, (2020), SpM3I.1.
2. **M. Hasan**, D. Sun, P. Liu and T. J. Hall, "Towards a universal RF photonic integrated circuit architecture for microwave applications," 37th Progress in Electromagnetics Research Symposium (PIERS), Shanghai, China 8-11 August (2016).
3. T. J. Hall and **M. Hasan**, "Universal photonic integrated circuit architecture: The discrete Fourier Transform case," 2016 Photonics North (PN), Quebec City, QC, 2016, pp. 1-1.

Acronyms

AI	Artificial Intelligence
AOM	Acousto Optic Modulator
AO-OFDM	All Optical Orthogonal Frequency Division Multiplexing
AWG	Arrayed Waveguide Gratings
BER	Bit-Error-Rate
CMOS	Complementary Metal-Oxide-Semiconductor
CW	Continuous Wave
DAC	Digital to Analog Convertor
DC	Direct Current
DD-MZM	Dual-Drive Mach-Zehnder Modulator
DP-MZM	Dual-Parallel Mach-Zehnder Modulator
DFB	Distributed Feedback Laser
DFT	Discrete-Fourier Transform
EAM	Electro-Absorption Modulator
EG	Echelle Gratings
EON	Elastic Optical Network
E/O	Electrical to Optical
FBG	Fibre Bragg Grating
FFT	Fast-Fourier Transform
FSR	Free Spectral Range
FWHM	Full Width Half Maximum
GMZI	Generalized Mach-Zehnder Interferometer
I	In-Phase
IMD	Intermodulation Distortion
LASER	Light Amplification by Stimulated Emission of Radiation
LSB	Lower Sideband
MATP	Maximum Transmission Point
MITP	Minimum Transmission Point
MMI	Multimode Interference

MPW	Multi Project Wafer
MZDI	Mach-Zehnder Delay Interferometer
MZI	Mach-Zehnder Interferometer
MZM	Mach-Zehnder Modulator
OFDM	Orthogonal Frequency Division Multiplexing
OPM	Optical Performance Monitoring
OSA	Optical Spectrum Analyzer
OSNR	Optical Signal-to-Noise Ratio
PAM	Pulse-Amplitude Modulation
PM	Phase Modulator
PP	Push-Pull
Q	Quadrature
QTP	Quadrature Transmission Point
QWP	Quarter Wave Plate
RR	Ring Resonator
SDN	Software Defined Networking
SSB	Single-Sideband Modulation
SSB-SC	Single-Sideband Suppressed Modulation
TE	Transverse Electric
TM	Transverse Magnetic
USB	Upper Sideband
WDM	Wavelength-Division Multiplexing

Table of Contents

CHAPTER 1

Introduction

1.1 Background and motivation

Information and Communications Technology (ICT), including optical communications, high performance computing and wireless access are creating an interconnected global society. Applications like streaming video (e.g. Netflix), social networking (e.g. Facebook) and cloud computing (e.g. Amazon Web Services, Dropbox) are driving exponential growth of the traffic carried over the world's ICT networks. Breakthrough technology is required to serve an increasing number of users with ever-increased bandwidth demands while limiting energy consumption. The industry now talks of Pbit/s capacity optical networks. The first concern of industry is the cost of hardware, yet energy consumption has risen to second place, and the key to both cost and energy reduction is photonic integration.

Software-defined networking (SDN) and emerging elastic optical network (EON) technologies are key technology enablers for next-generation networks. SDN allows programmability of network functions and protocols. EON allows the allocation of an arbitrary and appropriate spectral range and advanced modulation format to an optical path according to application bandwidth and quality of service requirements taking into account optical physical layer attributes such as impairments. Network operators have embraced the SDN paradigm with enthusiasm motivated by its potential to commoditize hardware amongst other factors. However, the current optical transport network (OTN) is opaque to the control plane and as such is a major impediment to the full deployment of SDN. An SDN/EON OTN is required that calls for integrated photonics where all components are controlled by software.

5G wireless and optical communications are converging in terms of technology and methods. Spectrally efficient advanced modulation formats long used in wireless to relieve a crowded RF spectrum are now being used in coherent optical communications systems to relieve what has now become a similarly crowded optical spectrum. Similarly, RF-photonic methods for the generation and modulation of millimeter wave carriers, their (de-) modulation, and distribution are envisaged to support 10 Gbit/s data rates necessary for large file download and the use of a high density of

antennas with multiple-in multiple-out signal processing for good coverage. RF photonic systems have been implemented until recently using fibre-coupled discrete components but considerations of stability, compactness, and cost calls for integrated photonics.

With the transition from incoherent to coherent optical systems a revolution is consequently in progress in both optical and wireless communication technology. At long last, rather than field intensity, information is now conveyed by the amplitudes of the components of the vector field (polarisation, magnitude and phase). It is theoretically possible to construct a coherent optical circuit with sufficient versatility to implement any possible linear operation. This follows because any loss-less linear optical circuit is described by a unitary transformation, and a specific array of basic two-mode transformations is mathematically sufficient to implement any unitary transformation [1]. Many advanced optical functions, including fundamental tests of quantum mechanics and quantum technologies; and arbitrary linear optical processors for communications could be implemented using meshes of Mach–Zehnder interferometers [2].

Ironically, the physical layer functions required by optical communications networks are more easily expressed but far more challenging to implement within a coherent optical rather than an incoherent optical conceptual framework. The reason is the extreme short wavelength of light (~1 μm), which demands path length tolerances in the region of ~ 1 nm if the phase is to be controlled within a complex circuit architecture; performance can be severely degraded by small imperfections of optical components. Fortunately, another revolution in optical component technology is in progress with a transition from discrete components interconnected by optical fibre to integrated components interconnected by planar optical waveguides within a photonic integrated circuit (PIC). Photonic integration brings tight dimensional tolerances and, more significantly, extremely tight relative dimensional tolerances. The latter enables circuit designers to ameliorate impairments by making use of component symmetries that are robust to PIC fabrication errors but impractical with discrete components. Moreover, methodologies for trimming circuit parameters to achieve perfect optics with imperfect components are emerging [3]. The research will focus on photonic circuits and subsystems that leverage continued advances in photonic integrated circuits including hybrid integration of active optoelectronic, electro-optic, and electronic devices, and related advances in algorithms for signal processing and control. The goal is to advance the state of the art through the proposal and exploration of novel circuit or system

architectures that offer speed beyond all-electronic implementations, substantially reduced energy consumption, and/or reduced footprint with the potential for commercialization.

1.2 Objectives

The specific objectives are:

- to demonstrate new programmable discrete-space optical processor architectural and device concepts amenable to photonic integration for next generation optical communications and microwave-photonics functions.
- to develop the design of a technologically viable compact on-chip high-resolution wideband spectrometer to measure the spectral profile of WDM signals accurately in flex- and fixed- grid architectures across the entire C-band 1530 nm-1565 nm aiming at sub-GHz resolution bandwidth.
- to develop energy efficient circuit architecture for complex modulation and/or frequency shifting operation.
- to develop broadband RF phase shifter using photonic technology.

The thesis plan envisages chapters based on either papers that have been published or manuscripts planned for publication. The contributions of the research described has made to the advancement of the research goal outlined in the preceding is detailed in the following sections.

1.2.1 Photonic processor architecture

Meshes of Mach–Zehnder interferometers (MZI) feature widely in the field of radio frequency (RF) photonics. There has been a plethora of publications [4-9] over the last decade that have described essentially the same Generalized Mach-Zehnder Interferometer (GMZI) circuit architecture: a $1 \times N$ splitter directly interconnected to a $N \times 1$ combiner via an array of N electro-optic $LiNbO_3$-based phase modulators, each circuit adapted to particular design goals. The applications have generally been to; in- and quadrature- (IQ) phase modulation, single sideband modulation, electro-optic frequency up-conversion [4-7]; radio frequency (RF) multiplication [8-9]; and multiple carrier generation [10]. The difference between the circuits proposed have largely concerned variations of the static optical and electrical phase shifts required or the implementation of an equivalent circuit using standard Mach-Zehnder modulators (MZM) rather than individual phase-modulators (PM) as the basic building brick. A generalized design methodology that

determines the parameters of the architecture required to meet specified design objectives such as the suppression of unwanted intermodulation products has been reported in [11]. It has also been shown [12-13], how to use the intrinsic phase relations between the ports of splitters and combiners and specifically multi-mode interference (MMI) couplers to implement the static optical phase shifts required by these circuits, thereby avoiding the need to apply static DC bias to the electro-optic modulators and the associated drift issues that otherwise require complex stabilization circuitry. This thesis describes and analyses a coherent electro-optic circuit architecture that generates *N* spatially distinct phase-correlated harmonically related carriers using a GMZI with its $N \times 1$ combiner replaced by an $N \times N$ optical Discrete Fourier Transform (DFT). Advantage may be taken of the tight optical path-length control, component and circuit symmetries and emerging trimming algorithms offered by photonic integration. The architecture subsumes all MZI-based architectures in the prior art given an appropriate choice of output port(s) and dimension N although the principal application envisaged is phase correlated subcarrier generation for next generation optical transmission systems beyond 1Terabit / second using all optical orthogonal frequency division multiplexing.

Super-channel transmission has already been reported experimentally [14-18] to facilitate high data rates. One common demerit in these demonstrations is that all subcarriers exit from the same port by means of optical comb generation. Hence, an optical de-multiplexing filter is needed to separate these subcarriers individually so that they can be modulated. However, the limited tuning range and temperature sensitivity of an optical de-multiplexing filter makes the system implementation complicated and reduces the system performance. The design of a complementary frequency shifter capable of generating two spatially separated subcarriers has been reported [10] but, with ever increasing demand for bandwidth, a circuit design capable of generating more than two spatially separated subcarriers is required for near future optical systems.

This thesis considered the acousto-optic diffraction in the Raman-Nath regime within the framework of classical Fourier optics to provide the intuition of the proposed architecture. This motivates a discretization that replaces the acousto-optic modulator by a set of waveguide phase-modulators excited by a waveguide splitter; electrically driven from the same RF source but with a progressive phase increment; and with light from their egress port processed by an optical DFT network. A transfer matrix analysis of this architecture then shows that it operates as expected with carriers with frequency shift $q\omega_{RF}$ emitted from output port q modulo N. The options for the

implementation of the DFT network are considered and a specific example based on MMIs elaborated for $N = 4$. The analysis is then verified by simulation both in the ideal case and in the presence of impairments. A similar optical processor may be applied at the receiver to demodulate super channels before coherent detection. The thesis also explains how the architecture can be understood as a discretization of a classical free-space optical information processing system. Later on, a novel extension of the circuit architecture has also been introduced, by replacing the 4×4 optical Discrete Fourier Transform (DFT) network using the combination of a properly chosen phase shifter and single 4×4 MMI coupler. An integrated circuit based on silicon photonics technology readily available in the laboratory is used for experimental confirmation.

1.2.2 Design and integration feasibility of a high-resolution broadband spectrometer

In an optical network, optical performance monitoring (OPM) is the key enabling technology for reliable spectrum management. Up-to-date network telemetry is required for capacity scaling, network or component fault recovery, and network reconfiguration through performance prediction and planning. The monitoring includes information on bit-error-rate (BER), optical signal-to-noise ratio (OSNR), electrical signal-to-noise ratio (ESNR), loss, power, etc. The monitoring information is then fed to the network management agent for resource optimization to maximize the reach versus rate. In practice, optical performance monitoring may be based on the measurement of one or several parameters. However, OPM is used herein to refer to "power" monitoring since power is one of the key indicators of performance in optical systems.

In transport optics, especially in WDM networks, spectral sensing is not straightforward. Traditionally WDM channels are distributed over the 40 nm wide fibre-optic C-band (1530 nm to 1570 nm) with fixed centre frequencies arranged on the ITU grid at intervals of 50 GHz or 100 GHz. and an OPM card is used to measure the power. The working principle of the OPM card involves sweeping a tunable filter with 50 GHz resolution over the spectrum to make available ITU grid channel power readings. Due to their excessive power consumption, size and cost, OPM cards are deployed at few points in the network; typically co-located with reconfigurable add-drop multiplexers (ROADMs). However, current optical networks are elastic in nature, i.e. the channels are not located on a fixed regular grid, rather the channel center wavelength can be placed at an arbitrary location within the spectrum. The flexible grid can support a variety of channel power profiles (i.e., bandwidth and power spectral density) with a resolution of channel centre frequency

placement as fine as 6.25 GHz. Flex-ready spectrum measurements are required to facilitate the deployment of the flex-grid system. As a result, flex-grid ready ROADM architectures are equipped with new modules that can measure power at desired frequency location and resolution. However, due to cost issues, spectrum measurement is only performed at add-drop nodes and not at amplifier nodes. Moreover, a single OPM module is shared by the multi degree-ROADM so the OPM measurement speed reduces as the number of lines it supports increases. Consequently, the performance of WDM channels in a section (ROADM-to-ROADM) is modeled based on an analytical or a semi-analytical analysis or a machine learning approach. The absence of OPM makes it difficult to have live and accurate network measurement; and hence hard to implement performance optimization. Complete knowledge of spectral content in a network is prerequisite for the effective use of color-, direction-, contention-, grid-, filter-, gap-less ROADM, flexible modulation formats, flexible channels frequencies and spectral assignment.

A large variety of on-chip spectrometer designs have been unveiled and realized over the past decade such as cascaded ring resonator (RR) arrayed waveguide grating (AWG) architecture [19-20], dispersive configurations (arrayed waveguide gratings (AWG) [21], echelle gratings (EG) [21-22] or cascaded micro-ring resonators [23-24], cascaded Mach-Zehnder interferometer (MZI) based processor [25]; and discrete Fourier transform infrared spectroscopy [26-27]. In [19] the authors propose a combined architecture where the ring and AWGs need to be tuned to match the ring response with the AWG center wavelength. Depending on the number of channels, fixed grid reading of the spectrum is achieved. Similar to the previous prior art the authors of [20] proposed a cascaded architecture where a ring resonator (RR) is followed by a parallel pair of arrayed waveguide gratings (AWG) with different center wavelengths to reduce the cross talk. The center wavelength of the AWGs must differ by half a channel spacing for proper operation but there is no mention of if and how the whole spectrum may be scanned. When the RR is not tuned to an AWG channel passband center, the spectrometer will suffer increased insertion loss and channel leakage (cross talk) with increased detuning. In addition to that, EG and AWGs have been proposed by Xiang et al. [21] to construct spectrometers capable of operation over a broad range of different wavelength. The resolution is restricted by the number of samples of the spectrum by the fixed number of EG/AWG channels. The minimum resolution bandwidths obtained is 1.6 nm (~100 GHz). A finer resolution of 0.496 nm with an adjacent channel cross talk of -18 dB is obtained by a similar configuration disclosed in reference [22] using an EG with integrated metal

semiconductor metal (MSM) photodiode. A multiple ring resonator in cascade architecture has been proposed in [23-24] for high resolution spectrum measurement. These architectures have proven to be extremely complicated to control and calibrate in a reliable fashion due to the fact that two or more very sensitive components (RR) are needed to be tuned together. An array of 84 microdonut resonators are integrated to cover 50 nm bandwidth with a minimum resolution of 0.6 nm. The outer radii of the resonator require careful variation with a step size of 1 nm [23]. Multiple ring resonator in cascaded is presented in [24]. On the other hand, in [25] a fast-Fourier transformation (FFT)-like approach is used by performing multiple measurements of the filtered spectrum. The authors demonstrate a resolution of 23 pm (~ 2.9 GHz) over a 184 pm range about 1550 nm using eight parallel MZI. Sub-GHz resolution seems to be within reach but entire C band coverage remains challenging as it requires multiple arms which imposes significant loss, complex control and measurement dynamics. Following a similar approach, Kita *et al*. [26] proposed a new signal processing technique performed electro-optically where a combination of numerous measurements with data processing provides the desired high-resolution power measurement across a desired band. To achieve sub-GHz resolution more than 10 stages are needed. Reference [27] discloses a digital Fourier Transform infra-red (dFTIR) spectroscopy approach with a cascade of 10 electro-optic switches in between carefully dimensioned waveguide segments, which in principle can lead to a sub-GHz resolution. However, the scaling and control of the architecture is complicated when high resolution sensing is required over a wide band. Therefore, this strategy and architecture suffers similarly in scaling when high resolution spectrum sensing over a wide band is needed. In summary, the existing measurement technologies fail to combine acceptable resolutions with wideband operation and do not support feasible integration with other products which limits their deployment mainly due to high cost, loss and foot print. In addition, the requirement of sub-GHz resolution bandwidth to reliably and accurately distinguish the individual carriers in a densely packed multi-carrier super-channels or to monitor the differential power of adjacent channels in fixed and flex-grid architectures with a large free-spectral range for transparent operation across the entire C band 1530 nm-1565 nm for an integrated solution remains challenging.

In this thesis, the design of a technologically viable compact on-chip high-resolution wideband spectrometer is presented and verified by software simulation using an industry standard tool. A novel and original approach to coordinated tuning of the individual stages enables the spectrometer

to scan the entire C-band with better than 1 GHz resolution using only three stages and two controls. The target application is to measure the spectral profile of WDM signals accurately in flex- and fixed- grid architectures across the entire C-band 1530 nm-1565 nm with minimum scan time and better than 1 GHz frequency accuracy. The photonic integration of the circuit architecture can be implemented using a mature fabrication technology; low index contrast Silica on Silica or CMOS compatible low loss Si_3N_4 photonic integration platform. However, to meet the technical specifications such as compact size and high-resolution bandwidth, the Si_3N_4 platform is preferred due to its impressive agreement between simulation and practical measurement for the components used in this design architecture [28-31]. For effective use of resources, the fabrication plan envisaged access to multi-project wafer MPW runs for test structures followed by a custom wafer run for fabrication of prototypes for demonstration. The LioniX Triplex technology chosen only offers MPW runs for designs using the asymmetric double strip (ADS) waveguide and the low-cost photolithography used has a minimum feature size of 1 um. Accordingly, the simulations of the components and sub-circuits that constitute the proposed spectrometer are designed using ADS as reference waveguide. The proposed circuit architecture consists of three stages. The first stage is a ring resonator (RR) which has the function of defining the spectrometer resolution. It provides a periodic train of resonances spaced by its free-spectral range (FSR). It is tuneable in frequency over one FSR. The final stage is an arrayed waveguide grating (AWG) which has the function of isolating one RR resonance in each output channel. The output channel frequency spacing is equal to the FSR of the RR. The principal innovation is ganged tuning of the RR and AWG to retain the RR resonance at the center of the AWG channel passband. This is achieved by a second stage that uses an MZDI with FSR equal to the AWG channel spacing to form a coherent superposition of two interleaved AWG channel spectra corresponding to a pair of input ports.

An alternative architecture is also conceived as a refinement of the previously proposed design. The coherent superposition of a pair of AWG input channels is replaced by the incoherent superposition of pairs of AWG outputs, which may perform processing the measured AWG channel powers. The MZI stage is eliminated, releasing the spectrometer from any requirement to control inter-stage optical path lengths and thereby significantly easing manufacture. The details of the circuit architecture design, modelling and integration feasibility is also presented in this thesis. The architecture combines a RR and a number N of AWG with interleaved channel spectra. For the purpose of exposition, the $N = 2$ case is first considered but subsequently generalised.

Hardware economies may be made by replacing the multiple AWGs by a single time multiplexed N-input AWG. The $N = 3$ architecture has particular merit as the first to offer near zero adjacent channel crosstalk. In order to meet the specification (high resolution bandwidth) of the proposed spectrometer, the CMOS compatible Si_3N_4 photonic integration platform has been selected as it offers low loss, tight confinement, low dispersion and a mature thermo-optic phase shifter technology. The detail simulation verification of the proposed architecture is presented using components (RR and AWG) designed for fabrication. A combination of industry standard software tool is used for the component design. A simple but novel signal processing approach enables the spectrometer to scan the entire C-band with high resolution (~1GHz) using only one dynamic control. The original signal processing techniques make the proposed architecture robust to fabrication tolerances.

1.2.3 Energy efficient single sideband modulation/complex modulation

Electro-optic in-phase–quadrature (I-Q) modulation or single side-band (SSB) modulation or frequency conversion are functions ('the desired function') fundamental to radio frequency photonic systems. To the best of the authors' knowledge, an integrated SSB modulator based on a Ti-diffused $LiNbO_3$ optical waveguide circuit driven by an in-phase and quadrature signal at 2 GHz. was reported for the first time in 1981 [4]. The circuit configuration used is same as the dual-parallel Mach-Zehnder modulator (DP-MZM) used today. Since then, there has been a plethora of publications [5-7,12-13, 32-36] describing different techniques of achieving the desired function. In [32-34] the desired function is achieved by electro-optic amplitude modulation of an optical carrier. A custom electro-absorption modulator (EAM), driven by a mm-wave RF source, is used to externally amplitude-modulate a distributed feedback laser (DFB) and an optical filter (for example, a fiber-Bragg grating (FBG)) is used to extract a single side-band. The conversion efficiency is low, which reduces receiver sensitivity. Moreover, the EAM, DFB laser, and FBG must be very closely matched in frequency of operation that entails temperature control, which is undesirable in terms of energy consumption. Alternatively, the desired function is achieved by electro-optic phase-modulation of an optical carrier. Typically, pairs of phase modulators are combined to form Mach-Zehnder modulators (MZM), which are used to amplitude-modulate the in-phase (I) and quadrature (Q) components of the optical carrier. Circuit architectures using a dual-drive MZM (DD-MZM) [5, 35-36], two DD-MZM [6] and a DP-MZM [7] have been

investigated. To minimize trimming, it is advantageous in integrated circuits to exploit phase shifts that are intrinsic to the topology of the optical and electrical waveguides (and, hence, are broadband and temperature insensitive), such as, the phase relations between the ports of splitters and combiners and, more generally, the ports of multi-mode interference couplers (MMI).The use of the intrinsic phase relationship between ports of a MMI coupler has been proposed to improve the linearity of an electro-optic modulator by selective suppression of unwanted inter-modulation products [37-38]. A requirement for precise RF-drive level, static DC bias of the electro-optic modulators, and/or passive phase shift elements are common features of most designs. A notable advance, reported in [12-13], are DC bias-less and filter-less architectures with no requirement to set a precise electrical drive level. Most reported architectures [1, 5-13] are directly equivalent to single stage generalized Mach-Zehnder Interferometer (GMZI) circuit: a $1 \times N$ splitter directly interconnected to a $N \times 1$ combiner via an array of N linear electro-optic phase modulators. The universally accepted solution is the use of a Dual-parallel Mach-Zehnder modulator (DP-MZM) solution. Few two-stage architectures have been reported and, to the best of authors' knowledge, none reported capable of the desired function; only architectures useful for frequency-multiplication are known in the prior art [39]. The search for a two-stage architecture capable of the desired function was motivated by the authors' finding, reported in [40], that a two-stage MZM architecture for frequency multiplication required 3 dB less RF-drive power than its functionally equivalent GMZI architecture. As far as the authors are aware, a two-stage MZM capable of performing the desired function is reported for the first time in this thesis. The proposed design has 3 dB RF and 3 dB optical conversion gain advantage compared to a single stage circuit, for example, a DP-MZM. The experimental verification of the proposed concept is also presented using a prototype cascaded MZM architecture on a silicon photonics. The adapted circuit is a three-stage cascaded MZM architecture was designed to be used as an optical digital-to-analog converter for high baud rate PAM transmission. The details of the fabrication technology of the silicon photonic chip and the electrode electro-optic (E/O) characterization can be found in [41]. Achieving the correct quiescent operating point experimentally is complicated by imbalance of the optical path lengths in the different stages of the test architecture and other impairments due to fabrication errors. Nevertheless, thermo-optic phase shifters are present in every stage for appropriate phase tuning. Firstly, a DC characterization was performed with the assistance of the algorithm presented by Wilkes et al [42]. They formed an interferometer consisting of a cascade

of two Mach-Zehnder modulators; one of which plays the role of a variable beam splitter. Using Miller's algorithm to adjust the variable beam splitter they achieved a – 60 dB extinction ratio limited only by the number of bits of the DAC used to provide the bias voltage. In our case, using the algorithm, the extinction ratio at the upper output port is maximized to greater than 40-dB. The lower port extinction is improved similarly. Following the achievement of this bias state, an additional optical bias is applied as per the conceived theoretical model. An alternative implementation based on polarization modulators is also reported in this thesis.

1.2.4 Photonic generation of broadband RF phase shifter

A precise and broadband radio frequency (RF) phase shifter is needed in a variety of applications including phased array antenna systems to support high speed wireless communication and radar; and self interference cancellation (SIC) systems in a full duplex technology to improve the attainable spectral efficiency of a 5G network. The photonic generation of microwave phase shifts is receiving significant attention due to its simplicity, light weight, low cost, small size and broadband operation with minimal phase errors. The underlying principle is based on frequency shifting an optical carrier via single side band suppressed carrier (SSB-SC) modulation using RF carrier of interest followed by the re-insertion of a copy of the original optical carrier that is shifted in phase by a variety of means such as an optical phase modulator based on p-n junction devices; z-cut lithium niobate (LiNbO3); or a polarization controller within a number of different circuit architectures [43-50].

In reference [43] an optical carrier is divided in to two paths, one used to generate SSB-SC modulation, while the other path is phase shifted using an optical phase modulator. Both the paths are then combined on a photodiode to generate the phase shifted RF signal. A similar strategy to obtain the phase shift is followed in references [44-45] using a dual-polarization dual-parallel Mach Zehnder Modulator (DP-MZM); in which one DP-MZM generates the SSB-SC modulation while the other DP-MZM is biased at maximum transmission point to maximize the output power of the carrier. The outputs of the both DP-MZM are then combined using a polarization beam combiner (PBC). The relative phase of the orthogonally polarised optical carrier and sideband is then adjusted by a polarization dependent optical phase shifter (OPS) [44] or a combination of polarization controller and polarizer [45]. A DP-MZM based scheme is presented in [46-49]. In [46], one child MZM is biased at the minimum transmission point (MITP) and driven by an RF

signal, thereby generating double sideband suppress carrier (DSB-SC) modulation; while the other child MZM is biased at the MATP to pass the carrier. The two outputs are combined by using an optical coupler [47]. The optical phase shift is applied by tuning the phase adjust voltage of the parent MZM. Finally, an optical bandpass filter (OBF) is used to suppress one of the sidebands. A similar method is described in [47] except the combining is done through a PBC and the optical phase shift is implemented using polarization dependent OPS. Reference [48] describes a DP-MZM based scheme capable of a 360˚-degree phase shift founded on the precise settings of the phase and amplitude of the optical carrier and two sidebands using predetermined modulator bias voltages. An architecture consisting of, two parallel MZM driven by in-phase and quadrature phase RF signal modulate orthogonally polarised optical carriers combined on a photodiode is demonstrated in [49]. The slope about the operating point of the two MZM is varied by adjustment of their respective DC bias voltage, thereby the sign and magnitude of the in-phase and quadrature phase modulation components is adjusted resulting in the phase shift of the superimposed components. For proper operation of the scheme, the modulation depth should be small which leads to high insertion loss and careful adjustment of the two bias voltages is required as, for a constant magnitude RF output, both bias voltages depend on the desired phase shift. A photonic integrated phase shifter based on silicon-on-insulator technology is presented in [50]. A single side band (SSB) full carrier modulation is generated using a DP-MZM. An optical deinterleaver filter is used to separate the optical carrier and the sideband. The phase of the isolated carrier is then shifted by using a p-n junction based optical phase shifter and combined with the sideband on a photodiode. All these methods require either an optical deinterleaver filter or optical bandpass filter, precise control of the polarization and/or polarizer, bias voltages or suffers from lack of phase shift linearity and range. Moreover, the need for a continuous phase shift range extending beyond 360˚ degree is gaining appreciation. For an example, improved robustness to loss of lock of an optoelectronic oscillator has been demonstrated by enlarging the RF tuning phase shift ranges from 350˚ degrees to 1160˚ degree using a frequency conversion pair [51]. A circuit architecture based on two parallel DP-MZM circuit that requires no additional control or filter for proper operation is proposed in the thesis. Furthermore, the linearity of the phase shifter remains valid for wide range of frequencies. The proposed phase shifter can generate any phase without bound. Actually, the complex transmission of the phase shifter follows a trajectory that rotates on a unit circle in either direction. The practical implementation of the proposed design can be demonstrated

using a commercially available dual polarization quadrature phase shift keying (DP-QPSK) modulator. Due to unavailability of a-QPSK modulator, experimental verification by an electronic emulation of the proposed concept is presented in this thesis using off the shelf components.

CHAPTER 2

Universal RF photonic circuit architecture

2.1 Summary

There has been a plethora of publications over the last decade on the subject of electro-optic circuit architectures for RF signal generation. These circuits may be understood as a Generalized Mach-Zehnder Interferometer (GMZI) circuit architecture with as many arms containing phase modulators as there are distinct paths through the circuit studied: a $1 \times N$ splitter directly interconnected to a $N \times 1$ combiner via an array of N electro-optic $LiNbO_3$-based phase modulators where N is the number of distinct paths through the structure studied. It was observed that there existed an essential unity of these architectures. This chapter describes and analyses a coherent electro-optic circuit architecture that generates N spatially distinct phase-correlated harmonically related carriers using a GMZI with its $N \times 1$ combiner replaced by an $N \times N$ optical Discrete Fourier Transform (DFT). The architecture subsumes all MZI-based architectures in the prior art given an appropriate selection of output port(s) and dimension N, although the principal application envisaged is phase-correlated subcarrier generation for next-generation optical transmission systems. For simplicity, the simulation of a 4×4 DFT realized by a combination of 180° optical hybrids implemented as 2×2 MMI couplers. A novel extension of the circuit architecture is also presented, by replacing the 4×4 optical Discrete Fourier Transform (DFT) network using a combination of a properly chosen phase shifters and a single 4×4 MMI coupler. Furthermore, the experimental validation of a 4×4 universal RF photonic circuit architecture is presented using photonic integrated circuit (PIC) readily available in the laboratory which was fabricated for another application.

2.2 Contribution

Part of the theoretical modelling and simulation verification provided in this chapter was published as a seminal paper in *Optics Express*. I performed the simulation verification, processed the results and wrote part of the manuscripts. Dr. Hall conceived the initial theory and wrote other parts of the manuscript. I conceived the theory of realizing $N \times N$ DFT circuit using $N \times N$ MMI with combination of predefined phase shifts. I wrote the manuscript and Dr. Hall revised it. It was

published as conference proceedings in *Progress in Electromagnetic Research Symposium*. Another manuscript demonstrating the experimental findings has been prepared for submission to *Optics Communication*. I designed the experiment, completed the measurement, and wrote the manuscript. Dr. Hall edited the manuscript. Mr. Gazi Hasan contributed to the input/output coupling of the experiment and data recording.

2.3 Article

This section is a reproduction of articles published (Optics Express) and submitted (Optics Express) for publication.

T. J. Hall and **M. Hasan**, "Universal discrete Fourier optics RF photonic integrated circuit architecture," *Optics Express* 24(7),7600-7610 (2016).

M. Hasan, D. Sun, P. Liu and T. J. Hall, "Towards a universal RF photonic integrated circuit architecture for microwave applications," *37th Progress in Electromagnetics Research Symposium (PIERS)*, Shanghai, China 8-11 August (2016).

The submitted manuscript follows verbatim [54].

M. Hasan, G. M. Hasan and T. J. Hall, "Experimental realization of a universal RF photonic integrated circuit," submitted to *Optics Communication* (2020).

Universal discrete Fourier optics RF photonic integrated circuit architecture

Trevor J. Hall and Mehedi Hasan*

Photonic Technology Laboratory, Centre for Research in Photonics, Advanced Research Complex, University of Ottawa, 25 Templeton Street, Ottawa, K1N 6N5, ON, Canada

Abstract: This paper describes a coherent electro-optic circuit architecture that generates a frequency comb consisting of N spatially separated orders using a generalised Mach-Zenhder interferometer (MZI) with its $N\times1$ combiner replaced by an optical $N\times N$ Discrete Fourier Transform (DFT). Advantage may be taken of the tight optical path-length control, component and circuit symmetries and emerging trimming algorithms offered by photonic integration in any platform that offers linear electro-optic phase modulation such as $LiNbO_3$, silicon, III-V or hybrid technology. The circuit architecture subsumes all MZI-based RF photonic circuit architectures in the prior art given an appropriate choice of output port(s) and dimension N although the principal application envisaged is phase correlated subcarrier generation for all optical orthogonal frequency division multiplexing. A transfer matrix approach is used to model the operation of the architecture. The predictions of the model are validated by simulations performed using an industry standard software tool. Implementation is found to be practical.

References and links

1. M. Reck, A. Zeilinger, H. J. Bernstein, and P. Bertani, "Experimental realization of any discrete unitary operator," Phys. Rev. Lett. **73**, 58-61 (1994).
2. J. Carolan, C. Harrold, C. Sparrow, E. Martín-López, N. J. Russell, J. W. Silverstone, P. J. Shadbolt, N. Matsuda, M. Oguma, M. Itoh, G. D. Marshall, M. G. Thompson, J. C. F. Matthews, T. Hashimoto, J. L. O'Brien, and A. Laing, "Universal linear optics," Science 349, 711-716 (2015).
3. D. A. B. Miller, "Perfect optics with imperfect components," Optica 2, 747-750 (2015).
4. M. Izutsu, S. Shikama, T. Sueta, "Integrated optical SSB modulator / frequency shifter," IEEE J. Quantm Electron. 17, 2225-2227 (1981).
5. G. H. Smith, D. Novak, and Z. Ahmed, "Overcoming chromatic-dispersion effects in fiber-wireless systems incorporating external modulators," IEEE Trans. Microwave Theory Tech. 45, 1410-1415 (1997).
6. A. Wen, M. Li, L. Shang, and Y. Chen, "A novel optical SSB modulation scheme with interfering harmonics suppressed for ROF transmission link," Opt. Laser Technol. 43, 1061-1064 (2011).
7. C. W. Chow, C. H. Wang, C. H. Yeh, and S. Chi, "Analysis of the carrier-suppressed single-sideband modulators used to mitigate Rayleigh backscattering in carrier-distributed PON," Opt. Express 19, 10973-10978 (2011).
8. M. Hasan, R. Maldonado-Basilio, T. J. Hall, "Comments on X. Yin, A. Wen, Y. Chen, and T. Wang, "Studies in an optical millimeter-wave generation scheme via two parallel dual-parallel Mach-Zehnder modulators," J. Mod. Opt. 62, 581-583 (2015).
9. P.-T. Shih, J. Chen, C.-T. Lin, W.-J. Jiang, H.-S. Huang, P.-C. Peng, and S. Chi, "Optical millimeter-wave signal generation via frequency 12-tupling," J. Lightwave Technol. 28, 71-78 (2010).
10. H. Yamazaki, T. Saida, T. Goh S. Mino, M. Nagatani, H. Nosaka, K. Murata, "Dual-carrier dual-polarization IQ modulator using a complementary frequency shifter," IEEE J. Sel. Top. Quantum Electron. 19, 3400208 (2013).
11. R. Maldonado-Basilio, M. Hasan, R. Guemri, F. Lucarz, and T. J. Hall, "Generalized Mach–Zehnder interferometer architectures for radio frequency translation and multiplication: suppression of unwanted harmonics by design," Opt. Comm. **354**, 122-127 (2015).
12. M. Hasan, R. Maldonado-Basilio, and T. J. Hall, "A dual-function photonic integrated circuit for frequency octo-tupling or single-side-band modulation," Opt. Lett. 40, 2501-2504 (2015).
13. R. Maldonado-Basilio, M. Hasan, H, Nikkhah, S. Abdul-Majid, R. Gumeri, F. Lucarz, J. Tocnaye, and T. J. Hall, "Electro optic up-conversion mixer amenable to photonic integration," J. Mod. Opt. 62, 1405-1411 (2015).
14. Y. Ma, Q. Yang, Y. Tang, S. Chen, and W. Shieh, "1-Tb/s single-channel coherent optical OFDM transmission over 600-km SSMF fiber with subwavelength bandwidth access," Opt. Express 17, 9421-9427 (2009).
15. K. Takiguchi, and T. Miwa, "Integrated-optic OFDM signal multiplexer composed of optical IFFT circuit," Electron. Lett. 51, 505-506 (2015).
16. K. Takiguchi, M. Oguma, H. Takahashi and A. Mori, "Integrated-optic eight-channel OFDM demultiplexer and its demonstration with 160 Gbit/s signal reception," Electron. Lett. 46, 575-576 (2010).
17. K. Takiguchi, T. Kitoh, A. Mori, M. Oguma, and H. Takahashi, "Integrated-optic OFDM demultiplexer using slab star coupler based optical DFT circuit," 36th European Conference and Exhibition on Optical Communication (ECOC), Torino, 2010, pp. 1-3.
18. W. Li, X. Liang, W. Ma, T. Zhou, B. Huang, and D. Liu, "A planar waveguide optical discrete Fourier transformer design for 160 Gb/s all-optical OFDM systems," Opt. Fiber Technol. 16, 5-11 (2010).

19. A G Kirk, A K Powell, and T J Hall, “A generalisation of the error diffusion method for binary computer generated hologram design,” Opt. Comm. **92**, 12-18 (1992).
20. A. E. Siegman, “Fiber Fourier optics,” Opt. Lett. 26, 1215-1217 (2001).
21. M. E. Marhic, “Discrete Fourier transforms by single-mode star networks,” Opt. Lett. 12, 63-65 (1987).
22. G. Cincotti, “Generalized fiber Fourier optics,” Opt. Lett. 36, 2321-2323 (2011).
23. G. Cincotti, “What else can an AWG do?,” Opt. Express 20, B288 (2012).
24. J. Zhou, “All-optical discrete Fourier transform based on multimode interference couplers,” IEEE Photonics Technol. Lett. 22, 1093-1095 (2010).
25. J. Zhou, “Realization of discrete Fourier transform and inverse discrete Fourier transform on one single multimode interference coupler,” IEEE Photonics Technol. Lett. 23, 302-304 (2011).
26. D. A. B. Miller, “Perfect optics with imperfect components Perfect optics with imperfect components: supplementary material,” http://dx.doi.org/10.1364/optica.2.000747.s001.
27. S. Abdul-Majid, R. Maldonado-Basilio, C. Lei, H. Awad, I. Hasan, W. N. Ye, and T. J. Hall, “Performance analysis of a photonic integrated interferometer circuit based on silicon-on-insulator,” Opt. Quantum Electron. 47, 1965-1971 (2015).
28. M. Hasan, R. Maldonado-Basilio, F. Lucarz, J-L de Bougrenet and T. J. Hall, “Photonic integrated circuit for frequency 8- and 24-tupled millimeter wave signal generation”, Opt. Lett. 39, 6950-6953 (2014).
29. R. Halir, P. J. Bock, P. Cheben, A. Ortega-Monux, C. Alonso-Ramos, J. H. Schmid, J. Lapointe, D. Xu, J. G. Wanguemert-Perez, I Molina-Fernandez, and S. Janz, “Waveguide sub-wavelength structures: a review of principles and applications,” Laser Photonics Rev. 9, 25-49 (2015).
30. A. Natarajan, A. Komijani, X. Guan, A. Babakhani, and A. Hajimiri, “A 77-GHz phased-array transceiver with on-chip antennas in silicon: transmitter and local LO-path phase shifting,” IEEE J. Solid-State Circuits 41, 2807-2819 (2006).
31. A. Chiba, T. Kawanishi, T. Sakamoto, K. Higuma, K. Takada, and M. Izutsu, “Low-crosstalk balanced bridge interferometric-type optical switch for optical signal routing,” IEEE J. Sel. Top. Quantum Electron. 19, 3400307 (2013).
32. D. Marpaung C. Roeloffzen, R. Heideman, A. Leinse, S. Sales, and J. Capmanyet, “Integrated microwave photonics,” Laser Photonics Rev. 7, 506-538 (2013).
33. R. Slavík, S. G. Farwell, M. J. Wale, and D. J. Richardson, "Compact Optical Comb Generator Using InP Tunable Laser and Push-Pull Modulator," IEEE Photonics Technol. Lett. 27, 217-220, (2014).
34. H. Subbaraman, X. Xu, A. Hosseini, X. Zhang, Y. Zhang, D. Kwong, and R. T. Chen "Recent advances in silicon-based passive and active optical interconnects," Optics Express 23, 2487-2511 (2015).
35. X. Zhang, B. Lee, C. Lin, A. X. Wang, A. Hosseini, and R. T. Chen "Highly Linear Broadband Optical Modulator Based on Electro-Optic Polymer," IEEE Photonics Journal 4, 2214-2228 (2012).
36. P. Rabiei, J. Ma, S. Khan, J. Chiles, and S. Fathpour, "Heterogeneous lithium niobate photonics on silicon substrates," Opt. Express 21, 25573-25581 (2013).
37. W. H. P. Pernice, C. Xiong, F. J. Walker, and H. X. Tan, “Design of a silicon integrated electro-optic modulator using ferroelectric BaTiO3 films,” IEEE Photonics Technol. Lett. 26, 1344-1347 (2014).
38. J. Li, Z. Liu, Y. Tu, S-T. Ho, I W. Jung, L. E. Ocola, and B. W. Wessels, “Photonic crystal waveguide electro-optic modulator with a wide bandwidth,” J. Lightwave Technol. 31, 1601-1607 (2013).
39. D. Korn, R. Palmer, H. Yu, P. C. Schindler, L. Alloatti, M. Baier, R. Schmogrow, W. Bogaerts, S. K. Selvaraja, G. Lepage, M. Pantouvaki, J. M. D. Wouters, P. Verheyen, J. V. Campenhout, B. Chen, R. Baets, P. Absil, R. Dinu, C. Koos, W. Freude, and J. Leuthold, “Silicon-organic hybrid (SOH) IQ modulator using the linear electro-optic effect for transmitting 16 QAM at 112 Gbit/s,” Opt. Express 21, 13219-13227 (2013).
40. M. J. R. Heck, J. F. Bauters, M. L. Davenport, J. K. Doylend, S. Jain, G. Kurczveil, S. Srinivasan, Y. Tang, and J. E. Bowers, “Hybrid silicon photonic integrated circuit technology,” IEEE J. Sel. Top. Quantum Electron. 19, 6100117 (2013).
41. J. W. Goodman, Introduction to Fourier Optics, 3rd Edition (Roberts & Company Publishers, 2005).

1. Introduction

With the transition from incoherent to coherent optical systems a revolution in optical communications technology is in progress. At long last, rather than field intensity, information is now conveyed by the amplitudes of the components of the vector field (polarisation, magnitude and phase). It is theoretically possible to construct a coherent optical circuit with sufficient versatility to implement any possible linear operation. This follows because any loss-less linear optical circuit is described by a unitary operator, and a specific array of basic two-mode operations is mathematically sufficient to implement any unitary operator [1]. Many advanced optical functions, including fundamental tests of quantum mechanics and quantum technologies; and arbitrary linear optical processors for communications could be implemented using meshes of Mach–Zehnder interferometers [2]. Ironically, the physical layer functions required by optical communications networks are more easily expressed but far more challenging to implement within a coherent optical rather than an incoherent optical conceptual framework. The reason is the extreme short wavelength of light (~1 μm), which demands path length tolerances in the region of ~ 1 nm if the phase is to be controlled within a complex circuit architecture; performance can be severely degraded by small imperfections of optical components. Fortunately, another revolution in optical component technology is in progress with a transition from discrete components interconnected by optical fibre to integrated components interconnected by planar optical waveguides within a photonic integrated circuit. Integration brings tight dimensional tolerances and, more significantly, extremely tight relative dimensional tolerances. The latter enables circuit designers to ameliorate impairments by making use of component symmetries that are robust to photonic integrated circuit fabrication errors but impractical with discrete

components. Moreover, methodologies for trimming circuit parameters to achieve perfect optics with imperfect components are emerging [3].

Meshes of Mach–Zehnder interferometers (MZI) feature widely in the field of radio frequency (RF) photonics. There has been a plethora of publications [4-9] over the last decade that have described essentially the same Generalized Mach-Zehnder Interferometer (GMZI) circuit architecture: a $1 \times N$ splitter directly interconnected to a $N \times 1$ combiner via an array of N electro-optic $LiNbO_3$-based phase modulators, each circuit adapted to particular design goals. The applications have generally been to; in- and quadrature- (IQ) phase modulation, single sideband modulation, electro-optic frequency up-conversion [4-7]; radio frequency (RF) multiplication [8-9]; and multiple carrier generation [10]. The difference between the circuits proposed have largely concerned variations of the static optical and electrical phase shifts required or the implementation of an equivalent circuit using standard Mach-Zehnder modulators (MZM) rather than individual phase-modulators (PM) as the basic building brick. A generalized design methodology that determines the parameters of the architecture required to meet specified design objectives such as the suppression of unwanted intermodulation products has been reported in [11]. It has also been shown [12-13], how to use the intrinsic phase relations between the ports of splitters and combiners and specifically multi-mode interference (MMI) couplers to implement the static optical phase shifts required by these circuits, thereby avoiding the need to apply static DC bias to the electro-optic modulators and the associated drift issues that otherwise require complex stabilization circuitry. This paper describes and analyses a coherent electro-optic circuit architecture that generates N spatially distinct phase-correlated harmonically related carriers using a GMZI with its $N \times 1$ combiner replaced by an $N \times N$ optical Discrete Fourier Transform (DFT). Advantage may be taken of the tight optical path-length control, component and circuit symmetries and emerging trimming algorithms offered by photonic integration. The architecture subsumes all MZI-based architectures in the prior art given an appropriate choice of output port(s) and dimension N although the principal application envisaged is phase correlated subcarrier generation for next generation optical transmission systems beyond 1Terabit / second using all optical orthogonal frequency division multiplexing.

Super-channel transmission has already been reported experimentally [14-18] to facilitate high data rates. One common demerit in these demonstrations is that all subcarriers exit from the same port by means of optical comb generation. Hence, an optical de-multiplexing filter is needed to separate these subcarriers individually so that they can be modulated. However, the limited tuning range and temperature sensitivity of an optical de-multiplexing filter makes the system implementation complicated and reduces the system performance. The design of a complementary frequency shifter capable of generating two spatially separated subcarriers has been reported [10] but, with ever increasing demand for bandwidth, a circuit design capable of generating more than two spatially separated subcarriers is required for near future optical systems.

The paper is organized as follows. First, to provide intuition, acousto-optic diffraction in the Raman-Nath regime is considered within the framework of classical Fourier optics. This motivates a discretization that replaces the acousto-optic modulator by a set of waveguide phase-modulators excited by a waveguide splitter; electrically driven from the same RF source but with a progressive phase increment; and with light from their egress port processed by an optical DFT network. A transfer matrix analysis of this architecture then shows that it operates as expected with carriers with frequency shift $q\omega_{RF}$ emitted from output port q modulo N. The options for the implementation of the DFT network are considered and a specific example based on MMIs elaborated for $N = 4$. Layout considerations result in re-ordering and consolidation of elements that can remove any obvious connection to a travelling phase modulation wave and Fresnel diffraction. The analysis is then verified by simulation both in the ideal case and in the presence of impairments. The paper closes with a discussion of implementation feasibility and a summary of the main results.

2. Classical Raman-Nath diffraction

As a consequence of Fresnel diffraction, an ideal thin lens forms, in its real focal plane, the Fourier transform of the field in its front focal plane. A point source, represented by a Dirac delta distribution at the origin of the front focal plane, is thereby transformed to a constant amplitude field in the real focal plane. Hence, in Fig. 1, the spherical wave emanating from the point source at the origin in the front focal plane of lens L_1 is collimated into a plane wave propagating along the optical axis to provide a uniform amplitude field in its rear focal plane. Similarly, lens L_2 forms, in its rear focal plane, the Fourier transform of the field in its front focal plane. Consequently, the Fourier transform of the field transmitted by the acousto-optic modulator (AOM) is formed at the screen. In the absence of the AOM, lenses L_1 and L_2 ideally form a stigmatic image of the point source on the screen. In practice, the ideal image is convolved by a point-spread function caused by the finite apertures of the system's components. An acoustic wave induces within the aperture of the AOM a travelling phase grating via the elasto-optic effect. In the Raman-Nath regime the AOM behaves as a thin transmittance and the image on the screen splits into multiple diffraction orders.

The optical field a at the exit of the AOM due to a plane acoustic wave propagating in the x-direction transverse to the optical axis is given by:

$$a(x) = exp[\, i\eta\, cos(\, \Omega t - Kx)]. \tag{1}$$

where $\eta = \Delta nkl$ is the peak optical phase change caused by the peak refractive index change Δn induced by the acoustic wave via the elasto-optic effect, $k = 2\pi/\lambda$ is the vacuum optical wavenumber, λ is the vacuum optical wavelength, l is the acousto-optic interaction length, Ω is the frequency of the acoustic wave $K = 2\pi/\Lambda$ is the acoustic wavenumber, Λ is the acoustic wavelength, and t is time. Invoking the Jacobi-Angier expansion:

$$\exp(i\eta\, cos\theta) = \sum_{q=-\infty}^{\infty} i^q J_q(\eta) \exp\,(iq\theta) \tag{2}$$

yields:

$$a(x) = \sum_{q=-\infty}^{\infty} i^q J_q(\eta)\, \exp[iq(\Omega t - Kx)] \tag{3}$$

where J_q is the Bessel function of the first kind of order q. The lens L_2 forms, in its rear focal plane, the Fourier transform $\hat{a}$ of the field a in its front focal plane:

$$\hat{a} = \frac{1}{2\pi} \int_{-\infty}^{\infty} a(x)\, exp(\, - i\xi x) dx. \tag{4}$$

where the spatial frequency variable ξ is mapped into a transverse spatial co-ordinate by the optical system. Performing the Fourier transform one obtains an infinite train of Dirac distributions located at $\xi = -qK$ with mass $i^q J_q(\eta) exp(iq\Omega t)$:

$$\hat{a}(x) = \sum_{q=-\infty}^{\infty} i^q J_q(\eta)\, \exp(iq\Omega t)\, \delta\, (\xi + qK) \tag{5}$$

This is the familiar Raman-Nath diffraction pattern with the temporal frequency of each order Doppler shifted by qΩ The different temporal frequency components of the field are thereby spatially separated. Suppose, rather than plane wave-illumination, multiple beamlets (for example generated by a Fourier array generator [19]) sample the travelling phase grating on a regular lattice with period Λ/N then the spatial spectrum is replicated on a regular lattice with lattice constant NK. The Raman-Nath orders are thereby superimposed into equivalence classes corresponding to order q modulo N. A single period of the spectral orders is then related to a single period of the sampled phase grating by a DFT.

2.1 Discrete Raman-Nath diffraction

Pursuing the observation in the preceding section, consider the circuit shown in Fig. 2 consisting of a $1 \times N$ uniform light splitter that excites an array of N identical electro-optic waveguide phase modulators with outputs combined by a passive coherent optical network that emits light from its output ports with complex amplitudes b_q equal to the DFT of the complex amplitudes a_p of the light entering its input ports, where p and q are integers that index the ports:

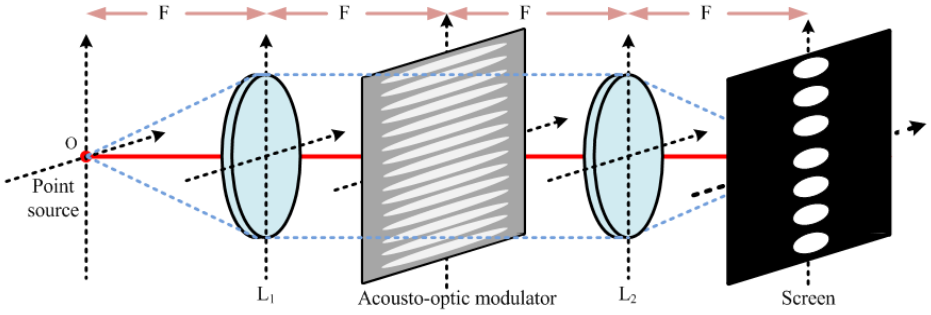

Fig. 1. A classical free-space coherent optical system for the observation of continuous Raman-Nath diffraction. Lens L_1 provides the acousto-optic modulator with uniform collimated illumination. The acousto-optic modulator (AOM) generates a travelling refractive index wave within its aperture. Lens L_2 provides the Fourier transform of the light transmitted by the AOM at the screen where Raman-Nath diffraction orders are observed.

$$b_q = \frac{1}{\sqrt{N}} \sum_{p=0}^{N-1} a_p \, exp(-ipq \frac{2\pi}{N}) \tag{6}$$

Let each phase modulator be driven by an RF source of angular frequency Ω with a progressive phase shift with increment $2\pi/N$:

$$v_p = v_{RF} \, cos[\Omega t + p(\frac{2\pi}{N})] \tag{7}$$

For light of unit amplitude at the input of the splitter, the complex amplitude a_p of the light exiting the phase modulators is:

$$a_p = \frac{1}{\sqrt{N}} exp(i\pi \frac{v_p}{v_\pi})$$

$$= \frac{1}{\sqrt{N}} exp(i\pi \frac{v_{RF}}{v_\pi}) \, cos[\Omega t + p(\frac{2\pi}{N})] \tag{8}$$

where v_π is the half-wave voltage.

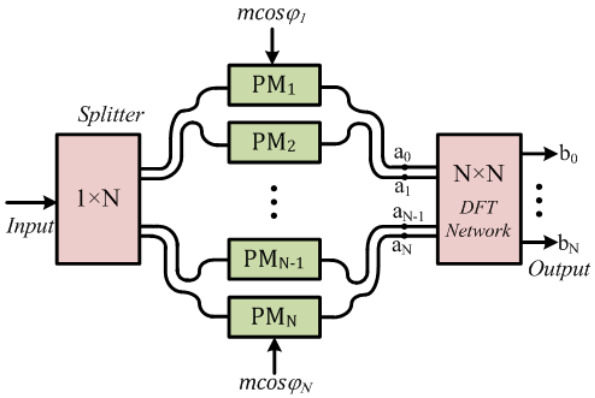

Fig. 2. Schematic diagram of an array of N phase modulators in parallel between a $1 \times N$ splitter and $N \times N$ DFT network. PM: phase modulator; DFT: discrete Fourier transform.

The output of the waveguide phase modulators may be interpreted as the discrete-space samples at $x = -pd$ of a single period of the continuous travelling phase function defined by Eq. (1) with a peak phase shift given by:

$$\eta = \pi \frac{v_{RF}}{v_\pi} \tag{9}$$

and a spatial frequency of the periodic extension of a single period of the samples given by:

$$K = \frac{2\pi}{\Lambda}; \qquad \Lambda = Nd \tag{10}$$

where d is the sampling interval.

Substituting Eq. (8) into Eq. (6) and invoking the Jacobi-Angier expansion Eq. (2) yields:

$$b_q = \frac{1}{N} \sum_{p=0}^{N-1} \sum_{r=-\infty}^{\infty} i^r J_r(\eta) \exp(ir\Omega t) \exp\,[ip(r-q)\,2\pi/N] \tag{11}$$

Re-ordering the summations to give:

$$b_q = \sum_{r=-\infty}^{\infty} i^r J_r(\eta) \exp(ir\Omega t) \; \frac{1}{\sqrt{N}} \sum_{p=0}^{N-1} \exp\,[ip(r-q)p\,2\pi/N] \tag{12}$$

and noting:

$$\frac{1}{\sqrt{N}}\sum_{p=0}^{N-1} exp[\,i(r-q)p\frac{2\pi}{N}] = 0 \qquad r \neq q \qquad mod \qquad N$$

$$\frac{1}{\sqrt{N}}\sum_{p=0}^{N-1} exp[\,i(r-q)p\frac{2\pi}{N}] = 1 \qquad r = q \qquad mod \qquad N \tag{13}$$

yields the final result:

$$b_q = \sum_{s=-\infty}^{\infty} i^{(q+sN)} J_{(q+sN)} \exp\,[i(q+sN)\Omega t] \tag{14}$$

It can be observed that all carriers of order q modulo N exit output port q as anticipated in the preceding section. The operation of the circuit architecture in Fig. 2 may therefore be understood in terms of discretized Raman-Nath diffraction. The circuit architecture subsumes the RF photonic circuits in the prior art for radio frequency (RF) multiplication; in- and quadrature- (IQ-) phase modulation / single sideband modulation / electro-optic frequency up-conversion; and frequency comb-generation given an appropriate choice of output port(s) and phase-modulator dimension N as is listed in Table I.

Table 1. Circuit Architecture Configurations

Function	Dimension	Port(s) used
IQ modulation, SSB & electro-optic frequency conversion	$N = 4$	q = 1 or N-1
$\times N$ RF frequency multiplication	$N = 2q$	q
Spatially separated carrier generation	N = desired number of carriers	all

3. Discrete Fourier optics

It is well established that a suitable combination of waveguides and couplers may implement an optical DFT. The foundation of discrete Fourier optics was established by a pioneering paper in which Siegman proposed [20] a simple optical scheme previously also reported by Marhic [21], to perform the DFT of a parallel input signal using only passive couplers and phase shifters. Following the Cooley-Tukey algorithm, the $N \times N$ DFT is recursively decomposed into $log2(N)$ stages of 2×2 DFT elements in parallel that are realized by 180^o optical hybrids implemented as 2×2 couplers. Subsequently, Cincotti [22] proposed a decomposition into larger dimension $M \times M$ DFT elements that are realized by $(360/M)°$ optical hybrids. This is advantageous in reducing the wiring complexity and the number of waveguides cross-overs. The DFT elements may be implemented using star-couplers [23] or multimode interference (MMI) couplers augmented by static phase shift elements [24, 25]. It is possible to implement any linear transformation including the DFT using a mesh of Mach-Zehnder Interferometers (MZI) [26]. Star-couplers and MMI depend upon Fresnel diffraction in 'free-space' slab waveguide regions that is sampled at its boundaries by single-mode planar waveguides. Networks that employ these components retain a connection to classical Fourier optics that becomes tenuous when only directional couplers are used. For illustrative purposes, a 4×4 DFT realized using 2×2 MMI is considered in this paper. Figure 3(a) shows a network that performs a 4×4 DFT composed of four $180°$-optical hybrids described by the transfer matrix:

$$S = \frac{1}{\sqrt{2}}\begin{pmatrix} 1 & 1 \\ 1 & -1 \end{pmatrix}.$$

and a $\pi/2$ phase shift element described by the transfer function:

$$Z^{-1} = \exp\,(^{-i\pi}/_{2})$$

A 2×2 MMI 3dB coupler is described by the transfer matrix:

$$S_{MMI} = \frac{1}{\sqrt{2}}\begin{pmatrix} 1 & -i \\ -i & 1 \end{pmatrix} = \frac{1}{\sqrt{2}}\begin{pmatrix} 1 & 0 \\ 0 & -i \end{pmatrix}\begin{pmatrix} 1 & 1 \\ 1 & -1 \end{pmatrix}\begin{pmatrix} 1 & 0 \\ 0 & -i \end{pmatrix}.$$

Hence:

$$S = -\begin{pmatrix} -i & 0 \\ 0 & 1 \end{pmatrix} S_{MMI} \begin{pmatrix} -i & 0 \\ 0 & 1 \end{pmatrix}.$$

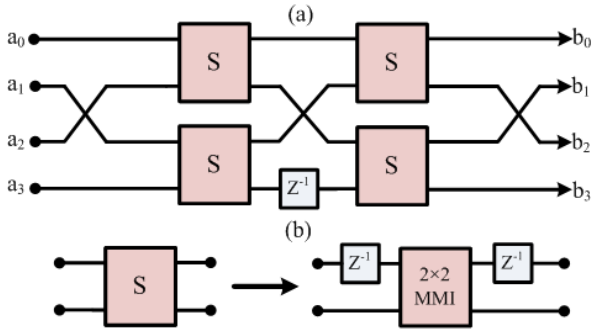

Fig. 3. (a) Schematic of a 4×4 DFT network; (b) realisation of S using a 2×2 MMI.

Consequently, up to a sign, the 180°-optical hybrids may be replaced by 2×2 MMI 3dB couplers with a $\pi/2$ phase shift element connected to its upper input and output port as shown in Fig. 3(b). Performing this substitution and eliminating any constant overall phase shifts yields the network shown in Fig. 4(a). The phase shift blocks at the front-end of the DFT network may be moved into the respective arm of the phase modulator array and placed at the front. The analysis in the preceding assumed that the $1 \times N$ input splitter generated light at its egress ports of equal magnitude and phase. This may be achieved using a tree of 1×2 symmetric splitters. The cross-over at the front-end of the DFT network as shown in Fig. 4(a), may be removed by reordering the phase-modulators. This re-ordering has the effect of grouping the phase modulators into differentially driven pairs that form two Mach-Zehnder interferometers (MZI) statically biased by the phase-shift elements. The latter may be absorbed by replacing the 1×2 symmetric splitters on the egress side of the splitter tree by 2×2 MMI 3dB couplers. Moreover, in most applications the spatial location and absolute phase of an output is irrelevant which permits the cross-over and two delay elements on the output side of the DFT network to be removed. The final result is shown in Fig. 4(b).

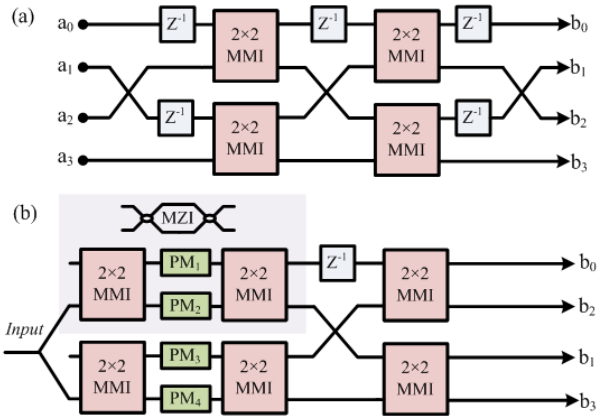

Fig. 4. (a) Schematic of a 4×4 DFT network using 2×2 MMI; (b) schematic of the complete circuit. The y-branch at the input represents a 1×2 symmetric coupler.

4. Verification

The correct operation of the circuit is verified by simulation using an industry standard software tool (VPIphotonics). A continuous wave DFB laser set to operate at a vacuum wavelength 1550 nm with a power of 10 mW is used as an

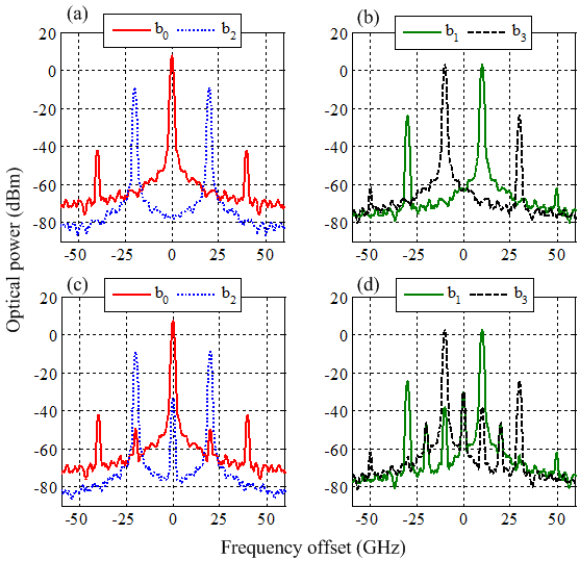

Fig. 5. Simulated optical spectrum, (a)-(b) without considering MMI errors due to fabrication tolerances; (c)-(d) with fabrication tolerances. A resolution bandwidth of 1 GHz is used for the optical spectrum analyzer. The optical noise floor is determined by the laser line-width, which is considered 200 kHz in this simulation.

optical source. A 10 GHz RF source generating peak amplitude of $v_{RF} = 0.25v_{\pi}$ and an appropriate phase shift is applied to the phase modulators. Figs. 5(a) & (b) show the optical spectrum predicted by the simulation which verifies the theoretical predictions. The correct function of the circuit may deviate from ideal because of power imbalances and phase error between the ports of MMI due to fabrication errors and errors in the path length of the electrical waveguides that connects the RF source and phase modulator electrodes. It can be assumed that all the components in a circuit will suffer similar impairments.

To account for the MMI tolerances, the S-matrix of an ideal MMI is perturbed to have 1° phase error and 0.70% power imbalances (well above simulated errors [27]) between the output ports and loaded for all the MMIs present in the circuit. The resultant optical spectra are shown in Figs. 5(c) & (d). Carrier break-through can be observed in the spectrum, thus limiting the overall performance. Nevertheless, a minimum sub-harmonic suppression ratio (SHSR) of 24 dB and above can be achieved. It has been reported [28] that performance degrades more when RF drive phase error is considered as the RF phase error for a harmonic is a multiple equal to its order of the RF-drive phase error. Figure 6 shows the calculated SHSR for different phase error between the MZMs. It shows that other than the output at port b_0, all remain constant. A minimum SHSR of 24 dB and above is achieved. The optical phase errors can be reduced substantially over a broader bandwidth compared to a conventional MMI by the use of a sub-wavelength

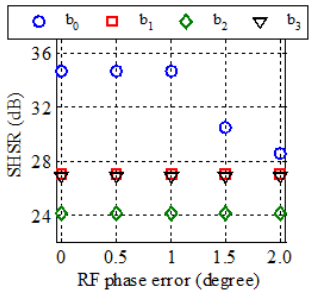

Fig. 6. Optical SHSR as a function of RF drive's phase errors between the MZMs.

engineered MMI [29]. A linear summing amplifier can combine in-phase and quadrature phase RF signals to produce any desired RF phase shift and a CMOS implementation has been demonstrated operating at 77 GHz [30]. Co-integration of these RF phase-shifters with the optical circuitry will also avoid electrical phase shift errors and facilitates programmability and electrical trimming.

If required, additional small Mach-Zehnder interferometers may be integrated within the circuit to facilitate optical trimming [31] to improve the performance further, for example, by pursuing the ideas of Miller [3].The proposed circuit architecture may be implemented in any photonic integration platform [32] that can offer a linear electro-optic modulator. As many as 20 $LiNbO_3$ phase modulators hybridized to silica on silicon photonic light circuits by butt coupling have been demonstrated [10]. Continuous advances in performance of modulators based on InP [33], silicon [34], polymer [35]; and progress on hybrid integration of $LiNbO_3$ [36], $BaTi0_3$ [37-38], organic [39] thin-film electro-optic materials and III-V active devices [40] on silicon-on-insulator augurs very well that implementation is practical.

5. Conclusions

A coherent electro-optic circuit architecture that generates a frequency comb consisting of N spatially separated orders has been described. Intuition is provided by the space discretization of classical Raman-Nath diffraction. The circuit consists of a $1 \times N$ splitter that feeds light into a parallel array of electro-optic phase modulators each driven from the same RF source with a progressive phase shift with increment $2\pi/N$ with their phase modulated optical outputs processed by an $N \times N$ optical DFT. The circuit is not limited to a DFT and any linear optical transformation may be substituted. Advantage may be taken of the tight optical path-length control, component and circuit symmetries and emerging trimming algorithms offered by photonic integration in any platform with a linear electro-optic phase modulator. The circuit subsumes many prior RF photonic circuit architectures given an appropriate choice of output port(s) and dimension N, although the principal application envisaged is phase correlated subcarrier generation. The predictions of a transfer matrix model of the circuit operation are validated by simulations performed using an industry standard software tool. Implementation is found to be practical. This suggests that free-space optical information processing systems [41] demonstrated in the past may find renewed application in discrete space form.

Acknowledgments

The authors acknowledge the Natural Sciences and Engineering Research Council of Canada (NSERC) for their support through a Strategic Project Grant STPGP 430176-12. Trevor J. Hall is grateful to the Canada Research Chair (CRC) Program for their support of his CRC-I in Photonic Network Technology.

Towards a Universal RF Photonic Integrated Circuit Architecture for Microwave Applications

Mehedi Hasan, DeGui Sun, Peng Liu, and Trevor J. Hall
Photonic Technology Laboratory, University of Ottawa, *25 Templeton Street, Ottawa, K1N 6N5, ON, Canada*

Abstract

There has been a plethora of publications over the last decade that have described essentially the same Generalized Mach-Zehnder Interferometer (GMZI) circuit architecture: a $1 \times N$ splitter directly interconnected to a $N \times 1$ combiner via an array of N electro-optic $LiNbO_3$-based phase modulators, each circuit adapted to particular design goals. This paper introduces a novel extension of the circuit architecture that subsumes all these MZI circuits in the prior art by replacing the $N \times 1$ combiner of a GMZI-based architecture by an $N \times N$ optical Discrete Fourier Transform (DFT) network to generate a frequency comb with regularly spaced harmonics of frequency $q\omega_{RF}$ where ω_{RF} is the frequency of the RF drive signal applied to the phase modulators. All harmonic orders equivalent modulo N to the output port number p exit that port. As the circuit generates N spatially separated phase correlated subcarriers, it can be used to provide multi-carriers for transmission formats such as orthogonal frequency division multiplexing (OFDM) that will enable the satisfaction of the terabit data rate demands anticipated in the near future. The proposed circuit can be implemented practically in any material platform that offers linear electro-optic phase modulators.

Introduction

In the field of microwave photonics, there has been a plethora of publications that describe the application of Mach-Zehnder interferometer (MZI) based RF photonic circuits that are all equivalent to the same generalized Mach-Zehnder interferometer (GMZI) circuit architecture: a $1 \times N$ splitter directly interconnected to a $N \times 1$ combiner via an array of N electro-optic (typically, $LiNbO_3$-based) phase modulators. Depending on the setting of circuit parameters (dimension, static optical & electrical phase-shifts) various useful functions have been demonstrated, including radio frequency (RF) multiplication [1-2], electro-optic frequency up-conversion [3], single side band (SSB) modulation or in- and quadrature- (IQ) phase modulation [4] and complementary frequency shifting [5]. A generalized design methodology that specifies the architecture required to meet specified design objectives such as the suppression of unwanted intermodulation products has been reported in [6]. The study of an optical Discrete Fourier Transform (DFT) used as the combiner of a GMZI circuit was reported for the first time in [7]. The envisaged application is subcarrier generation for next generation optical transmission systems at 1 Terabit / second using an all optical orthogonal frequency division multiplexing (AO-OFDM) technique. Super-channel transmission has already been reported experimentally [8-11] to facilitate high data rates. One common demerit of all these demonstrations is that all subcarriers generated by an optical comb source, output from the same port. Hence, an optical de-multiplexing filter is in need to separate these subcarriers individually so that they can be modulated. However, the limited tuning range and temperature sensitivity of an optical de-multiplexing filter makes the system implementation complicated and reduces the system performance. To overcome this problem, the design of a complementary phase shifter has been reported [12]. However, the reported design can only generate two subcarriers which is not sufficient to meet the ever-increasing demand. Hence, the design of a circuit that can generate more than two subcarriers will be required for near future optical system. A generalized design methodology is reported in [13-14] to generate multiple subcarriers by means of an optical Discrete Fourier Transform. However, in these approaches, it is assumed that coherently related discrete set of amplitudes are fed to the DFT network as optical inputs by means of a set of single-mode polarization fibers, which is challenging for practical implementations. To overcome this barrier, a generalized methodology is presented in [7], to perform an N^{th} order spatial DFT. It is shown that the optical DFT network can be implemented using a suitable combination of waveguides, phase shifters, splitters and combiners. This paper introduces a novel extension of the circuit architecture presented in [7], by replacing the 4×4 optical Discrete Fourier Transform (DFT) network using the combination of a properly chosen phase shifter and single 4×4 MMI coupler.

Principle of operation

Figure 1(a) shows a 4×4 DFT network using a 4×4 multimode interference (MMI) coupler and phase shifter in the appropriate position. Figure 1(b) shows the schematic of the proposed universal RF photonic circuit architecture. Note that, cascaded Y-branches are used as 1×4 splitter at the input. The input Y-branches may be replaced by using 4×4

MMI with appropriate choice of the phase shift elements as shown in Fig 1(c). Further, the waveguide crossover at the input of the 4×4 optical DFT network may be removed by interchanging the RF drive signal between phase modulator 3 (PM_3) and 4 (PM_4). The output crossover is not mandatory to implement as one know which harmonics are stronger at a particular output port. Similarly, the phase factor at the output of the DFT network can be removed in applications where the overall phase of a carrier is irrelevant. It is reported in [7] that, if the phase modulators are driven by an RF source of angular frequency ω_{RF} with a progressive phase shift of $2\pi/N$, each of the output ports generate carriers with frequency shift of $q\omega_{RF}$ where $q \sim p$ modulo N, and p is the output port number.
The transfer matrix of a 4×4 MMI can be written as [15]:

$$\mathrm{T} = \frac{1}{\sqrt{4}} \begin{bmatrix} 1 & -\xi & \xi & 1 \\ -\xi & 1 & 1 & \xi \\ \xi & 1 & 1 & -\xi \\ 1 & \xi & -\xi & 1 \end{bmatrix} \tag{1}$$

where, $\xi = \exp(-i\,\pi/4)$.

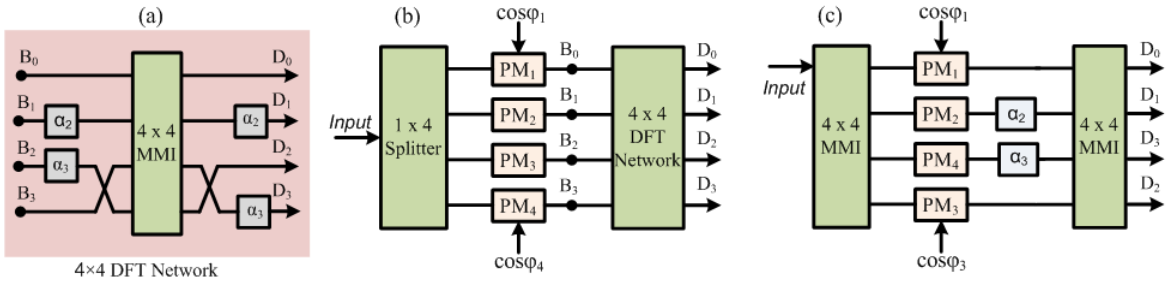

Fig. 1. (a) 4×4 optical DFT network; (b) schematic of the proposed circuit for $N = 4$; (c) realization of the proposed circuit using 4×4 MMI.

If α_2 and α_3 are set to $\exp(i\,5\pi/4)$ and $\exp(i\,\pi/4)$, the transfer matrix of the 4×4 DFT network can be written as:

$$\mathrm{T} = \frac{1}{\sqrt{4}} \begin{bmatrix} 1 & 1 & 1 & 1 \\ 1 & i & -i & -1 \\ 1 & -i & i & -1 \\ 1 & -1 & -1 & 1 \end{bmatrix} \tag{2}$$

an interchange of columns 3 and 4; and then row 3 and 4 yields:

$$\begin{bmatrix} D_0 \\ D_1 \\ D_2 \\ D_3 \end{bmatrix} = \frac{1}{\sqrt{4}} \begin{bmatrix} 1 & 1 & 1 & 1 \\ 1 & i & -1 & -i \\ 1 & -1 & 1 & -1 \\ 1 & -i & -1 & i \end{bmatrix} \begin{bmatrix} B_0 \\ B_1 \\ B_2 \\ B_3 \end{bmatrix} \tag{3}$$

which is the transfer matrix of a 4×4 DFT network. Now, if the input light waves of having equal amplitudes and phases are applied to the DFT network, results in spatially separated carriers with frequency shift of $p\omega_{RF}$ modulo N, where p is the output port number. To reduce the components, the 1×4 splitter can be replaced with 4×4 MMI with new phase factors ($\alpha_3 = \alpha_4 = \exp(i\pi/2)$).

Simulation result

The proposed concept is verified by simulation using industry standard software tool (VPIphotonics). A continuous wave DFB laser is set at 1550 nm with a power of 10 mW is used as an optical source. A 10 GHz RF drive signal having a peak amplitude of $v_{RF} = 0.25v_{\pi}$ is applied to the phase modulators with proper phase as mentioned earlier. Figure 2(a) shows the simulated optical spectrum which verify the theoretical prediction. The correct function of the circuit may deviate from ideal because of power

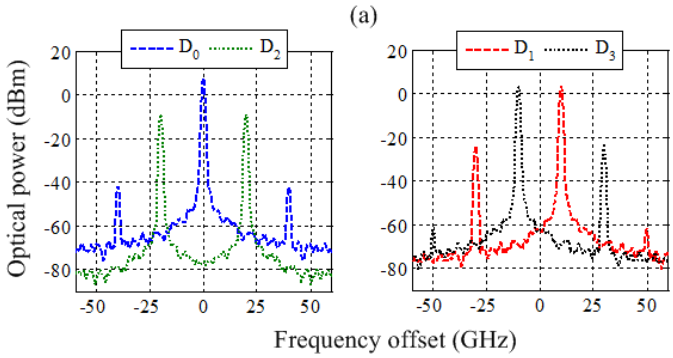

Fig. 2(a) simulated optical spectrum at the output of the circuit. RF drive signal frequency of 10 GHz is used in this simulation.

imbalances and phase error between the ports of MMI due to design errors, fabrication tolerances and error in the waveguide length that connects the RF drive signal and phase modulator. To account the design errors of MMI, all the necessary information (for example; length, width, input and output port position etc.) related to MMI design is extracted from the mask of the design presented in [16]. Then the Photon Design software tool FimmWave is used to reconstruct the S-matrix of the MMI by using the information collected from the mask. It can be assumed that all the components in a circuit will suffer similar errors. The reconstructed S-matrix of the MMI is used to configure all the MMI of the circuit in VPIphotonics simulation tool. Table 1 gives the parameters of the reconstructed S matrix. Figure 3(a)-(d) shows the simulated optical spectrum with the design errors. It shows that, a side harmonic suppression ratio (SHSR) of 21 dB or more is obtained. The SHSR can be improved by using sub-wavelength engineered MMIs [17] and driving the modulators as hard as possible so that all the harmonics will have almost equal amplitude.

Table 1. Summary of the phase error and power imbalances between the ports of the MMIs

	Output ports	**Power splitting ratio**	**Phase errors**
4 × 4 MMI	1	22.20%	4˚ phase error is considered between output ports 1 & 4
	2	23.43%	
	3	24.30%	2˚ phase error is considered between output ports 2 & 3
	4	21.59%	

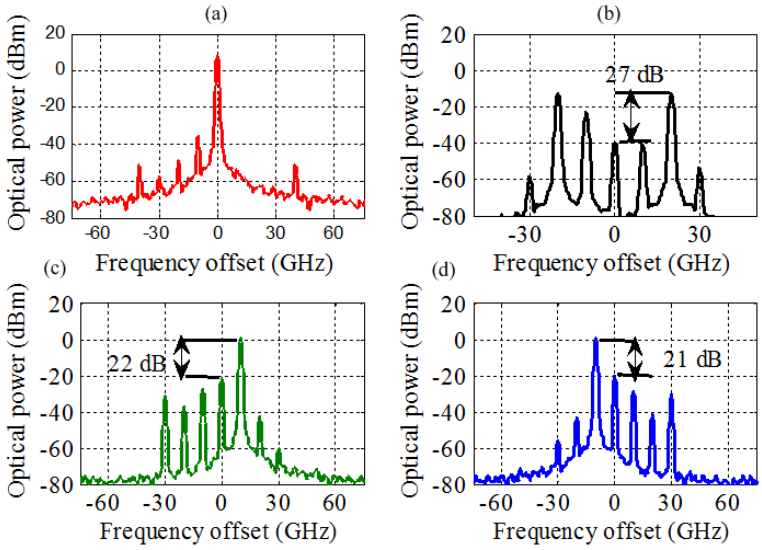

Fig. 3. (a)-(d) simulated optical spectrum considering MMI design errors.

Conclusion

In summary, a systematic design method for implementing spatial Discrete Fourier Transform in an integrated optical network has been presented. The design comprises of N parallel electro-optic phase modulators electrically driven by sinusoidal RF signal with a progressive phase shift of $2\pi/N$. The design has been verified by simulation for a $N = 4$ architecture. Non-ideal scenarios such as the presence fabrication errors has been considered and quantified. The practical implementation of the circuit depends on the availability of a suitable photonic integration platform that offers linear electro-optic phase modulators. In this context, $LiNbO_3$ offers mature integrated electro-optic modulator technology and that may be butt coupled to a planar light circuit containing the passive components [6]. Moreover, the continues advances made in the linearity, speed and footprint of electro-optic modulators based on thin film organic or ferroelectric oxides on silicon photonics augurs well for the future.

Reference

[1] M. Hasan, R. Guemri, R. Maldonado-Basilio, F. Lucarz, J.-L. de Bougrenet, and T. J. Hall, Opt. Lett., 39(24), 6950-6953, (2014).
[2] M. Hasan, R. Maldonado-Basilio, and T. J. Hall, J. Modern Optics 62(7), 581-583(2015).
[3] R. Maldonado-Basilio, M. Hasan, H, Nikkhah, S. Abdul-Majid, R. Gumeri, F. Lucarz, J. Tocnaye, and T. J. Hall, J. Mod. Opt. 62(7), 1405-1411 (2015).
[4] M. Hasan, R. Maldonado-Basilio, and T. J. Hall, Opt. Lett. 40(11), 2501-2504 (2015).
[5] M. Hasan, and T. J. Hall, Opt. Express 23 (19), 25259-25271 (2015).
[6] R. Maldonado-Basilio, M. Hasan, R. Guemri, F. Lucarz, and T. J.Hall, Opt. Comm. 354, 122-127 (2015).
[7] T. J. Hall and M. Hasan, Opt. Express 24(7), 7600-7610 (2016).
[8] Y. Ma, Q. Yang, Y. Tang, S. Chen, and W. Shieh, Opt. Express 17(11), 9421-9427 (2011).
[9] K. Takiguchi, and T. Miwa, Electronics Letters 51 (6), 505-506 (2015).
[10] K. Takiguchi, and T. Miwa, Electronics Letters 51 (6), 505-506 (2015).
[11] K. Takiguchi, M. Oguma, H. Takahashi and A. Mori, Electronics Letters 46(8), 575-576 (2010).
[12] H. Yamazaki, T. Saida, T. Goh S. Mino, M. Nagatani, H. Nosaka, K. Murata, IEEE J. Selec. Topics Quantum Electron. 19 (6), 3400208, (2013).
[13] M. E. Marhic, Optics Letters 12 (1), 63-65 (1987).
[14] A. E. Siegman, Optics Letters 26 (16), 1215-1217 (2001).
[15] H. Nikkhah, Q. Zheng, I. Hassan, S. Abdul-Majid, and T. J. Hall, Proc. of SPIE 8412, 841217 (11 pages) (2012).
[16] S. Abdul-Majid, R. Maldonado-Basilio, C. Lei, H. Awad, I. Hasan, W. N. Ye, and T. J. Hall, Opt. Quant. Electron. 47, 1965–1971(2015).
[17] R. Halir, P. J. Bock, P. Cheben, A. Ortega-Monux, C. Alonso-Ramos, J. H. Schmid, J. Lapointe, D. Xu, J. G. Wanguemert-Perez, I Molina-Fernandez, and S. Janz, Laser Photon. Rev. 9(1), 25-49 (2015).

Experimental realization of a universal RF photonic integrated circuit

Mehedi Hasan,[1,*] Gazi Mahamud Hasan,[1] and Trevor Hall,[1]
[1]Photonic Technology Laboratory, Centre for Research in Photonics, Advanced Research Complex, University of Ottawa, 25 Templeton Street, Ottawa, K1N 6N5, ON, Canada

Abstract

This paper demonstrates the operation of a universal RF photonic circuit that consists of a generalized Mach Zehnder Interferometer architecture with its $N \times 1$ combiner replaced by a $N \times N$ optical DFT network. The proposed circuit architecture can be used for SSB modulation, frequency up-conversion/down-conversion, frequency multiplication and phase correlated subcarrier generation based on the choice of output ports and dimension (N) of the circuit. A transfer matrix approach is used to develop the theoretical predictions which are verified by simulation using industry standard software tool. An integrated circuit based on silicon photonics technology readily available in the laboratory is used for experimental confirmation.

Introduction

Optical processors containing meshes of Mach Zehnder Interferometers (MZI) when suitably configured can provide arbitrary linear processing functions of utility in a variety of applications from fundamental tests of quantum technologies to signal processing in microwave photonics. To the best of the authors' knowledge, the very first integrated MZI single side band (SSB) modulator was demonstrated in 1981 [1]. The design can be characterized as an instance of a Generalized Mach-Zehnder Interferometer (GMZI) circuit architecture, where an array of N parallel linear electro-optic phase modulators interconnect the egress ports of a 1×N splitter input coupler and the ingress ports of a N×1 combiner output coupler. Since then a plethora of publications [2-11] have applied the same architecture for different RF photonic applications including, but not limited to, SSB modulation, frequency up-conversion/ frequency shifting operation, RF frequency multiplication and phase correlated multiple carrier generation to facilitate high data transmission. The variations in the static optical and electrical phase shifts are the main differences among these circuit architectures. A universal coherent electro-optic circuit architecture is reported in [12], that subsumes all these applications in one circuit. The replacement of the N×1 combiner of a GMZI circuit by an N×N optical Discrete Fourier Transform (DFT) network is the principal innovation. Although the principal application is the generation of N phase-correlated harmonically separated subcarriers for next generation optical transmission systems, the circuit performs other applications reported in the prior art [1-11] given an appropriate choice of output ports and dimension N. The generation of N phase correlated carriers from different output ports eliminates the requirement of an optical de-multiplexing filter needed to separate subcarriers generated from same port by means of optical comb techniques [13-16].

This paper reports the experimental findings obtained from a prototype that validates the operating principles of the universal RF photonic circuit architecture disclosed in [12] for the dimension $N = 4$. A silicon photonics integrated circuit consisting of a 4×4 MMI splitter connected to a 4×4 MMI combiner via an array of four parallel dual-drive Mach Zehnder Modulators (MZM) fabricated originally for a frequency up-conversion application [17] is adapted to this experiment. The details of the fabrication technology and electro-optic characterization of the phase shifters can be found in [17]. The eight on-chip electro-optic phase shifters are effectively reduced to the four required for the verification of the proposed RF photonic circuit architecture by the selection of an appropriate drive.

The paper is structured as follows. Firstly, the general form of a universal RF photonic circuit architecture is explained, and an equivalent realization is developed. Secondly, a universal architecture is specialised to dimension $N = 4$. The theoretical analysis of the proposed architecture ($N = 4$) is then developed using a transfer matrix approach. Followed by the theoretical prediction of the adapted photonic integrated circuit under specific operating conditions is developed and verified by computer simulation. Finally, the experimental measurements are reported.

Principal of operation

Figure 1(a) shows the schematic of the proposed discrete Fourier optics RF photonic circuit. The circuit consists of a $1 \times N$ uniform splitter that excites an array of N electro-optic phase modulators with outputs combined by a $N \times N$ optical DFT network. The optical DFT network is a passive coherent network formed by a combination of 180° hybrids

implemented as 2×2 MMI couplers. The phase modulators are driven by an RF source having angular frequency of ω with a progressive phase shift of $2\pi/\mathrm{N}$. The details of the mathematical derivation are reported in [12]. The analysis reveals that the proposed architecture subsumes all MZI based circuit reported in the prior art given appropriate selection of dimension N and output port(s). Figure 1(b) shows an alternative realization of the circuit architecture drawn in Fig.1(a), where all the parallel phase modulators are replaced by an equivalent delay. The complex optical field over different paths is sampled by a progressive delay of $\mathrm{T/N}$, where T is the nominal period of the RF carrier. This is equivalent to sampling the input optical envelope at different times [18]. The merit of this architecture is that it does not require a progressive RF phase shift to drive N phase modulators. However, the fixed sampling interval limits the operating RF bandwidth. Figure 2(a-b) shows the simulated transmission spectra of the circuit for the dimension $\mathrm{N} = 2$ and $\mathrm{N} = 4$ respectively. A sampling interval of $\mathrm{T} = 0.1$ ns is considered in the simulation. Result shows that the adjacent channel cross talk is low only at the channel passband centres.

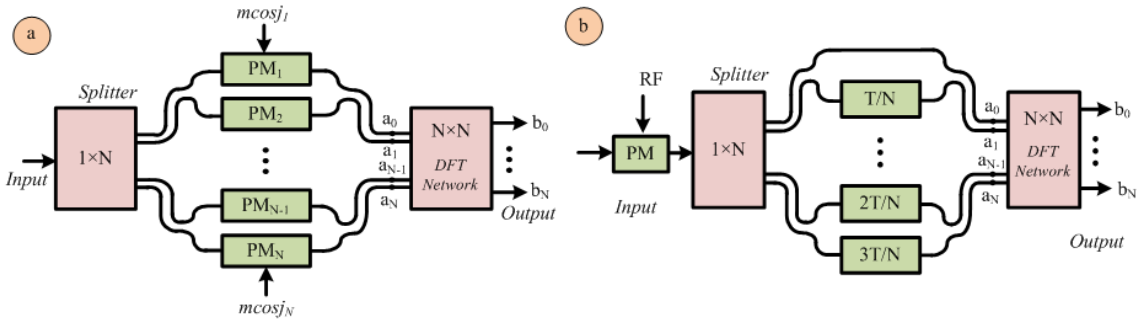

Fig. 1. (a) Architectural diagram of the proposed universal RF photonic architecture, where an array of N parallel phase modulators are sandwich between $1 \times \mathrm{N}$ splitter and $\mathrm{N} \times \mathrm{N}$ DFT network; (b) An alternative realization of the schematic shown in Fig. (a). PM, phase modulator; DFT, discrete Fourier Transform.

On the one hand, the array of parallel delay line can be mapped into a cascaded delay with a reduced number of arms, thereby reducing circuit complexity [19]. The cascaded architecture can be used as an RF frontend signal processor.[20]. On the other hand, the circuit presented in Fig. 1(a) can be operated over a range of frequencies up to the bandwidth of the phase modulator with the aid of an RF drive progressive phase shift circuit that, for example, constructs appropriate linear superpositions of in-phase and quadrature-phase components of the RF source. It is shown in reference [12], that a permutation of the phase modulators can lead to a differentially driven MZM implementation, which renders implicit the relation between the progressive phase shift and the phase modulators. In addition, the complexity of DFT network can be reduced by using higher dimension MMI couplers. For example, a 4×4 DFT network can be realized by a single 4×4 MMI couplers with properly chosen phase shifter elements [21] as illustrated in Fig. 3(a). The main difference from the circuit presented in Fig. 1(a) is that the $1 \times N$ uniform splitter is replaced by a 4×4 MMI splitter, and the (4×4) DFT network is replaced by a 4×4 MMI coupler augmented by with properly chosen phase shift elements (φ_1 and φ_2 in this case).

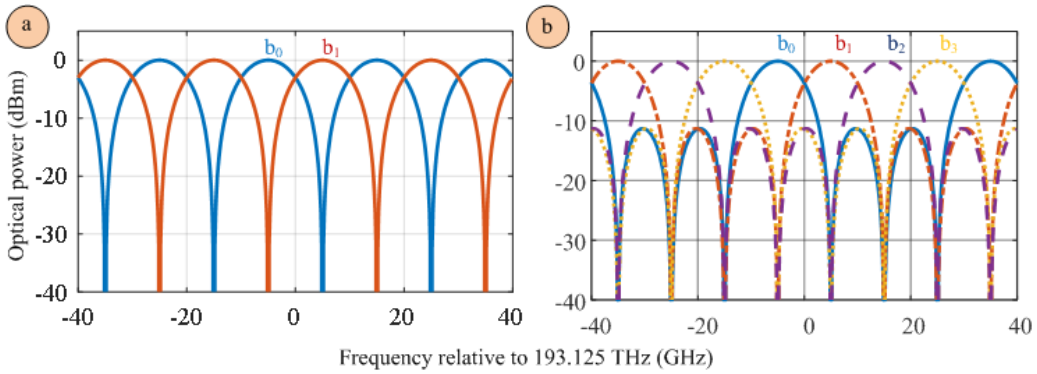

Fig. 2(a). Simulated transmission spectra of the circuit as shown in Fig.1(b) for $\mathrm{N} = 2$; (b) transmission spectra of the same circuit when the dimension $\mathrm{N} = 4$. The sample interval T is considered as 0.1 ns (10 GHz free-spectral range) in the simulation.

A photonic integrated circuit, readily available in our laboratory, is adapted to verify the operation of RF photonic circuit with a 4 × 4 DFT network as shown in Fig. 3(a). Figure 3(b) shows the schematic of the integrated circuit which consists of eight (8) parallel phase shifters with 4 × 4 MMI couplers as the input splitter and output combiner. The function of Fig. 3(a) can be emulated by the circuit in Fig. 3(b) using carefully selecting the phase shifter RF drive and bias. The remainder of this section develops an expression for the output of the circuit of Fig, 3(a) using the transfer matrix method. It is also shown theoretically, how the circuit of Fig. 3(b) may emulate the circuit of Fig. 3(a) as verified by simulation using an industry standard software tool.

Transmission matrix of the circuit architecture shown in Fig. 3(a) is:

$$\begin{bmatrix} O_1 \\ O_2 \\ O_3 \\ O_4 \end{bmatrix} = T_{4\times4} \begin{bmatrix} \exp(j\varphi_1) & 0 & 0 & 0 \\ 0 & \exp(j\varphi_2) & 0 & 0 \\ 0 & 0 & -\exp(j\varphi_4) & 0 \\ 0 & 0 & 0 & -\exp(j\varphi_3) \end{bmatrix} T_{4\times4} \begin{bmatrix} I_1 \\ I_2 \\ I_3 \\ I_4 \end{bmatrix} \tag{1}$$

where:

$$T_{4\times4} = \frac{1}{\sqrt{4}} \begin{bmatrix} 1 & \zeta & -\zeta & 1 \\ \zeta & 1 & 1 & -\zeta \\ -\zeta & 1 & 1 & \zeta \\ 1 & -\zeta & \zeta & 1 \end{bmatrix} \quad ; \quad \zeta = e^{-i\pi/4} \tag{2}$$

is the transfer matrix of a 4×4 MMI coupler;

$$\varphi_j = \pi\, v_j / v_\pi \tag{3}$$

is the induced optical phase shift caused by RF signal having amplitude of v_j; and v_π is the half-wave voltage of the modulator.

If the input I_1 is energized only,

$$\begin{bmatrix} O_1 \\ O_2 \\ O_3 \\ O_4 \end{bmatrix} = (1/4) I_1 \begin{bmatrix} \exp(jv_1) - j\exp(jv_2) + j\exp(jv_4) - \exp(jv_3) \\ \zeta\{\exp(jv_1) + \exp(jv_2) + \exp(jv_4) + \exp(jv_3)\} \\ \zeta\{-\exp(jv_1) + \exp(jv_2) + \exp(jv_4) - \exp(jv_3)\} \\ \exp(jv_1) + j\exp(jv_2) - j\exp(jv_4) - \exp(jv_3) \end{bmatrix} \tag{4}$$

In the case of an RF drive of the form:

$$v_1 = m\cos(\omega t)\,;\; v_2 = m\cos(\omega t + \pi/2)\,;\; v_3 = m\cos(\omega t + \pi)\,; v_4 = m\cos(\omega t + 3\pi/2) \tag{5}$$

where m is the depth of modulation; defined as;

$$m = \pi v_{RF} / v_\pi \tag{6}$$

After applying the Jacobi Anger expansion and simplifying [22]:

$$\begin{bmatrix} O_1 \\ O_2 \\ O_3 \\ O_4 \end{bmatrix} = I_1 \begin{bmatrix} i\{J_1(m)\exp[j\omega_{RF}t] - J_3(m)\exp[-j3\omega_{RF}t] \ldots\} \\ e^{-i\pi/4}\{J_0(m) + 2J_4(m)\cos(4\omega_{RF}t) \ldots\} \\ e^{-i\pi/4}\{2J_2(m)\cos(2\omega_{RF}t) + 2J_6(m)\cos(6\omega_{RF}t) \ldots\} \\ i\{J_1(m)\exp[-j\omega_{RF}t] - J_3(m)\exp[j3\omega_{RF}t] \ldots\} \end{bmatrix} \tag{7}$$

It can be observed that the proposed circuit subsumes RF photonic architecture defined in the prior art for single side band suppressed carrier modulation (SSB-SC), I-Q modulation, frequency multiplication and spatially separated carrier generation given an appropriate output port choices and dimension of the phase modulator used. For example, for output port-1 (O_1) all the harmonics are suppressed except -3ω_{RF}, +1ω_{RF}; which provides a $+\omega_{RF}$ shift of the optical carrier frequency or equivalently upper SSB modulation. Similarly, output port-4 (O_4) provides a $-\omega_{RF}$ shift of the optical carrier frequency or lower SSB modulation. For output port-2 (O_2) all the harmonics are suppressed except the carrier and $\pm 4^{th}$ harmonics. For output port-2 (O_2) all the harmonics are suppressed except $\pm 2\omega_{RF}$ and $\pm 6\omega_{RF}$. If impinged onto a photodiode, a frequency multiplication of four times ($4\omega_{RF}$) can be obtained. Each of the

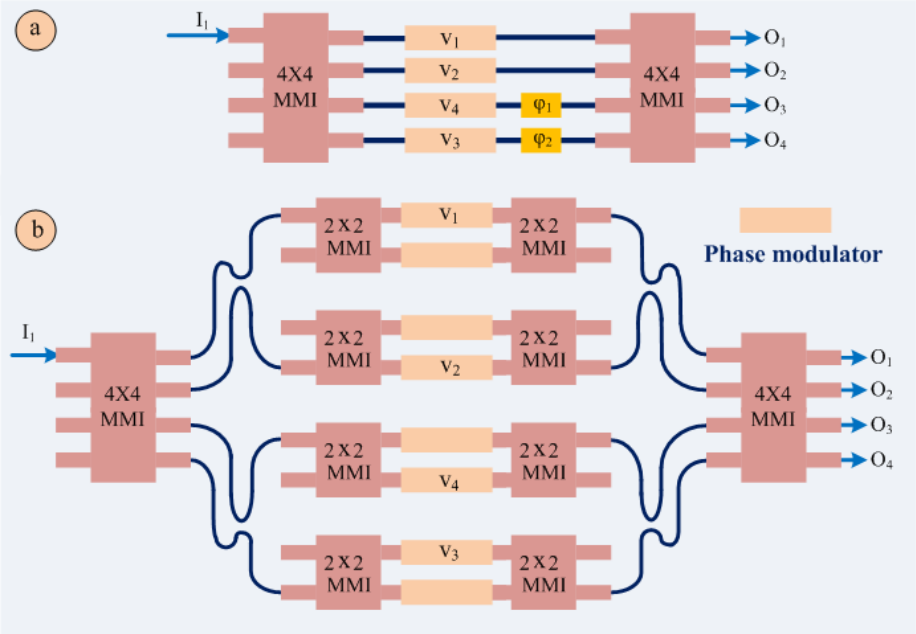

Fig. 3(a) Four parallel phase modulators between 4 × 4 optical DFT network and 1 × 4 Splitter, thereby create discrete Fourier optics RF photonic circuit [12]; (b) adapted readily available fabricated chip to demonstrate the function of Fig. (a).

output of the complete architecture may be used to spatially separate a subcarrier to facilitate high data rate transmission. Table 1 summaries the circuit functions when four phase-modulators are used.

Table 1. Functions provided by circuit architecture presented in Fig. 3(a)

Function	Port(s) used	Remarks
IQ modulation, SSB-SC & electro-optic frequency conversion	1(O_1) or 4 (O_4)	
× 4 RF frequency multiplication	3 (O_3)	× 8 RF can be generated from port-2 by suppressing the carrier
Spatially separated carrier generation	all	

For identical optical path lengths, when the upper arm is driven only, the transfer matrix of a 2 × 2 MZM can be written as:

$$\begin{bmatrix} O_1 \\ O_2 \end{bmatrix} = \frac{1}{2}\begin{bmatrix} 1 & -i \\ -i & 1 \end{bmatrix}\begin{bmatrix} \exp(j\varphi) & 0 \\ 0 & 1 \end{bmatrix}\begin{bmatrix} 1 & -i \\ -i & 1 \end{bmatrix}\begin{bmatrix} I_1 \\ I_2 \end{bmatrix} \tag{8}$$

where $\frac{1}{\sqrt{2}}\begin{bmatrix} 1 & -i \\ -i & 1 \end{bmatrix}$ is the transfer matrix of a 2 × 2 MMI. Simplifying Eq. (8)

$$\begin{bmatrix} O_1 \\ O_2 \end{bmatrix} = \frac{1}{2}\begin{bmatrix} \exp(j\varphi) - 1 & -i\{\exp(j\varphi) + 1\} \\ -i\{\exp(j\varphi) + 1\} & 1 - \exp(j\varphi) \end{bmatrix}\begin{bmatrix} I_1 \\ I_2 \end{bmatrix} \tag{9}$$

Similar way, when the lower arm is driven only. The transfer matrix can be written as,

$$\begin{bmatrix} O_1 \\ O_2 \end{bmatrix} = \frac{1}{2}\begin{bmatrix} 1-\exp(j\varphi) & -i\{\exp(j\varphi)+1\} \\ -i\{\exp(j\varphi)+1\} & \exp(j\varphi)-1 \end{bmatrix}\begin{bmatrix} I_1 \\ I_2 \end{bmatrix} \tag{10}$$

In the fabricated chip, only the minimum transmission port of the MZMs are connected to the outer 4×4 MMI. Hence, one can use either $\exp(j\varphi_1) - 1$ or $1 - \exp(j\varphi_1)$ as the transmission of each MZM based on the input port selection. The transmission matrix of the adapted circuit as shown in Fig. 3(b**)**, when only one arm of each MZI is excited is given by:

$$\begin{bmatrix} O_1 \\ O_2 \\ O_3 \\ O_4 \end{bmatrix} = (1/2)T_{4\times4}\begin{bmatrix} \exp(j\varphi_1)-1 & 0 & 0 & 0 \\ 0 & \exp(j\varphi_2)-1 & 0 & 0 \\ 0 & 0 & 1-\exp(j\varphi_4) & 0 \\ 0 & 0 & 0 & 1-\exp(j\varphi_3) \end{bmatrix} T_{4\times4}\begin{bmatrix} I_1 \\ I_2 \\ I_3 \\ I_4 \end{bmatrix} \tag{11}$$

where φ_j is the optical phase shift induced by RF drive signal as defined by Eq. (3).

When the light is launched into input I_1 only, simplifying Eq. (11) using Eq. (3),

$$\begin{bmatrix} O_1 \\ O_2 \\ O_3 \\ O_4 \end{bmatrix} = (1/8)\, I_1\begin{bmatrix} \exp(jv_1) - j\exp(jv_2) + j\exp(jv_4) - \exp(jv_3) \\ \zeta\{-4 + \exp(jv_1) + \exp(jv_2) + \exp(jv_4) + \exp(jv_3)\} \\ \zeta\{-\exp(jv_1) + \exp(jv_2) + \exp(jv_4) - \exp(jv_3)\} \\ \exp(jv_1) + j\exp(jv_2) - j\exp(jv_4) - \exp(jv_3) \end{bmatrix} \tag{12}$$

The applied RF drive is as given by Eq. (5). Applying Jacobi Anger expansion and simplifying,

$$\begin{bmatrix} O_1 \\ O_2 \\ O_3 \\ O_4 \end{bmatrix} = (1/2)I_1\begin{bmatrix} i\{J_1(m)\exp[j\omega_{RF}t] - J_3(m)\exp[-j3\omega_{RF}t] \dots\} \\ e^{-i\pi/4}\{J_0(m) - 1 + 2J_4(m)\cos(4\omega_{RF}t) \dots\} \\ e^{-i\pi/4}\{2J_2(m)\cos(2\omega_{RF}t) + 2J_6(m)\cos(6\omega_{RF}t) \dots\} \\ i\{J_1(m)\exp[-j\omega_{RF}t] - J_3(m)\exp[j3\omega_{RF}t] \dots\} \end{bmatrix} \tag{13}$$

If I_2 is excited,

$$\begin{bmatrix} O_1 \\ O_2 \\ O_3 \\ O_4 \end{bmatrix} = \frac{1}{2}I_2\begin{bmatrix} e^{-i\pi/4}\{J_0(m) - 1 + 2J_4(m)\cos(4\omega_{RF}t) \dots\} \\ i\{J_1(m)\exp[-j\omega_{RF}t] - J_3(m)\exp[j3\omega_{RF}t] \dots\} \\ i\{J_1(m)\exp[j\omega_{RF}t] - J_3(m)\exp[-j3\omega_{RF}t] \dots\} \\ e^{-i\pi/4}\{2J_2(m)\cos(2\omega_{RF}t) + 2J_6(m)\cos(6\omega_{RF}t) \dots\} \end{bmatrix}[I_2] \tag{14}$$

Eq. (13) is identical to Eq. (7) albeit the power at the output of the adopted chip is reduced by -6dB. In addition to, the output at port-2 (O_2) contain an extra carrier term contributed by the unmodulated arm of the MZM. Although, the constant carrier term is a part of the output of all the MZMs, it cancels out automatically from all the output ports due to inherent input/output phase relationship of the adapted circuit except from port O_2.

To verify this theoretical prediction, a simulation is performed using the industry standard software tool, VPIphotonics. A CW-DFB laser having output power of 20 mW with an operating vacuum wavelength of 1550 nm is used as an optical source. A 10 GHz RF signal having peak amplitude of $0.25v_\pi$ and appropriate phase shift as per Eq. (4) is applied to the phase modulators. Figure 4. (i-iv) shows the optical spectrum at the output ports of the 4×4 MMI. The output spectrum justifies the theoretical prediction as derived in Eq. (13). In practice, the power imbalances and phase errors between the ports of an MMI caused by variation in the fabrication processes deviate the correct operation of the circuit from ideal behaviour. The S-matrix of the MMI is perturbed from ideal to account the fabrication tolerances. In this simulation, the S-matrix of all the 2×2 MMI along with the two 4×4 MMI are configured according to the parameters listed in the Table 2 and loaded in VPIphotonics. The details about MMI tolerances can be found in [23]. The MMI design can be improved further using sub-wavelength engineering and broadband operation can be assured [24]. Simulated optical spectra shows that strong carrier breakthrough occurs at the output of the circuit. To improve the performance an integrated variable optical attenuator (VOA) [25] can be used to improve extinction or, to be more systematic, a trimming algorithm applied [26].

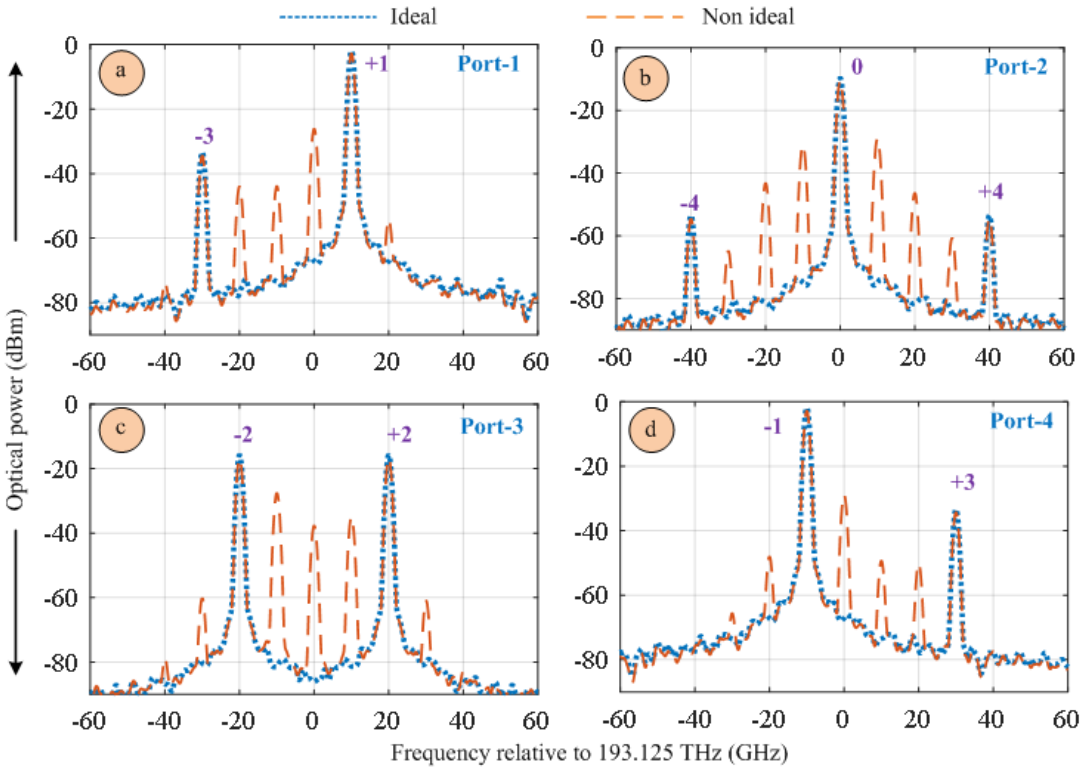

Fig. 4. Simulation result of the schematic presented in Fig. 3(b); (a-d) Optical spectrum at the four output ports (port-1, port-2, port-3 and port-4 respectively) of the 4 × 4 MMI when light is launched from the input port-1; The ideal plots are obtained when there no phase error and power imbalances among the ports of MMIs, whereas the non-ideal plots are obtained by adding power imbalances and phase errors in the MMIs according to the reference [23].

Table 2. Summary of the power imbalances and phase error of the MMIs [23].

Type of MMI	Output ports	Power splitting ratio	Phase errors
4×4	1	25%	2° phase error is considered between output ports 1 & 4
	4	23%	
	2	24%	2° phase error is considered between output ports 2 & 3
	3	22%	
2×2	1	50%	1° phase error
	2	49%	

Results and discussion

A photonic integrated circuit readily available in the laboratory, fabricated for another application is adapted for the experimental demonstration of a discrete Fourier transform based RF photonic integrated circuit. Figure 5 shows the photograph of the fabricated chip with wire bonding. The device was fabricated using CMOS compatible SOI technology. The thickness of the buried oxide layer was 2 μm, whereas the thickness of the top Si layer was 220 nm. The wide width of the p-n junction-based phase shifter in comparison to the width of the input/output ports of the MMI introduces waveguide bends into the circuit layout. As such, path length matching becomes a most important and critical aspect of the design. More detail about the fabricated chip can be found in [17, 23]. The detail design of the MMI presented in the fabricated chip can be found in [27].

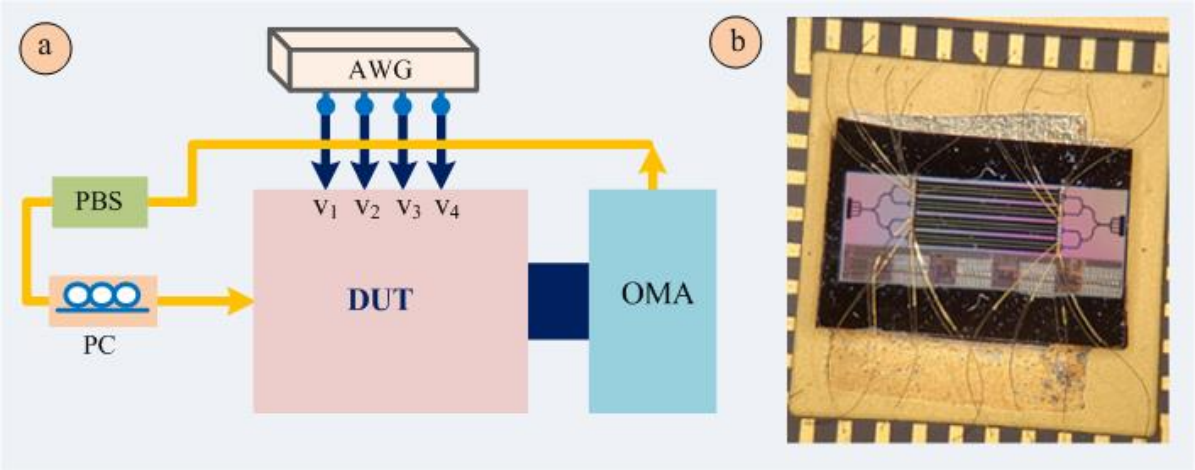

Fig. 5. (a) Schematic of the measurement setup; (b) microscopic image of the wire bonded chip; AWG, arbitrary waveform generator; PBS, polarization beam splitter; PC, polarization controller; OMA, optical modulation analyzer; DUT, device under test.

A continuous wave laser at a wavelength of 1550.38 nm is used as the optical input. A polarization beam-splitter (PBS) followed by a polarization controller (PC) is used to constrain the polarization of the light input to the silicon chip to be TE-like. The output of the circuit is connected to an optical modulation analyzer (Agilent N4391A) which is connected to a digital storage oscilloscope (Infiniium DSO-20-91604A). To maintain the same polarization state, polarization maintaining fiber is used for all connections. Lensed fibers are used for fiber-to-chip coupling at the input-output to reduce coupling loss. The four phase modulators are driven by four RF signals with specific phase relationship generated by a four-channel arbitrary waveform generator (AWG) (Fluke 294). The four RF signals with

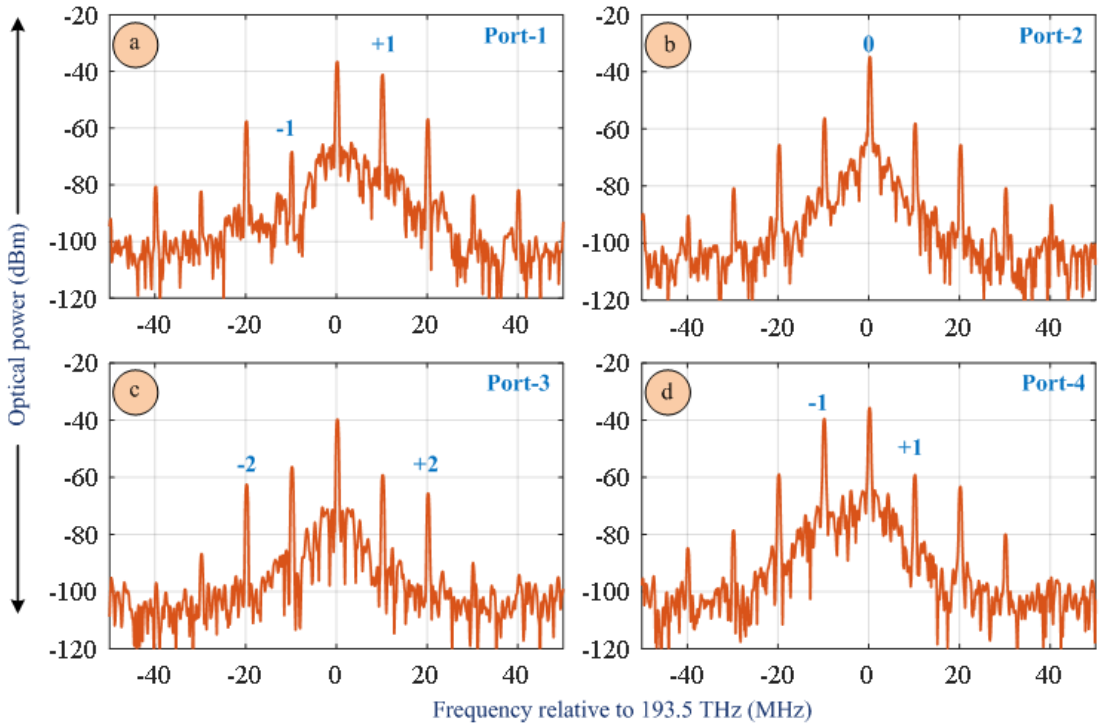

Fig. 6. Measured optical spectra at different output ports of the 4 × 4 MMI when the light is launched from input port 1 (I_1); (a) port-1 (O_1); (b) port-2 (O_2); (c) port-3 (O_3); (d) port-4 (O_4).

progressive phase shifts are denoted as V_1, V_2, V_3 and V_4 in Fig 5. A 10 MHz sinusoid signal with amplitude 2.5V is applied to each phase shifter. For this circuit to be operated as a DFT network, careful positioning of the RF drives from the AWG is necessary. For example, to maintain symmetry with the ideal DFT circuit shown in Fig. 3(a), RF drives V_4 and V_3 are applied to the phase modulators at the lower and upper arm of the MZM_3 and MZM_4 respectively so that the π optical phase shifts can be naturally derived from the phase relationship of the input-output ports of the corresponding 2×2 MMIs. A DC voltage of -3 V is applied via bias tee to make sure the p-n junction always operates in reverse bias. The DC biases are tuned slightly to obtain the correct operation. Light from the optical source is applied to individual input of the chip to investigate the response separately. The measured optical spectra of the four output ports of the circuit when the optical source is connected to input 1 of the circuit is shown in Fig. 6. Output port-1 and port-4 generates upper sideband and lower sideband respectively aligned with the theoretical prediction. The theoretically pristine performance of the circuit is limited by the presence of carrier and undesired spurious sidebands. The carrier breakthrough is too high due to power and phase imbalances between the ports of the MZM and the inactive phase shifter arm in each of the MZM working as bypass light path. Furthermore, the modulators are driven at a peak voltage of 2.5V due to limitation of the source, resulting in very small modulation index so that a suppressed carrier amplitude remains strong in comparison to the weak sidebands. The output spectrum at port-2 well justifies the theoretical prediction. Output port-3 should result in the dominance of the +2 and -2 harmonics. The +1 and -1 harmonics are suppressed to -60 dBm from circa -40 dBm. Due to the small modulation index, the amplitude of the 2^{nd} harmonic is too low. High insertion loss is also observed. The principal reason is that the chip lacks any mechanism for matching between the fiber mode and high-contrast access waveguide mode and some defects have also been observed on the chip [17].

To verify the correct operation of the circuit, further investigation is performed by changing the input light injection from input port-1 to port-2. The output spectrum is shown in Fig. 7. Now the optical carrier and $\pm 2^{nd}$ harmonic excite from the port-1(O_1) and port-4 (O_4) respectively. Similarly, output port-2 and port-3 generates LSB and USB respectively. The same kind of deviations from the theoretical prediction are observed as shown in Fig. 7. Nevertheless, it can be concluded that the circuit functions as universal RF photonic circuit described in [12] which subsumes the majority of the prior art in RF photonics. The main aim of this report is to prove that the fabrication of $N = 4$ parallel phase modulators combined by an (4×4) DFT circuit can be made practical. Careful design with

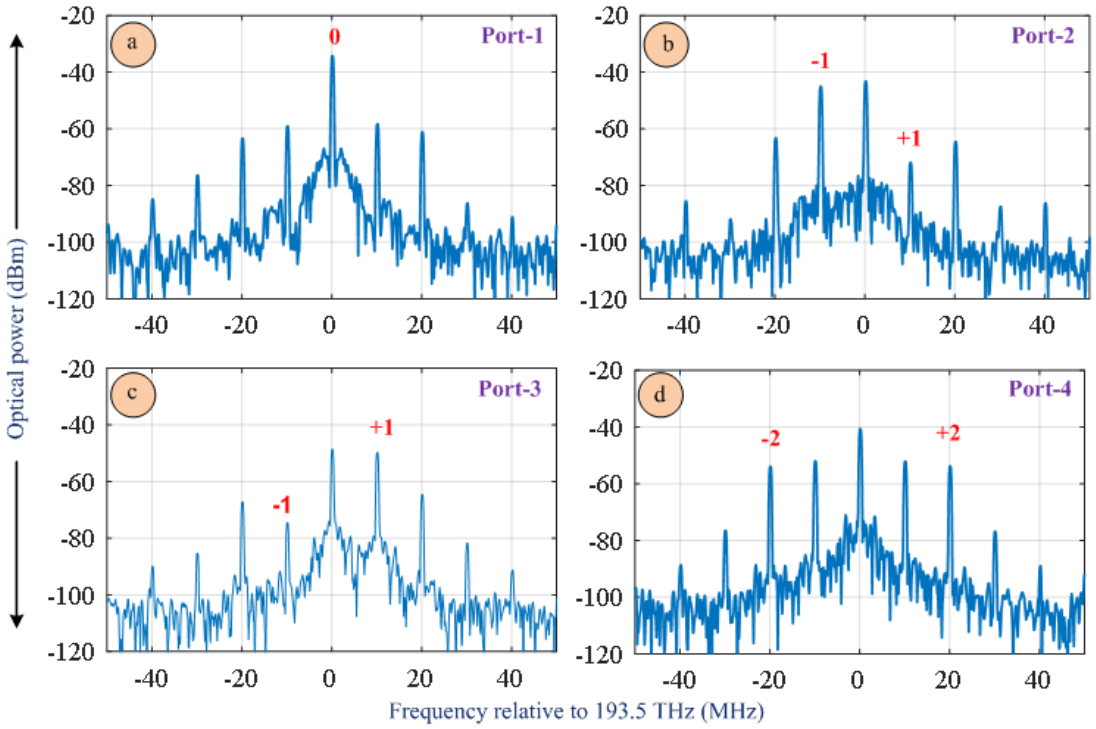

Fig. 7. Measured optical spectra at different output ports of the 4 × 4 MMI when the light is launched from input port 2 (I_2); (a) port-1 (O_1); (b) port-2 (O_2); (c) port-3 (O_3); (d) port-4 (O_4).

incorporating tuning mechanism via means of a phase shifter, VOA [25] or more in a systematic way, i.e. by using algorithm [26], can be applied to improve further the performance of the circuit.

Conclusion

In summary, a previously proposed RF photonic circuit architecture consists of $1 \times N$ splitter connected with $N \times N$ DFT network via N parallel electro-optic phase modulator has been implemented. A photonic integrated circuit based on silicon photonics technology having eight parallel phase shifters connected between 4×4 MMI at the input and output is configured for the target application. All though phase-correlated but spatially separated subcarrier generation is the principal aim, the circuit can subsume majority of the RF photonic applications in the prior art. Experimental results verify the theoretical prediction but the unwanted harmonics suppression ratio and specifically the carrier suppression is not sufficient for two reasons. Firstly, due to the unavailability of high-power RF signal source having four output channels, the phase shifters are driven at low modulation index. Consequently, the $\pm 1^{st}$ harmonics are weak compared to the carrier so that magnitude of the carrier breakthrough due to fabrication tolerances and bias errors remains significant relative to the magnitude of the sidebands. There is no tuning element in the circuit to compensate the MMI output power imbalances and phase errors due to the fabrication and bias errors. Nevertheless, it has been demonstrated that the universal RF photonic architecture described in [12] can be materialized using current state of the art technology, thereby, establishing a systematic design approach for future RF photonic applications.

Reference:

1. M. Izutsu, S. Shikama, T. Sueta, "Integrated optical SSB modulator / frequency shifter," IEEE J. Quantm Electron. 17, 2225-2227 (1981).
2. G. H. Smith, D. Novak, and Z. Ahmed, "Overcoming chromatic-dispersion effects in fiber-wireless systems incorporating external modulators," IEEE Trans. Microwave Theory Tech. 45, 1410-1415 (1997).
3. S. Shimotsu, S. Oikawa, T. Saitou, N. Mitsugi, K. Kubodera, T. Kawanishi and M. Izutsu, "Single side-band modulation performance of a LiNbO3 integrated modulator consisting of four-phase modulator waveguides," IEEE Photon. Technol. Lett. 13, 364-366 (2001).
4. J. Yu, Z. Jia, L. Yi, Y. Su, G.-K. Chang, and T. Wang, "Optical millimeter-wave generation or up-conversion using external modulators," IEEE Photon. Technol. Lett., 18(1), 265 (2006).
5. A. Wen, M. Li, L. Shang, and Y. Chen, "A novel optical SSB modulation scheme with interfering harmonics suppressed for ROF transmission link," Opt. Laser Technol. 43, 1061-1064 (2011).
6. C. W. Chow, C. H. Wang, C. H. Yeh, and S. Chi, "Analysis of the carrier-suppressed single-sideband modulators used to mitigate Rayleigh backscattering in carrier-distributed PON," Opt. Express 19, 10973-10978 (2011).
7. M. Hasan, R. Maldonado-Basilio, T. J. Hall, "Comments on X. Yin, A. Wen, Y. Chen, and T. Wang, "Studies in an optical millimeter-wave generation scheme via two parallel dual-parallel Mach-Zehnder modulators," J. Mod. Opt. 62, 581-583 (2015).
8. P.-T. Shih, J. Chen, C.-T. Lin, W.-J. Jiang, H.-S. Huang, P.-C. Peng, and S. Chi, "Optical millimeter-wave signal generation via frequency 12-tupling," J. Lightwave Technol. 28, 71-78 (2010).
9. M. Hasan, R. Maldonado-Basilio, and T. J. Hall, "Dual-function photonic integrated circuit for frequency octo-tupling or single-side-band modulation," Opt. Lett. 40, 2501-2504 (2015).
10. R. Maldonado-Basilio, M. Hasan, H, Nikkah, S. Abdul-Majid, R. Gumeri, F. Lucarz, J. Tocnaye, and T. J. Hall, "Electro optic up-conversion mixer amenable to photonic integration," Journal of Modern Optics 62,1405-1411 (2015).
11. H. Yamazaki, T. Saida, T. Goh S. Mino, M. Nagatani, H. Nosaka, K. Murata, "Dual-carrier dual-polarization IQ modulator using a complementary frequency shifter," IEEE J. Sel. Top. Quantum Electron. 19, 3400208 (2013).
12. Trevor J. Hall and Mehedi Hasan, "Universal discrete Fourier optics RF photonic integrated circuit architecture," Opt. Express 24 (7), 7600-7610 (2016).
13. Y. Ma, Q. Yang, Y. Tang, S. Chen, and W. Shieh, "1-Tb/s single-channel coherent optical OFDM transmission over 600-km SSMF fiber with subwavelength bandwidth access," Opt. Express 17, 9421-9427 (2009).
14. K. Takiguchi, T. Kitoh, A. Mori, M. Oguma, and H. Takahashi, "Integrated-optic OFDM demultiplexer using slab star coupler based optical DFT circuit," 36th European Conference and Exhibition on Optical Communication (ECOC), Torino, 2010, pp. 1-3.
15. W. Li, X. Liang, W. Ma, T. Zhou, B. Huang, and D. Liu, "A planar waveguide optical discrete Fourier transformer design for 160 Gb/s all-optical OFDM systems," Opt. Fiber Technol. 16, 5-11 (2010).
16. K. Takiguchi, and T. Miwa, "Integrated-optic OFDM signal multiplexer composed of optical IFFT circuit," Electron. Lett. 51, 505-506 (2015).
17. G. M. Hasan, M. Hasan, and T. Hall, "Performance analysis of a multi - function photonic architecture on SOI acting as a frequency shifter," TechRxiv. Preprint (2020). https://doi.org/10.36227/techrxiv.12237032.v1
18. Arthur James Lowery, "Design of arrayed-waveguide grating routers for use as optical OFDM demultiplexers," Opt. Express 18 (13), 14129-14143 (2010).
19. D. Hillerkuss, M. Winter, M. Teschke, A. Marculescu, J. Li, G. Sigurdsson, K. Worms, S. Ben Ezra, N. Narkiss, W. Freude, and J. Leuthold, "Simple all-optical FFT scheme enabling Tbit/s real-time signal processing," Opt. Express 18 (9), 9324-9340 (2010).
20. H. Yu, M. Chen, Q. Guo, M. Hoekman, H. Chen, A. Leinse, R. G. Heideman, R. Mateman, S. Yang, and S. Xie, "Si3N4-based integrated optical analog signal processor and its application in RF photonic frontend," IEEE Photon. J. 7, 1–9 (2015).
21. M. Hasan, De Gui Sun, Peng Liu and T. J. Hall, "Towards a universal RF photonic integrated circuit architecture for microwave applications," 2016 Progress in Electromagnetic Research Symposium (PIERS), Shanghai, 2016, pp. 84-87.
22. Mehedi Hasan, Rabiaa Guemri, Ramón Maldonado-Basilio, Frédéric Lucarz, Jean-Louis de Bougrenet de la Tocnaye, and Trevor Hall, "Theoretical analysis and modeling of a photonic integrated circuit for frequency 8-tupled and 24-tupled millimeter wave signal generation," Opt. Lett. 39, 6950-6953 (2014).

23. Mehedi Hasan, Jianqi Hu, Hamdam Nikkhah and Trevor Hall, "A photonic circuit for complementary frequency shifting, in-phase quadrature/single sideband modulation and frequency multiplication: analysis and integration feasibility," Journal of Modern Optics, 64:14, 1386-1397(2017).
24. R. Halir, P. Bock, P. Cheben, A. Ortega-Moñux, C. Alonso-Ramos, J. Schmid, J. Lapointe, D. Xu, J. Wangüemert-Pérez, I. Molina-Fernández, and S. Janz, "Waveguide sub-wavelength structures: a review of principles and applications," Laser Photonics Rev., 9(1), 25-49 (2015).
25. H. Yamazaki, T. Saida, T. Goh S. Mino, M. Nagatani, H. Nosaka, K. Murata, "Dual-carrier dual-polarization IQ modulator using a complementary frequency shifter," IEEE J. Selec. Topics Quantum Electron. 19 (6), 3400208, (2013).
26. C. M. Wilkes, X. Qiang, J. Wang, R. Santagati, S. Paesani, X. Zhou, D. A. B. Miller, G. D. Marshall, M. G. Thompson, and J. L. O'Brien, "60 dB high-extinction auto-configured Mach–Zehnder interferometer," Opt. Lett. 41, 5318-5321 (2016).
27. S. Abdul-Majid, R. Maldonado-Basilio, C. Lei, H. Awad, I. Hasan, W.N. Ye, and T. Hall, "Performance analysis of a photonic integrated interferometer circuit based on silicon-on-insulator;" Opt. Quant. Electron. 47, 1965–1971 (2015).

CHAPTER 3

High resolution optical spectrometer

3.1 Summary

In this chapter, the design of a technologically viable compact on-chip high-resolution wideband spectrometer is presented and verified by software simulation using an industry standard tool. The target application is to measure the spectral profile of WDM signals accurately in flex- and fixed-grid architectures across the entire C-band 1530-1565 nm aiming at sub-GHz resolution bandwidth with minimum scan time and better than 1 GHz frequency resolution. The proposed architecture consists of three stages. The first stage is a tunable ring resonator (RR) that defines the resolution. The third stage is an arrayed waveguide grating (AWG) that isolates one RR resonance within each of its channels. The second stage uses an MZI to form a coherent superposition of two interleaved AWG channel spectra corresponding to a pair of input ports; establishing gang tuning of the RR and AWG to retain the RR resonance at the center of the AWG channel passband. A refinement of the architecture is also presented by replacing the coherent superposition of a pair of AWG input channels to the incoherent superposition of pairs of AWG outputs. This eliminates the MZI stages, consequently the spectrometer does not require any control of the inter-stage optical path length, which renders the spectrometer more robust to fabrication process variations.

3.2 Contribution

The research findings reported in this chapter have been published as an article in *IEEE Photonics Journal* and a manuscript submitted to *Optics Express* for peer review. A *US PATENT* application has also been filed. I contributed to the circuit design, performed circuit level numerical modelling, simulation and wrote the manuscripts. Dr. Hall contributed to the architecture design, interpretation of the result and revised the manuscript. Mr. Peng Liu performed the RR simulation using OptiBPM. Mr. Gazi Hasan executed the simulation of the directional coupler. Dr. Mohammad Rad reviewed the manuscripts.

3.3 Article

This section is a reproduction of articles published (IEEE Photonics Journal) and submitted (Optics Express) for publication.

M. Hasan, M. Rad, G.M. Hasan, P. Liu, P. Dumais, E. Bernier and T. J. Hall, "Ultra-high resolution wideband On-chip spectrometer," *IEEE Photonics J.* 12, 1-17 (2020).

The submitted manuscript follows verbatim.

M. Hasan, M. Rad, P. Liu, E. Bernier and T. J. Hall, "Circuit design and integration feasibility of a high-resolution broadband on-chip spectral monitor," submitted to *Optics Express* (2020).

Ultra-high resolution wideband on-chip spectrometer

M. Hasan[1], M. Rad[2], G. M. Hasan[1], P. Liu[1], P. Dumais[2], E. Bernier[2], T. J. Hall[1]

[1]Photonic Technology Laboratory, Centre for Research in Photonics, Advanced Research Complex, University of Ottawa, 25 Templeton Street, Ottawa, K1N 6N5, ON, Canada
[2]Huawei Technologies Canada, 303 Terry Fox Drive, Kanata, K2K 3J1, ON, Canada

Abstract: Monitoring the state of the optical network is a key enabler for programmability of network functions, protocols and efficient use of the spectrum. A particular challenge is to provide the SDN-EON controller with a panoramic view of the complete state of the optical spectrum. This paper describes an architecture for compact on-chip spectrometry targeting high resolution across the entire C-band to reliably and accurately measure the spectral profile of WDM signals in fixed and flex-grid architectures. An industry standard software tool is used to validate the performance of the spectrometer. The fabrication of the proposed design is found to be practical.

Index Terms: Spectrometer, Ring resonator, Mach-Zehnder interferometer, Arrayed Waveguide Grating, Photonic integration, Optical performance monitoring, Optical transport networks.

1. Introduction

Software Defined Networking (SDN), Elastic Optical Networks (EON), and Artificial Intelligence (AI) have gained wide acceptance as they support network operators (Bell, Rogers, Verizon, etc.) in their quest to address the challenges of rapidly changing and demanding service requirements, while making efficient use of network resources [1], [2]. SDN allows programmability of network functions and protocols. EON allow the allocation of an arbitrary and appropriate spectral range and modulation format to an optical path according to application bandwidth and quality of service requirements taking into account optical physical layer attributes such as impairments [3]. AI allows the network to provision resources in response to current service requests while learning from the past to improve network efficiency and effectiveness [4].

SDNs scale by control and adaptive management, and handle changing demand and resources to achieve energy, resource efficiency and sustainability. Applying SDN principles to the physical layer that includes optical components, such as wavelength switches, fibre, add/drop mux/de-mux, amplifiers, filters, and sensors; requires fully programmable functions be they implemented in optics or electronics. As a consequence of the rigidity of the physical layer infrastructure, SDN research has focused principally on the higher digital electronic layers of the network. Applying SDN to the optical transport network could enhance both operational management in terms of cost saving and service layer performance such as fast connection turn-up, margin squeezing or health monitoring of the network. The adaptability provided from AI combined with the flexibility of SDN & EON along with the extremely fast processing capability of optical devices will transform the existing transport networks into a next-generation SDN-enabled energy efficient optical transport network.

Optical performance monitoring (OPM) is critical to this vision as it is necessary that the SDN-EON-AI controller is provided with sufficient and accurate knowledge of the state of the network to fulfill its function. Network management agents or optimization algorithms require up to date telemetry data of the network on links, components and operating points of service (WDM traffic channels in the case of transport optics). Monitoring information can be used for better resource optimization to maximize the reach versus rate. OPM information can also be used for performance prediction and planning in case of network reconfiguration, capacity scaling or network or component fault recovery. The monitoring information includes power, loss, bit-error-rate (BER), optical signal-to-noise-ratio (OSNR), electrical signal-to-noise ratio (ESNR), etc. In practice any parameter measured in the network can be used for the purpose of OPM. However, power is a strong indication of performance in optical systems as like other systems and hence OPM is used to refer to “power” in this manuscript.

Power measurement (monitoring) or spectrum sensing, while seemingly very simple and basic, is still challenging in transport optics especially in WDM networks. Typically, WDM channels are spread from 1530 nm to 1570 nm, i.e., across around 40 nm of fiber optic bandwidth. Traditional WDM channels are spaced at known and fixed locations of the WDM spectrum (50 GHz or 100 GHz ITU spectrum). However, current elastic optical networks are following more and more flex-grid channel profiles where the channel center wavelength can be at any place in the spectrum with much finer resolutions (e.g. smaller than 6.25 GHz) and they also can have different power profiles (i.e., bandwidth and power spectral density). Power measurement is done by OPM cards traditionally where a tunable filter sweeps the spectrum (C band) typically with 50 GHz resolution and hence ITU channel power readings become available. OPM cards are large; consume considerable power; and, most important, are expensive. As a result, they are only available at few points in the network. Typically, reconfigurable add-drop modules (ROADMs) are equipped with OPM cards. Since existing power measurements are based on ITU, flex ready spectrum measurements are adopted for flex grid systems. New modules capable of performing power measurement for desired location (center wavelength) and desired resolution (known bandwidth) are being used in flex-grid ready ROADM architectures. However, they still suffer from the cost issue and hence spectrum measurement is only available at add-drop nodes. ROADMs with high degrees usually share an OPM module for the purpose of spectrum measurement. This makes the OPM speed slow depending on the number of lines it supports. Amplifier nodes do not have power reading capabilities. Therefore, almost all analysis of photonic layer optimizations uses analytical, semi-analytical, or machine learned based modeling to estimate the performance of WDM channels in a section (ROADM-to-ROADM).

Reliable spectral measurement across the network is therefore a key enabling technology. Complete knowledge of the state of the network is a prerequisite to enabling SDN-EON-AI to make effective use of colour-, direction-, contention-, grid-less, filter-, gap-less ROADM, flexible channels centre frequencies and width, flexible sub-carriers in super-channels, flexible modulation formats and forward error control coding transponders, and impairment-aware wavelength routing and spectral assignment. The absence of OPM (with focus on power measurement) makes it very difficult to have reliable performance estimation or have the models trained and fed with proper live and accurate measurement across the network for the purpose of performance optimizations. Knowledge of spectral content in a section of optical networks is of great value for operators and photonics infra-structure owners.

A large variety of on-chip spectrometer designs have been unveiled and realized over the past decade such as cascaded ring resonator (RR) arrayed waveguide grating (AWG) architecture [5-6], dispersive configurations (arrayed waveguide gratings (AWG) [7], echelle gratings (EG) [7] or cascaded micro-ring resonators [8], cascaded Mach-Zehnder interferometer (MZI) based processor [9]; and discrete Fourier transform infrared spectroscopy [10]. In [5] the authors propose a combined architecture where the ring and AWGs need to be tuned to match the ring response with the AWG center wavelength. Depending on the number of channels, fixed grid reading of the spectrum is achieved. Similar to the previous prior art the authors of [6] proposed a cascaded architecture where a ring resonator (RR) is followed by a parallel pair of arrayed waveguide gratings (AWG) with different center wavelengths to reduce the cross talk. The center wavelength of the AWGs must differ by half a channel spacing for proper operation but there is no mention of if and how the whole spectrum may be scanned. When the RR is not tuned to an AWG channel passband center, the spectrometer will suffer increased insertion loss and channel leakage (cross talk) with increased detuning. In addition to that, EG and AWGs have been proposed by Xiang et al. [8] to construct spectrometers capable of operation over a broad range of different wavelength. The resolution is restricted by the number of samples of the spectrum by the fixed number of EG/AWG channels. A multiple ring resonator in cascade architecture has been proposed in [8] for high resolution spectrum measurement. These architectures have proven to be extremely complicated to control and calibrate in a reliable fashion due to the fact that two or more very sensitive components (RR) are needed to be tuned together. On the other hand, in [9] a fast-Fourier transformation (FFT)-like approach is used by performing multiple measurements of the filtered spectrum. The authors demonstrate a resolution of 23 pm (~ 2.9 GHz) over a 184 pm range about 1550 nm. Sub-GHz resolution seems to be within reach but entire C band coverage remains challenging as it requires multiple arms (up to 10) which imposes significant loss, complex control and measurement dynamics. Following a similar approach, Kita *et al*. [10] proposed a new signal processing technique performed electro-optically where a combination of numerous measurements with data processing provides the desired high-resolution power measurement across a desired band. To achieve sub-GHz resolution more than 10 stages are needed. Therefore, this strategy and architecture suffers similarly in scaling when high resolution spectrum sensing over a wide band is needed. In summary, the existing measurement technologies fail to combine acceptable resolutions with wideband operation and do not support feasible integration with other products which limits their deployment

mainly due to high cost, loss and foot print. In addition, the requirement of sub-GHz resolution bandwidth to reliably and accurately distinguish the individual carriers in a densely packed multi-carrier super-channels or to monitor the differential power of adjacent channels in fixed and flex-grid architectures with a large free-spectral range for transparent operation across the entire C band 1530 nm-1565 nm for an integrated solution remains challenging.

In this paper, the design of a technologically viable compact on-chip high-resolution wideband spectrometer is presented and verified by software simulation using an industry standard tool. A novel and original approach to coordinated tuning of the individual stages enables the spectrometer to scan the entire C-band with better than 1 GHz resolution using only three stages and two controls. The target application is to measure the spectral profile of WDM signals accurately in flex- and fixed- grid architectures across the entire C-band 1530 nm-1565 nm with minimum scan time and better than 1 GHz frequency accuracy. The photonic integration of the circuit architecture can be implemented using a mature fabrication technology; low index contrast Silica on Silica or CMOS compatible low loss Si_3N_4 photonic integration platform. However, to meet the technical specifications such as compact size and high-resolution bandwidth, the Si_3N_4 platform is preferred due to its impressive agreement between simulation and practical measurement for the components used in this design architecture [11] - [14].

2. Proposed spectrometer circuit architecture

The circuit architecture of the proposed spectrometer [15] is illustrated schematically in Fig. 1. It consists of three stages. The first stage is a ring resonator (RR) which has the function of defining the spectrometer resolution. It provides a periodic train of resonances each with bandwidth <1GHz and spaced by its free-spectral range (FSR). It is tuneable in frequency over one FSR. The final stage is an arrayed waveguide grating (AWG) which has the function of isolating one RR resonance in each output channel. Each channel has a -3dB passband width equal to half the channel spacing. The output channel frequency spacing is equal to the FSR of the RR. The central stage has the function of ensuring to a good approximation that the centre frequency of each AWG output channel passband tracks the centre frequency of their associated RR resonance. It consists of a parallel mirrored pair of nominally identical Mach-Zehnder delay interferometers (MZDI) with FSR equal to the AWG channel spacing and hence to the FSR of the RR. The construction of the MZDI can be made either by using 2×2 directional couplers or multimode interference (MMI) couplers. The four outputs of the central stage are connected via equal optical path length waveguides to four of five adjacent AWG input channels omitting the centre channel. The AWG input channel frequency spacing is equal to half the AWG output channel spacing. The Mach-Zehnder interferometer (MZI) that precedes the MZDI pair is used as a switch that selects the active MZDI and hence the active pair of AWG input channels of the four equipped AWG input channels.

The spectrometer has two controls: a first control to tune the RR and a second to toggle the MZI switch. A phase change of $\Delta\theta \in [0,2\pi]$ within the RR provided by a phase shift element is used to scan cyclically the RR resonant frequency comb over one FSR. There are two phases within this operating cycle that correspond to the state of the switch. The switch toggles at the mid-point and the end point of the scan as determined by the first control. These two controls are the only dynamic controls needed. However, it is prudent to equip the MZDI stages with quasi-static (pre-set) phase trimmers to compensate any phase bias errors due to fabrication process variations. There is some freedom of choice in the selection of the FSR and hence the total number of AWG output channels required to operate over the entire C-band. Reported experimental demonstrations of the components, our device and circuit simulations, and the

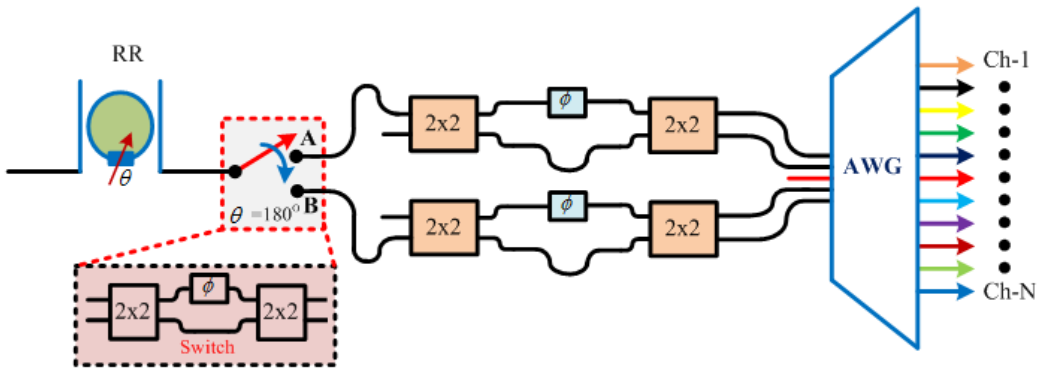

Fig. 1. Schematic of the proposed spectrometer. AWG, arrayed waveguide grating.

process development kit support the practicality of the demonstration of a spectrometer that meets the following specifications.

Table 1: Sub-system design specifications for the proposed spectrometer.

Design specifications	Comments	Remarks
RR free spectral range (GHz)	50	
MZI free spectral range (GHz)	50	Equal to the free spectral range of RR
AWG output channel spacing (GHz)	50	Equal to the free spectral range of RR
AWG output channel bandwidth (GHz)	25	Half of AWG output channel spacing
AWG input channel spacing (GHz)	25	Half of AWG output channel spacing
Number of AWG output channel	88	
Total spectrum covered (THz)	4.4	$88 \times 50 = 4400$ GHz (entire C band)

To isolate an individual RR resonance within an AWG channel, ideally the comb of AWG passband centre frequencies tracks the comb of RR resonant frequencies as the spectrometer is scanned, as illustrated schematically in Fig. 2 (a, b). The benefits of ganged tuning are: minimisation of excess loss; tuning invariant channel transmission; and, an AWG adjacent channel crosstalk that is the best value (passband centre) rather than the worst value (passband edges). During the two phases of the scan, a data acquisition system (DAQ) acquires samples of the optical power monitored by photodetectors placed at the AWG outputs. Post processing of the acquired data may be further optimized for an increased effective measurement resolution. In principle, the AWG output channel spectra may be translated in frequency by translating the input waveguide across the input aperture of its first star coupler. An optical phased array (OPA) can be used to perform the translation of the input field profile. A necessary condition is that translation per unit frequency change of the OPA output equals that of the AWG input. The OPA may be based on a secondary AWG having an FSR equal to the primary AWG output channel frequency spacing. The secondary AWG output star coupler and the primary AWG input star coupler may be merged. However, the defocus caused by opposite sign curvature of the secondary AWG image field and the principal AWG object field strictly should be compensated by a field lens within the merged couplers. An alternative more practical approach adopted in this work is to accept a discrete approximation to the translation of the input field profile and connect the two-star couplers by N waveguides of the same optical path length. In the discrete case the output channel frequency spacing of the OPA should equal the input channel frequency spacing of the primary AWG and the OPA may be implemented by a dimension N generalised Mach-Zehnder Interferometer (GMZI) rather than by a secondary AWG.

A more serious problem follows from field being split between the two extrema of the beam steering aperture at the frequency at which the field profile should fly-back. Over the fly back transition in the transmission this result, in two adjacent RR resonances being passed via the same output port giving rise to unacceptable crosstalk at the edges of the tuning range. The remedy is to use two OPA-AWG units offset in frequency and to select the unit offering low crosstalk at a particular tuning. With this expedient it is sufficient to use a Mach-Zehnder interferometer (MZI) as a dimension N=2 discrete approximation to an OPA.

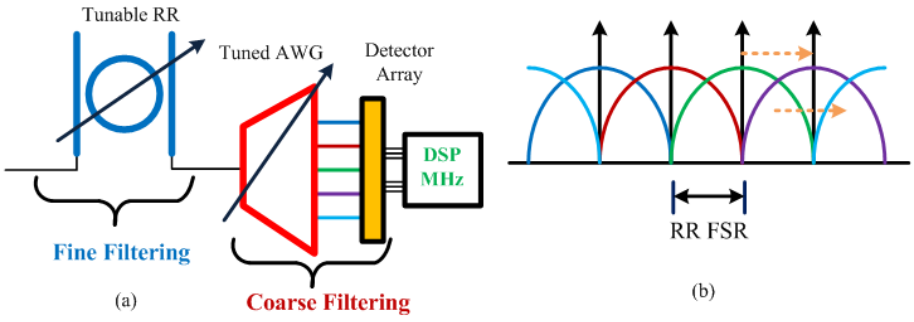

Fig. 2. (a) Tunable RR & AWG; DAQ, data acquisition; (b) Tracking of RR comb (grey arrows) & AWG channels (peaked curves).

Consider an MZI–AWG with input channel frequency spacing and output channel bandwidth equal to one half of its output channel frequency spacing $\Delta\omega$. A 2×2 MZI has an amplitude transmission matrix:

$$T_{MZI} = \begin{bmatrix} \sin(\varphi/2) & \cos(\varphi/2) \\ \cos(\varphi/2) & -\sin(\varphi/2) \end{bmatrix} \quad (1)$$

where φ is the phase imbalance between its arms. It is easily verified that this transmission matrix satisfies energy conservation. Fig. 3 shows the basic amplitude transmission of an MZI, when light is launched from different input ports.

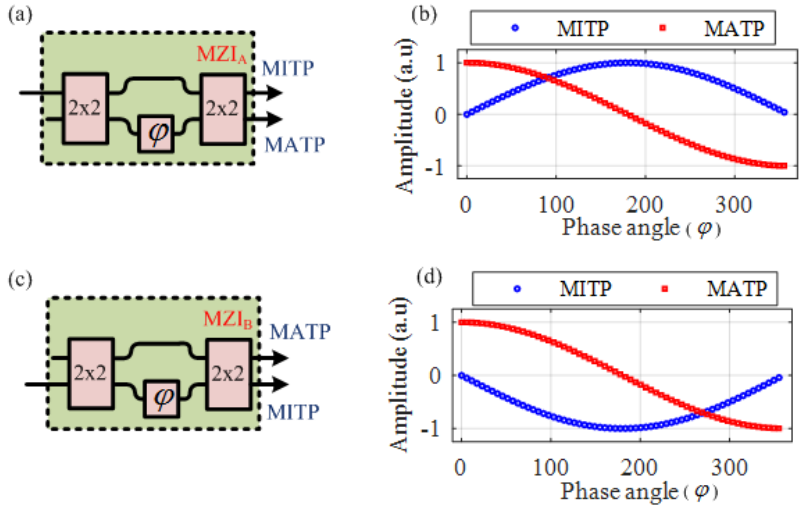

Fig. 3. Schematic of an MZI with input from upper port (a) and lower port (c); and corresponding (b) & (d) amplitude transmission plot. MITP, minimum transmission point; MATP, maximum transmission point.

The period of the *amplitude* transmission matrix defined by Eq. 1 is 720 degrees. However, the phase imbalance of the arms leads to an $\exp(\varphi/2)$ scalar pre-multiplier neglected in Eq. 1 which ensures the overall MZI is invariant to a 360˚-degree change of φ. Accordingly, Fig 3(b) and (d) are only shown over a range of 360 degrees. Take the MZI port with $\cos(\varphi/2)$ dependence to be connected to the reference input channel of the AWG and the MZI port with $\sin(\varphi/2)$ dependence to be connected to the upshifted frequency input channel.

The amplitude transmission of a given output port is:

$$T_{AWG}(\omega) = H(\omega)\cos(\varphi/2) + H(\omega - \Delta\omega/2)\sin(\varphi/2) \quad (2)$$

where $H(\omega)$ is the transmission function of an AWG which may be taken as real to good accuracy and ω is the frequency offset from the centre of the passband. Now let us consider that $\varphi = \omega\tau$, where $\tau = 2\pi/\Delta\omega$, is the delay that must be applied in one of the arms of the MZI and $\Delta\omega$ is the AWG channel frequency spacing. The transmission at selected values of detuning is given by Table 2.

Table 2. Transmission of the MZI$_A$-AWG output channel for MZI$_A$ phase bias variation from 0° to 360°.

AWG transmission	ω						Remarks
	0	$\Delta\omega/4$	$\Delta\omega/2$	$-\Delta\omega/2$	$-\Delta\omega/4$	$\Delta\omega$	The AWG tracks the RR resonant frequency correctly over the first half of the RR/MZI FSR only corresponding to MZI$_A$ bias 0° to 180°
$T_{AWG}(\omega)$	1	1	1	-1	0	1	

When $\omega\tau = 0$ ($\varphi = 0$), as per Fig. 3(b) the MATP port is active only, hence the amplitude transmission of the AWG is only $H(\omega)$. For $0° < \varphi < 180°$, the amplitude transmission of the MZI output ports have the same sign and there is constructive interference between the superimposed AWG amplitude transmissions. This corresponds to the desired

frequency tracking behavior as summarised by Table 2. As the input channel frequency spacing of the AWG is set to 25 GHz, the MZI-AWG combination track over half of the output channel frequency spacing. When $180° < \varphi < 360°$, as shown in Fig. 3(b) the amplitude transmission of the MZI are opposite in sign resulting in destructive interference between the superimposed AWG amplitude transmissions. As a result, the remaining half the FSR is taken up by the undesired fly-back response.

The fly-back may be corrected using an alternative MZI_B-AWG arrangement with the MZI port with $\cos(\varphi/2)$ dependence connected to the reference input channel of the AWG and the MZI port with $-\sin(\varphi/2)$ connected to the upshifted frequency input channel. As shown in Fig. 3(d), the amplitude of the MZI output ports have the same sign and create constructive interference between the superimposed AWG amplitude transmission for $180° < \varphi < 360°$. The new form of the previously described amplitude transmission at the same output port becomes,

$$T_{AWG}(\omega) = H(\omega)\cos(\varphi/2) - H(\omega - \Delta\omega/2)\sin(\varphi/2) \tag{3}$$

The frequency tracking behavior of the MZI_B-AWG arrangement is summarised in the Table 3 and can be seen to be complementary to the frequency tracking behavior of the MZI_A-AWG arrangement summarised in Table 2: when MZI_A-AWG commences fly-back, MZI_B-AWG tracks correctly and vice versa.

Table 3. Transmission of MZI_B-AWG output channel for MZI_B phase bias variation from 0° to 360°.

AWG transmission	ω						Remarks
	0	$\Delta\omega/4$	$\Delta\omega/2$	$-\Delta\omega/2$	$-\Delta\omega/4$	$\Delta\omega$	The AWG tracks the RR resonant frequency correctly over the second half the RR/MZI FSR only corresponding to MZI_B bias 180° to 360°
$T_{AWG}(\omega)$	1	0	-1	1	1	1	

Fig. 4(a-b) depicts the combination of the MZI_A-AWG and MZI_B-AWG with the simulated (i-x) frequency tracking behavior at different MZI phase bias. As found in the earlier analysis, the MZI_A-AWG combination tracks the RR resonance frequency correctly up to $\Delta\omega/2$ or 180˚ phase bias of the MZI_A, whereas MZI_B-AWG tracks the RR resonance frequency correctly from 180˚ to 360˚ phase bias. A phase bias ranging from 180˚ to 360˚ is equivalent to a phase bias ranging from 180˚ to 0˚. Consequently, the circuit architectures track in opposite directions the same 0 GHz to 25 GHz span of the 50 GHz channel frequency spacing. To overcome this problem, the resolution during the fly-back phase MZI_A-AWG is to hand over to an alternative MZI_B-AWG with the MZI port with $\cos(\varphi/2)$ dependence connected to the reference input channel of the AWG and the MZI port with $-\sin(\varphi/2)$ dependence connected to the downshifted frequency input channel of the AWG. This arrangement advantageously eliminates the cross-over interconnection. The amplitude transmission at the same output port is modified to:

$$T_{AWG}(\omega) = H(\omega)\cos(\varphi/2) - H(\omega + \Delta\omega/2)\sin(\varphi/2) \tag{4}$$

which during the fly-back phase of MZI_A gives the desired frequency tracking over the -25 GHz to 0 GHz span of the 50 GHz channel frequency spacing:

$$\begin{aligned} T_{AWG}(\omega) &= 1 \quad \omega = -\Delta\omega/2 \\ T_{AWG}(\omega) &= 1 \quad \omega = -\Delta\omega/4 \\ T_{AWG}(\omega) &= 1 \quad \omega = 0 \end{aligned} \tag{5}$$

Note that at $\omega = 0, \pm\Delta\omega/2$, where handover occurs the two MZI-AWG channel outputs agree. Consequently MZI_A-AWG and MZI_B-AWG combine with handover to successfully track the full span (-25 GHz to +25 GHz) of the channel frequency spacing (50 GHz). To economise on hardware, one would like to use a switch to select the MZI input port and rearrange the connection of its two outputs between a three input AWG as shown in Fig. 5. However, a switch to rearrange the MZI outputs could introduce phase errors. It is consequently preferable to use two nominally identical MZDI to drive two pairs of adjacent ports separated by an unequipped central input port of a 5-input port AWG as shown in Fig.1. The handover is then between the set of output ports and the same set displaced by one port. The data acquisition system can resolve this shift trivially.

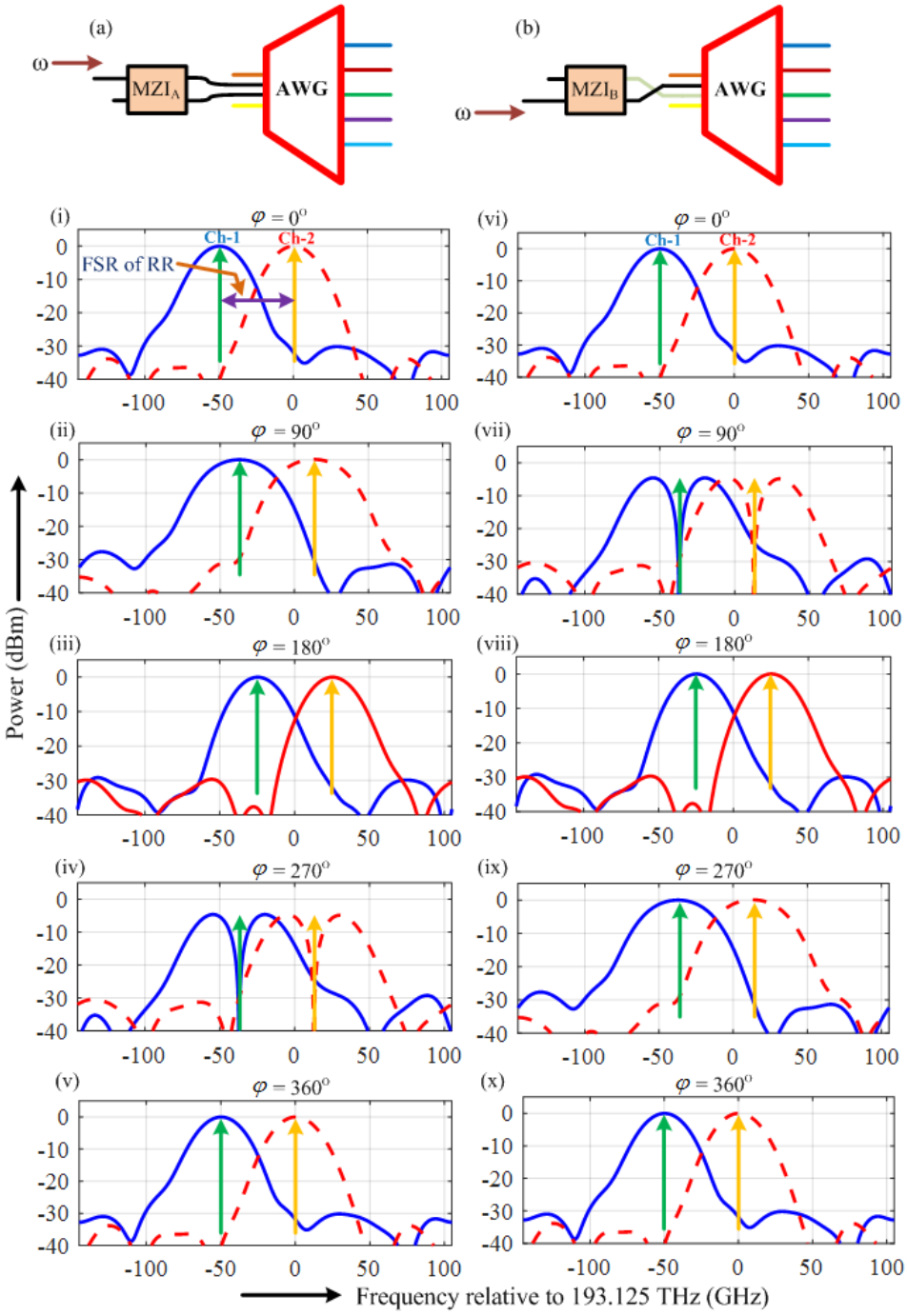

Fig. 4. MZI-AWG combination to correct the fly-back problem; (a) light is injected from the upper input port with corresponding amplitude transmission (i—v) of MZI$_A$-AWG combination at different phase bias; (b) light is injected from the lower input port with amplitude transmission(vi —x) of MZI$_B$-AWG combination at different phase bias of the MZI.

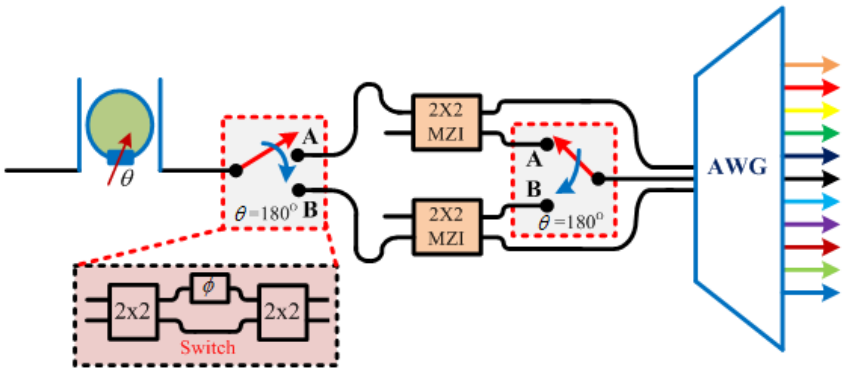

Fig. 5. Schematic diagram of the circuit architecture that can overcome the fly back problem and track the whole FSR of the RR.

The simulated output channel spectra of the AWG for a wide range of frequencies is shown in Fig. 6. The spectra shown in Fig. 6 provide intuition that the spectrometer may be understood as an RR working into a pair of passband-flattened AWGs with interleaved output channel spectra. However, this does not imply that any approach to a passband flattening mechanism will suffice. The mechanism of choice is ganged tuning of the RR and AWG via (a good approximation to) translation of the input across the aperture of the first star coupler. This mechanism offers not only the best of low adjacent channel leakage found at the centre of channel passband rather than the worst of adjacent channel leakage found at the edges of the channel of the basic AWG but also it offers a means to merge the two interleaved AWGs into a single consolidated AWG which halves the number of output channels; the number of photodetectors; and the footprint size otherwise required.

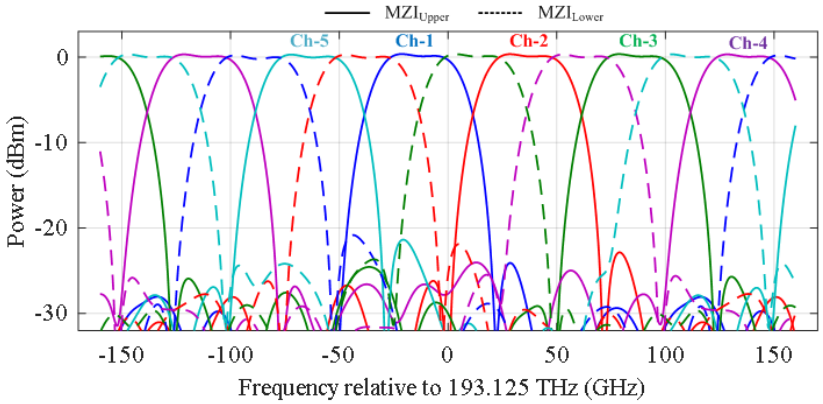

Fig. 6. AWG output channel spectra when both MZDI are auto-tuned by a delay line with an FSR equal to the AWG output channel frequency spacing. The channel spectra corresponding to the two different switch states are interleaved.

3. Simulation results

VPIphotonics software simulation is used to validate the theoretical prediction. Fig. 7. shows a schematic of the spectrometer stripped of the RR and with waveguide delay-lines and frequency independent static phase shift elements denoted by the symbol τ. The phase shifts are adjusted manually to bias the upper and lower MZI stages and to switch between them. The switch is used to select the upper MZI (MZI_A) in the first phase illustrated in Fig. 4(i-v) and the lower MZI (MZI_B) in the second phase illustrated (Fig. 4(vi-x)). For better understanding the concept, a 5 channel AWG with an FSR of 250 GHz (5×50 GHz) is used for simulation.

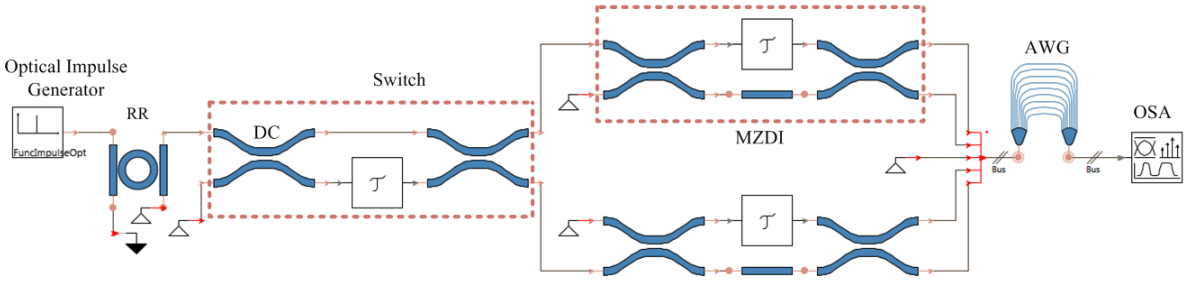

Fig. 7. VPI schematic of a circuit architecture for the purpose of demonstrating the operational principles by simulation; DC, directional coupler; OSA, optical spectrum analyzer.

To achieve auto-tuning the phase-shift elements presents in Fig. 4, are replaced by the delay lines. In this case (50 GHz output channel frequency spacing) the delay is chosen to set an FSR of 50 GHz. Fig. 8. shows the output of the AWG when both MZI are auto-tuned in this way. The flat passband and steep transitions between pass and reject

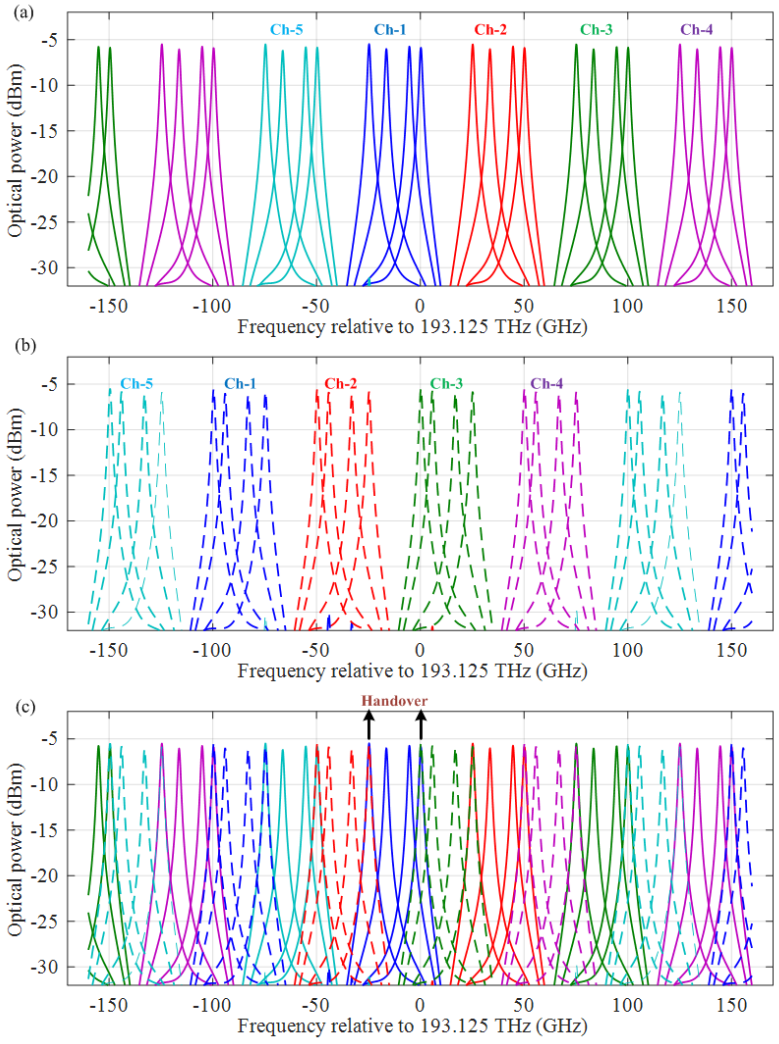

Fig. 8. A simulation of the complete spectrometer circuit with the MRR in place (as in Fig. 1) illustrating operation over complete scanning cycle over the full 50 GHz RR FSR. (a) Upper MZDI selected phase of scanning cycle; (b) lower MZDI selected phase of scanning cycle; (c) full scanning cycle.

bands are notable. The channel spectra corresponding to the two different switch states are interleaved. In the proposed architecture, only the RR will be tuned over one FSR for spectral sensing. One phase shifter for each MZI is included to align the MZI FSR with the AWG output channel spectra. It remains constant once the alignment (if required) is done. Fig. 8. illustrates the output channel spectra over the full scanning cycle of the proposed spectrometer obtained by tuning the RR over one FSR. The switched MZDI-AWG succeeds in isolating one RR resonance with sub-GHz bandwidth within each AWG channel; the peak of the resonance is substantially constant as the ring resonance frequency is scanned across its 50 GHz FSR thereby providing a continuous spectrum across the whole operating band; and, the adjacent channel crosstalk is negligible. It may be observed that the selection of the upper MZI provides a flat response over half the channel frequency spacing corresponding to a phase bias of 0 to $-\pi$ radians and selection of the lower MZI provides a flat response over the remaining half of the channel frequency spacing corresponding to a phase bias of $-\pi$ to -2π radians. Moreover, the readings of either selection agree at the two handover transitions in the scanning cycle one at a phase bias of 0, -2π and one at a phase bias of $-\pi$. The contiguous flat response across the band is a noticeable feature.

4. Discussion

A combination of software simulation is used to study further the integration feasibility of the proposed architecture. VPIphotonics is used for the circuit simulation whereas, Photon Design along with MATLAB is used to verify the function of the individual components that comprise the architecture. The simplicity of the structure (3-stages) and control (2-controls) renders practical implementation as a single photonic integrated circuit. The proposed spectrometer can be fabricated in any mature fabrication platform. However, the resolution bandwidth of the spectrometer primarily depends on the insertion loss (dB/turn) of the RR. An integration platform supporting loss-loss waveguides and careful attention to the design of the RR couplers to minimise their excess loss are therefore paramount. Hence in order to meet the specification of the proposed spectrometer, the CMOS compatible Si_3N_4 photonic integration platform has been selected as it offers low loss, tight confinement, low dispersion and a mature thermo-optic phase shifter technology. There are ample reports in the literature of the technological verification of SSC, MMI, tunable RR, and sub-circuits such as MZ(D)I [11]-[13] and modest port count AWG fabricated using the Si_3N_4 integration platform [14].

For effective use of resources, the fabrication plan envisaged access to multi-project wafer MPW runs for test structures followed by a custom wafer run for fabrication of prototypes for demonstration. The LioniX Triplex technology chosen only offers MPW runs for designs using the asymmetric double strip (ADS) waveguide and the low-cost photolithography used has a minimum feature size of 1 um. Accordingly, the simulations of the components and sub-circuits that constitute the proposed spectrometer are designed using ADS as reference waveguide. The

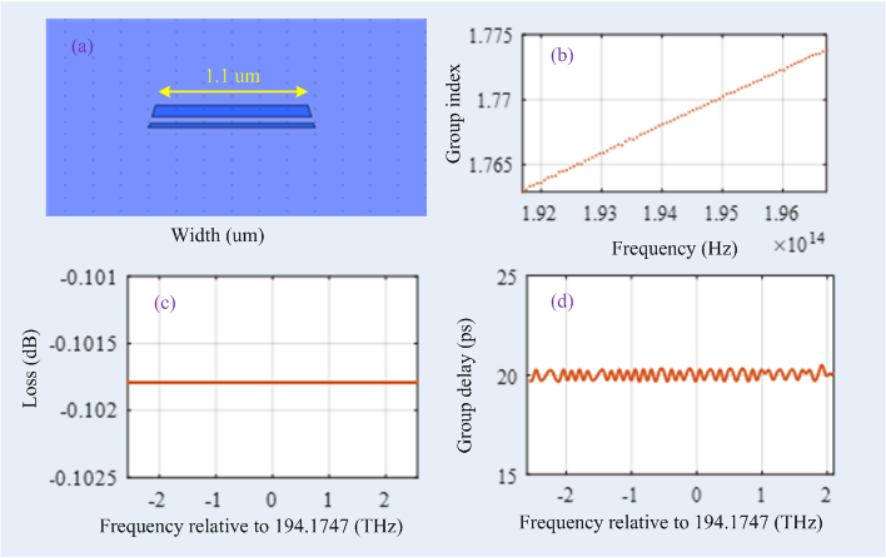

Fig. 9. (a) The reference ADS waveguide with width $w = 1.1\ \mu m$ simulated shown in the FIMMPROP device window; (b) fundamental TE-like mode group index versus vacuum wavelength across the C-band; (c) simulated waveguide loss for a straight waveguide having length of $l = 3392.878\ \mu m$; (d) simulated group delay caused by the same waveguide mentioned in (c).

reference ADS used is shown in Fig. 9(a) where the width of the top side of the upper strip is 1.1 um and the etching results in sidewalls inclined at 82° relative to the horizontal axis. The Photon Design software tool FIMMWAVE was used to acquire the characteristics of the waveguide in the C-band. Simulations all use the TE-like mode as it is more tightly confined and hence exhibits slightly lower bend loss than the TM mode.

The effective group index of the mode is illustrated in Fig. 9(b) and has a value of 1.7725, 1.76841 and 1.7629 at the short wavelength edge (1530 nm), centre wavelength (1545 nm), and the longer wavelength (1565 nm) edge of the C-band respectively. The major contributing mechanism is waveguide dispersion; the contribution of material dispersion is negligible in comparison. The phase shift φ contributed by a waveguide delay line of length l as a function of optical frequency ω is given by:

$$\varphi(\omega) = n_e(\omega)(l/c)\omega \tag{6}$$

where n_e is the mode effective index and c is the vacuum velocity of light. At frequencies in a neighborhood of a reference frequency ω_0 the frequency dependence of the optical path length is well approximated its Taylor series up to second order:

$$\varphi(\omega) \approx \varphi_0 - \tau(\omega - \omega_0) - \tau' \frac{1}{2}(\omega - \omega_0)^2 \ldots \tag{7}$$

where:

$$\begin{aligned} \varphi_0 &= n_e(\omega_0)(l/c)\omega_0 \\ \tau &= n_g(\omega_0)(l/c) \\ \tau' &= n_g'(\omega_0)(l/c) \end{aligned} \tag{8}$$

and n_g, n_g' are the mode group index and mode group index dispersion respectively. The phase bias φ_0 is equal to the phase shift evaluated at the reference frequency, τ is the group delay evaluated at the reference frequency and τ' is the group delay dispersion given by the slope of the group delay versus optical frequency.

The phase bias is sensitive to subwavelength errors in the optical path length $n_e(\omega_0)l$. A means of trimming or tuning the phase bias may therefore be necessary to correctly set the operating point of interferometric components. The free-spectral range is the frequency interval over which the phase shift changes by 2π and assuming small dispersion is given by:

$$FSR(\omega) = c/n_g(\omega)l \tag{9}$$

The dispersion results in a small change over the band of the local value of the FSR. The FSR at the reference frequency defines a regular frequency grid over the whole band. The optical path length l is calculated as 3392.878 um at the reference frequency 194.1747 THz (wavelength of 1545.0 nm). Fig. 9(c) shows the simulated total waveguide loss for the optical path length l. A loss of 0.3 dBcm^{-1} is considered in the simulation as conservative assumption albeit $0.1 - 0.2\ dBcm^{-1}$ is reported in the chosen platform. In the presence of dispersion, the frequencies where the phase shift returns to the value of the phase-bias position are offset from the grid because of the dispersion. Figure 9(d) shows the simulated group delay for the whole C-band. It shows that the group delay offset by $\pm 0.3\ ps$ from its average value 20 ps (50 GHz) due to waveguide dispersion. As such the FSR differ around 100 MHz from its design value, i.e 50 GHz.

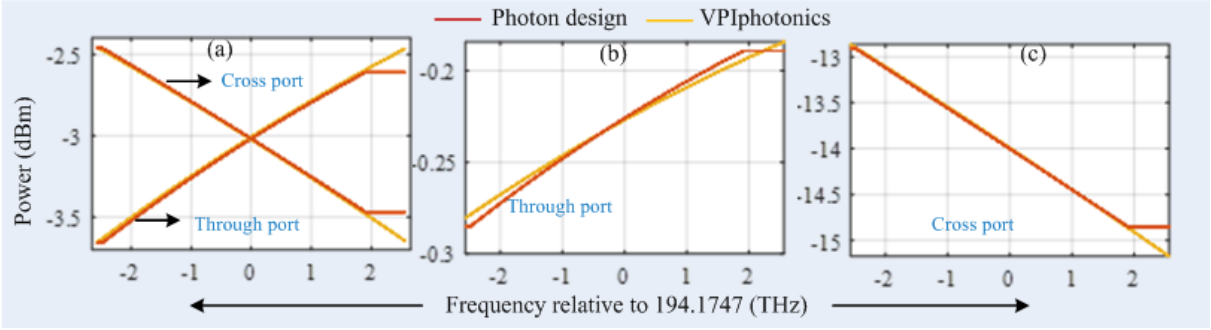

Fig. 10. (a) Power splitting of a nominally 3dB directional coupler over the C-band for ADS waveguides and TE polarisation; (b-c) power splitting of a directional coupler used in the RR over the C-band. An input power of 0 dBm for all the samples over the C-band is used for the simulation.

The spectrometer circuit shown in Fig. 1 contains a total of three MZI sub-circuits (an MZI switch that selects one of two MZDI AWG passband flattening sub-circuits) formed by a total of six 2×2 3dB couplers. A 2×2 multimode interference coupler (MMI) can also be an ideal candidate for the 3 dB couplers. However, LioniX advised, for their integration platform, the excess insertion loss of MMI is much higher than directional couplers (DC). Simulations confirm that, with careful design for this platform, the excess loss of a DC is negligible ($< 0.1\ dB$) comparison to an MMI (<1dB). However, the spectrometer circuit must operate successfully over the whole extent of the C-band. Deviations of the splitting ratio from 50:50 of 3dB couplers impacts adversely on the channel leakage of the spectrometer and consequently the wavelength dependence of the splitting ratio of the 3dB couplers is an important consideration. Fig. 10 (a) shows the power splitting ratio of the designed DC. First of all, the DC coupler is designed using Photon Design software tool for the reference ADS waveguide. Later on, a frequency dependent coupling coefficient is defined in VPI using the PYTHON language to emulate the findings using Photon Design. The flat power splitting at the right edge of the picture is just a continuation from the end of the frequency dependent splitting modelled in the PYTHON script. The frequency dependent coupling coefficient is defined till 194.1747+2 THz. It shows that both simulations match each other well. Furthermore, it is also noted that the wavelength dependence of the splitting ratio of an MZI sub-circuit formed by a pair of DC interconnected with a pair of waveguide arms may be engineered to be maximally flat by appropriate adjustment of the lengths of the DC and the path imbalance between them [16]. Fig. 10 (b-c) shows the simulated through port and cross port coupling of the directional coupler used in the ring resonator. The power splitting ratio is used as 94.92% and 3.98% at the design wavelength $1545\ nm$. For an FSR of 50 GHz at $1545\ nm$ the ADS waveguide ring circumference is calculated to be $3.3928\ mm$ corresponding to a ring radius of $539.99\ \mu m$. The bend loss of an ADS waveguide bend of this radius of curvature is negligible over the C-band; the mode is fully bound by the waveguide bend and the only terms contributing loss are absorption and scattering loss. Detailed data on absorption and scattering loss is not available beyond the disclosure that the total waveguide loss is circa $0.1 - 0.2\ dB\ cm - 1$ for a ring of $50 - 100$ µm radii. As a conservative assumption, the waveguide loss is considered as $0.3\ dB/cm$ in the simulation. Fig. (11) shows the transmission of the RR. The zoom-out inset shows that the FSR is slightly offset from the 50 GHz grid at the edges of the band. Furthermore, the peak transmission is not constant throughout the C-band, it varies 1-1.25 dB from one edge of the C-band to the other edge.

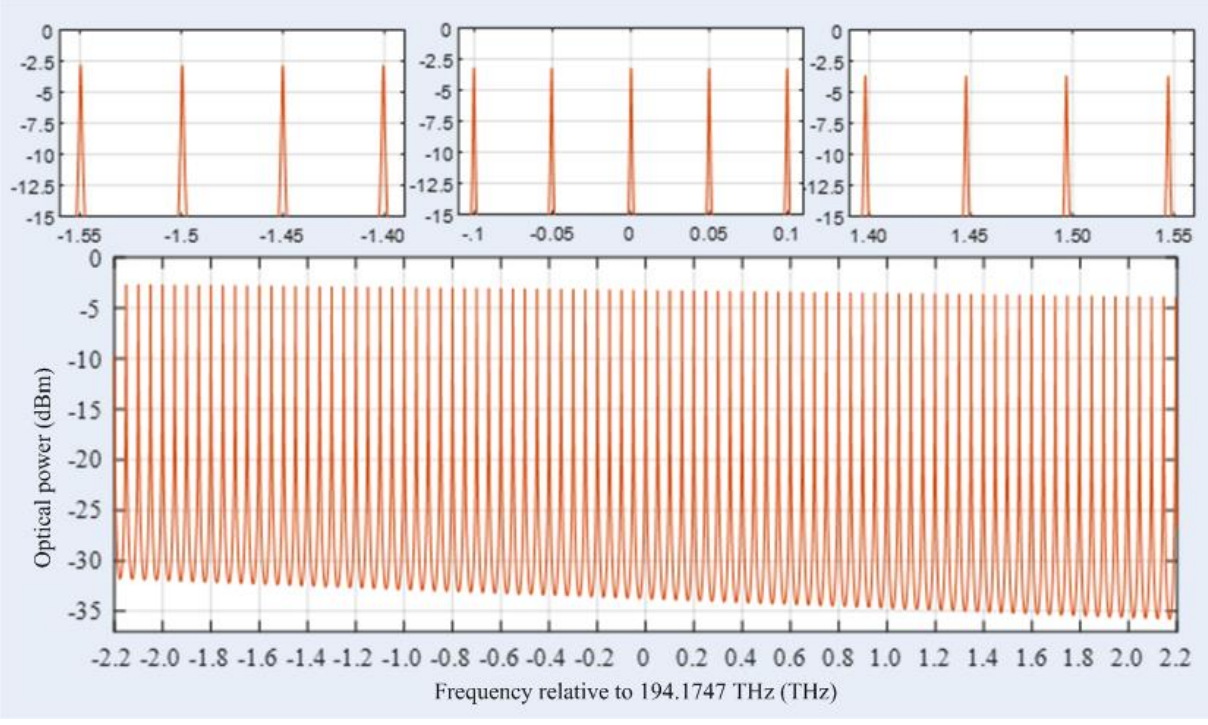

Fig. 11. The transmission of a ring resonator predicted by VPI simulation. The in set shows the zoom-in transmission at the smaller wavelength, center wavelength and longer wavelength. The coupler used has excess loss of 1.1%, cross-coupling of 3.98% and hence through-coupling of 94.92% at the design wavelength. The waveguide loss is 0.3 dB/cm. The resulting FWHM bandwidth is (≤1 GHz) and insertion loss is 3.2 dB.

This peak transmission follows the cross-coupling characteristic curve of the DC used in the RR. The resulting resolution bandwidth is found to be around 1 GHz and the insertion loss is 3.2 dB at the design wavelength.

Ring resonators fabricated via the LioniX MPW run will be tuned by thermo-optic phase shift elements which use chromium metal films deposited on top of the cladding at a distance of roughly 8 μm from the waveguide core as the heating element. The chromium films have 150 nm thickness and 20 μm width and are conveniently located on the over-cladding immediately above the waveguide core section in order to ensure maximum heat transfer. The heat increases the temperature of the waveguide causing a change in effective refractive index of the mode due to the temperature dependence of the refractive indices of core and cladding materials. The change of mode effective index in turn shifts the resonant frequency of the ring.

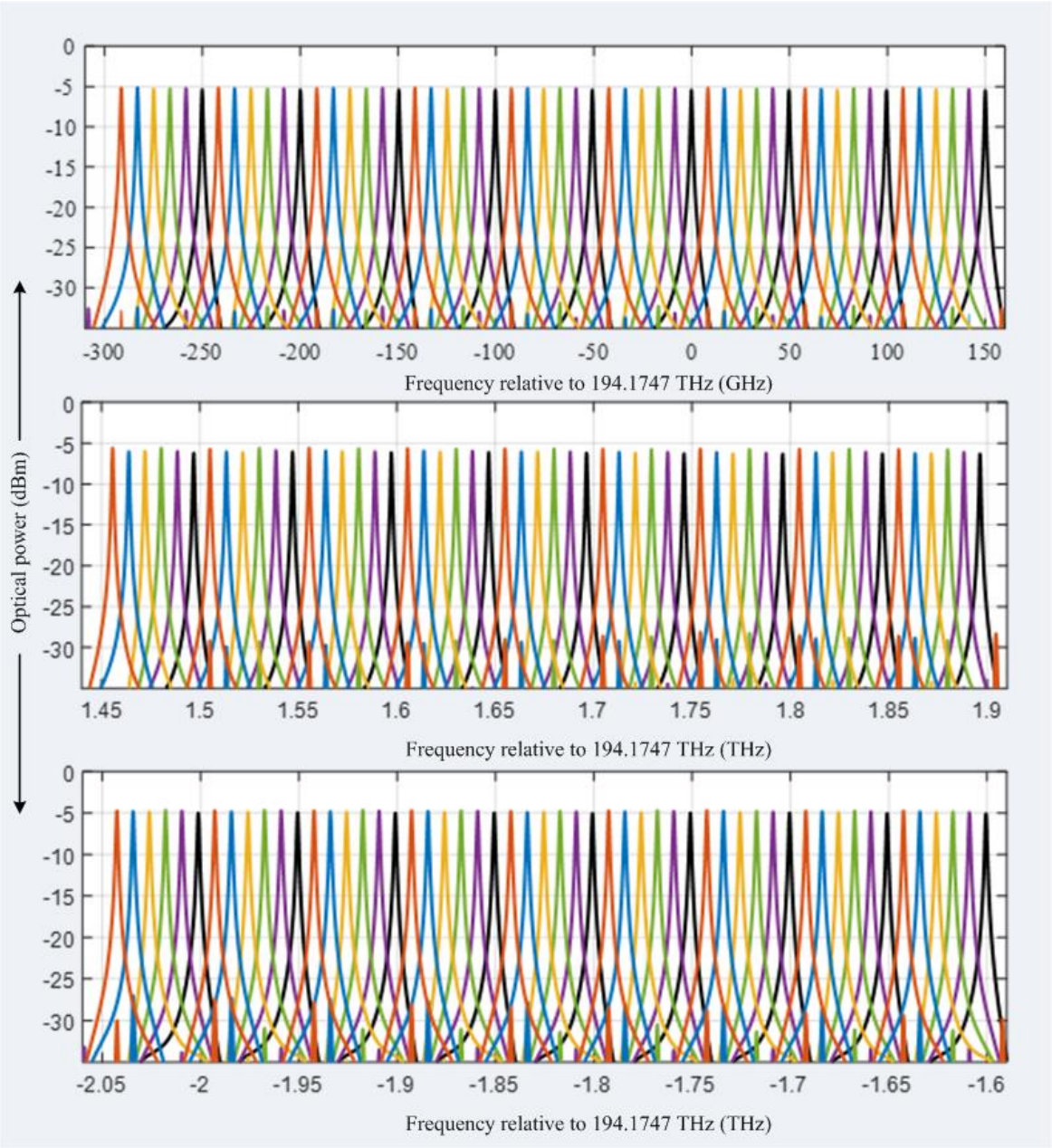

Fig. 12. Full scanning cycle of the spectrometer at the center of the C-band (top), lower wavelength edge (middle) and longer wavelength edge (bottom).

The MPW process offers no design freedom in respect of this structure such as the use of deep trenches to prevent heat spreading. A high bit (≥ 8) digital to analog converter (DAC) with moderate sampling rate ($\sim 256\ kbit/s$) will be used to precisely tune the RR over one FSR. However, electro-optic tuning offer greater efficiencies, such as low drive voltage, high extinction ratio, low drive power, linear voltage to index relationship [17]. Tuning by means of Piezo-electric actuator is found to be efficient as well [18].

A stigmatic imaging methodology has been adopted for preliminary AWG design to avoid prolonged and complex simulations when making small adjustments. For stigmatic images, the AWG channel passband characteristics are determined entirely by the transmission of an offset junction between an input (Tx) and output (Rx) waveguide respectively. Seyringer has reported impressive agreement of simulations and experimental measurements of a 160×50 GHz AWG fabricated in Si_3N_4 with footprint of ~ $1cm^2$ [14]. Her biomedical sensing application dictates the operating center vacuum wavelength of 850 nm. However, a reference design for $850\ nm$ may be mapped to $1550\ nm$ by increasing all dimensions by a factor of 1.8 at least as a good starting point for further optimisation. Moreover, the spectrometer requires almost half the number of output channels which will scale down the footprint. Finally, VPI circuit simulation is used to evaluate the overall performance of the proposed circuit. An AWG having 80 output ports with $50\ GHz$ FSR is used in the circuit simulation. An AWG insertion loss of 5 dB is considered representative, while a random 100 MHz offset/shift from the $50\ GHz$ FSR is applied to emulate the fabrication error. The RR, DC and MZI is configured as depicted earlier in the discussion part. It is reasonable to assume that all directional couplers on the same integrated circuit have similar extinction ratio as Yamazaki et al. [19] obtained less than 0.5 dB loss variation among 4 Mach Zehnder Modulators (MZMs). An optical source covering the whole C-band with power of 0 dBm for all the samples is used as input. The spectrometer performs excellently albeit the crosstalk is increased by 2-5 dB at some points. Nevertheless, a crosstalk of -22 dB or less is obtained as shown in Fig. 12. Again, the peak power flatness lies within 1 dB.

The entire operation of the proposed circuit requires four controls; two static and two dynamic. As per the 1st term of Eq. (8), the two MZI connected to the AWG will have phase bias at the design wavelength. Hence, phase tuning is required to align the FSR of the MZI with the channel spectra of the AWG. Once this is done, it will remain static for the whole operation. Light can be launched using the unused port of the switch to complete this adjustment. Out of the two-dynamic control, one will tune the RR over one FSR and other will trigger the switch at the predefined position. Table 4 shows the operation of the switch:

The handover of the switch is not strictly restricted to Table 4. If we look closely at the ganged MZI-AWG spectra, there is ample liberty for the switching operation. The switch does not need to toggle at the exact 180° and 360° (or 0°) position of the RR. Rather there is a window of 5 GHz to make this switching operation with negligible power penalty. This redefines switching range $180 \pm 15^\circ$. An integrated wave meter as presented in [20], will be used to monitor the position of each resonance within an AWG channel. The wave meter circuit consist of a 2×2 directional coupler (or 2×2 MMI) and a 3×3 MMI (with its middle input port unused) that forma two-arm interferometer with a delay imbalance. When driven by a source with a narrow spectral line shape, in the present case a RR resonance within an AWG channel passband it generates sinusoidal interference fringes when the frequency is scanned. The phase of the fringe is a measure of the position of the spectral line within the FSR of the interferometer. The 3×3 MMI introduces 120° phase shifts between three copies of the intensity fringes measured at its three outputs, which enables an accurate estimate of the frequency of the spectral line independent of the input intensity and robust to component impairments

Table 4. Operation of the switch

RR position	Switch position	Remarks
0° to 180°	A (Fig.1)	Upper MZI is in operation
180° to 360°	B (Fig. 1)	Lower MZI is in operation

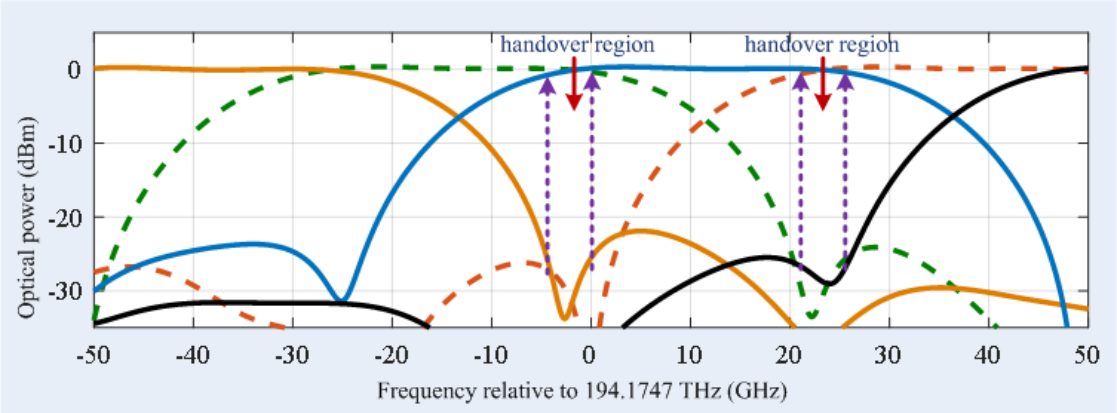

Fig. 13. Zoom-out view of MZI-AWG interlaced spectra to find out exact switching position.

5. Conclusion

In summary, a state of the art on-chip spectrometer with sub-GHz resolution over the entire C-band in a compact footprint has been proposed and verified by simulation in this article. To the best of the authors knowledge there have been no reports of simulation or experimental studies of a sub-GHz integrated spectrometer operating over the entire C-band and the solution proposed herein is unique. The proposed circuit architecture is feasible for photonic integration in the CMOS compatible Si_3N_4 platform owing to its low loss mature technology.

Acknowledgment

Mehedi Hasan acknowledges the Natural Sciences and Engineering Research Council of Canada (NSERC) for their support through the Vanier Canada Graduate Scholarship program. Mehedi Hasan is grateful to Eugene Sokolov, Photonics Application Engineer, VPIphotonics for detail discussion about component modelling in VPI photonics software. Trevor J. Hall is grateful to Huawei, Canada for their support of this work. Trevor J. Hall is also grateful to the University of Ottawa for their support of a University Research Chair.

References

[1] S. Gringeri, N. Bitar, and T. J. Xia, "Extending software defined network principles to include optical transport," *IEEE Communications Magazine*, vol. 51, no. 3, pp. 32-40, Mar. 2013.

[2] A. Aguado, M. Davis, S. Peng, M. V. Alvarez, V. Lopez, T. Szyrkowiec, A. Autenrieth, R. Vilalta, A. Mayoral, R. Munoz, R. Casellas, R. Martınez, N. Yoshikane, T. Tsuritani, R. Nejabati, and D. Simeonidou, "Dynamic virtual network reconfiguration over SDN orchestrated multitechnology optical transport domains," *J. Lightw. Techn.*, vol. 34, no. 8, pp. 1933-1938, Apr. 2016.

[3] O.G. Dios, R. Casellas, F. Paolucci, A. Napoli, Ll. Gifre, S. Annoni, S. Belotti, U. Feiste, D. Rafique, M. Bohn, S. Bigo, A. Dupas, E. Dutisseuil, F. Fresi, B. Guo, E. Hugues, P. Layec ,V. Lopez, G. Meloni, S. Misto, R. Morro, T. Rahman, G. Khanna, R. Martínez, R. Vilalta, F. Cugini, L. Poti, A. D'Errico, R. Munoz, Y. Shu, S. Yan, Y. Yan, G. Zervas, R. Nejabati, D. Simeonidou, L. Velasco, and J. Fernandez-Palacios, "First demonstration of multi-vendor and multi-domain EON with S-BVT and control interoperability over pan-European testbed," *European Conference on Optical Communications (ECOC)*, Valencia, Spain, pp. 1-3, Sep. 2015.

[4] F. Meng, S. Yan, R. Wang, Y. Ou, Y. Bi, R. Nejabati, and D. Simeonidou, "Robust self-learning physical layer abstraction utilizing optical performance monitoring and Markov chain Monte Carlo," *European Conference on Optical Communications (ECOC)*, Gothenburg, Sweden, pp. 1-3, Sep. 2017.

[5] B. Kyotoku, L. Chen, and M. Lipson, "Sub-nm resolution cavity enhanced micro-spectrometer," *Opt. Express*, vol. 18, no. 1, pp. 102-107, Jan. 2010.

[6] G. Yurtsever, and R. Baets, "Integrated spectrometer on silicon on insulator," *16th Annual Symposium of the IEEE photonics*, Ghent, Belgium, pp. 273-276, 2011.

[7] E. Ryckeboer, A. Gassenq, M. Muneeb, N. Hattasan, S. Pathak, L. Cerutti, J.B. Rodriguez, E. Tournié, W. Bogaerts, R. Baets, and G. Roelkens, "Silicon-on-insulator spectrometers with integrated GaInAsSb photodiodes for wide-band spectroscopy from 1510 to 2300 nm," *Opt. Express*, vol. 21, no. 5, pp. 6101-6108, Mar. 2013.

[8] C. Xiang, P.A. Morton, J. Khurgin, C. Morton, and J. E. Bowers, "Widely tunable Si_3N_4 triple-ring and quad-ring resonator laser reflectors and filters," *IEEE 15th International conference on group IV photonics*, Cancun, Mexico, pp. 1-2, Aug. 2018.

[9] Y. Li, J. Li, H. Yu, H. Yu, H. Chen, S. Yang, and M. Chen, “On-chip photonic microsystem for optical signal processing based on silicon and silicon nitride platforms,” *Advanced Optical Technologies,* vol. 7, no. 1-2, pp. 81-101, Apr. 2018.

[10] M. Kita, H. lin, A. Agarwal, K. Richardson, I. Luzinov, T. Gu, and J. Hu, "On-chip infrared spectroscopic sensing: Redefining the benefits of scaling," *IEEE J. Sel. Topics in Quantum Electron.*, vol. 23, no. 2, pp. 340-349, Sep. 2017.

[11] C. G. H. Roeloffzen , M. Hoekman , E. J. Klein, L. S. Wevers, R. B. Timens , D. Marchenko, D. Geskus, R. Dekker, A. Alippi, R. Grootjans, A. V. Rees , R. M. Oldenbeuving, J. P. Epping, R. G. Heideman, K. Wörhoff, A. Leinse, D. Geuzebroek , E. Schreuder, P. W. L. Van Dijk, I. Visscher, C. Taddei , Y. Fan , C. Taballione, Y. Liu , D. Marpaung , L. Zhuang , M. Benelajla, and K.-J. Boller, “Low-loss Si_3N_4 TriPleX optical waveguides: Technology and applications overview,” *IEEE J. Sel. Topics in Quantum Electron.*, vol. 24, no. 4, pp. 1-21, Jan. 2018.

[12] L. Zhuang, D. Marpaung, M. Burla, W. Beeker, A. Leinse, and C. Roeloffzen, "Low-loss, high-index-contrast Si_3N_4/SiO_2 optical waveguides for optical delay lines in microwave photonics signal processing," *Opt. Express*, vol. 19, no. 23, pp. 23162-23170, Nov. 2011.

[13] Y. Xie, L. Zhuang, and A. Lowery, “Picosecond optical pulse processing using a terahertz-bandwidth reconfigurable photonic integrated circuit,” *Nanophotonics*, vol. 7, no. 5, pp. 837-852, May 2018.

[14] D. Seyringer, M. Sagmeister, A. Maese‐Novo, M. Eggeling, E. Rank, P. Muellner, R. Hainberger, W. Drexler, M. Vlaskovic, H. Zimmermann, G. Meinhardt, and J. Kraft, “Technological verification of size‐optimized 160‐channel silicon nitride‐based AWG-spectrometer for medical applications,” *Applied Physics B*, vol. 125, no. 6, pp. 88, Jun. 2019.

[15] T. Hall, M. Hasan, M. Rad, and D. Patrick, “Optical performance monitor,” U.S. patent application 62/868,450, Jun. 28, 2019.

[16] B. E. Little, T. Murphy, ‘Design rules for maximally flat wavelength-insensitive optical power dividers using Mach–Zehnder structures’, *IEEE Photon. Techn. Lett*., vol. 9, no. 12, 1607-1609, 1997.

[17] Abu Naim R. Ahmed, Shouyuan Shi, Mathew Zablocki, Peng Yao, and Dennis W. Prather, "Tunable hybrid silicon nitride and thin-film lithium niobate electro-optic microresonator," *Opt. Lett*., vol. 44, no. 3, 618-621, 2019.

[18] Warren Jin, Ronald G. Polcawich, Paul A. Morton, and John E. Bowers, "Piezoelectrically tuned silicon nitride ring resonator," Opt. Express, vol. 26, no. 3, 3174-3187 (2018).

[19] H. Yamazaki, T. Saida, T. Goh, S. Mino, M. Nagatani, H. Nosaka, and K. Murata, “Dual-carrier dual-polarization IQ modulator using a complementary frequency shifter,” *IEEE J. Selec. Topics Quantum Electron*., vol.19, no. 6, pp. 172-182, May 2013.

[20] E. Kleijn, E. M. van Vliet, D. Pustakhod, M. K. Smit and X. J. M. Leijtens, "Amplitude and Phase Error Correction Algorithm for 3X3 MMI Based Mach–Zehnder Interferometers," *Journal of Lightwave Technology*, vol. 33, no. 11, pp. 2233-2239, June 2015.

Circuit design and integration feasibility of a high-resolution broadband on-chip spectral monitor

MEHEDI HASAN,[1,*] MOHAMMAD RAD,[2] PENG LIU,[1] ERIC BERNIER,[2] AND TREVOR HALL,[1]

[1]Photonic Technology Laboratory, Centre for Research in Photonics, Advanced Research Complex, University of Ottawa, 25 Templeton Street, Ottawa, K1N 6N5, ON, Canada
[2]Huawei Technologies Canada, 303 Terry Fox Drive, Kanata, K2K 3J1, ON, Canada

Abstract: Up-to-date network telemetry is the key enabler for resource optimization by means of capacity scaling, fault recovery, network reconfiguration etc. Reliable optical performance monitoring in general and specifically the monitoring of the spectral profile of WDM signals in fixed and flex-grid architecture across the entire C-band remains challenging. This article describes a spectrometer circuit architecture along with an original data processing algorithm that combined can measure the spectrum quantitatively across the entire C-band aiming at < 1 GHz resolution bandwidth. The circuit is composed of a scanning ring resonator followed by a parallel arrangement of AWGs with interlaced channel spectra. The comb of ring resonances provides the high resolution and the algorithm creates a virtual tuneable AWG that isolates individual resonances of the comb within the flat passband of its flat synthesised channels. The parallel arrangement of AWGs may be replaced by a time multiplexed multi-input port AWG. A simulation verification of the circuit using components designed for fabrication is presented. The architecture is robust to fabrication process variations owing to its data processing approach. Due to its maturity and low loss, CMOS compatible Si_3N_4 is chosen for integration.

1. Introduction

In an optical network, optical performance monitoring (OPM) is the key enabling technology for reliable spectrum management. Up-to-date network telemetry is required for capacity scaling, network or component fault recovery, and network reconfiguration through performance prediction and planning. The monitoring includes information on bit-error-rate (BER), optical signal-to-noise ratio (OSNR), electrical signal-to-noise ratio (ESNR), loss, power, etc. The monitoring information is then fed to the network management agent for resource optimization to maximize the reach versus rate. In practice, optical performance monitoring may be based on the measurement of one or several parameters. However, OPM is used herein to refer to "power" monitoring since power is one of the key indicators of performance in optical systems.

In transport optics, especially in WDM networks, spectral sensing is not straightforward. Traditionally WDM channels are distributed over the 40 nm wide fibre-optic C-band (1530 nm to 1570 nm) with fixed centre frequencies arranged on the ITU grid at intervals of 50 GHz or 100 GHz. and an OPM card is used to measure the power. The working principle of the OPM card involves sweeping a tunable filter with 50 GHz resolution over the spectrum to make available ITU grid channel power readings. Due to their excessive power consumption, size and cost, OPM cards are deployed only at a few points in the network; typically co-located with reconfigurable add-drop multiplexers (ROADMs). However, current optical networks are elastic in nature, i.e. the channels are not located on a fixed regular grid, rather the channel center wavelength can be placed at an arbitrary location within the spectrum. The flexible grid can support a variety of channel power profiles (i.e., bandwidth and power spectral density) with a resolution of channel centre frequency placement as fine as 6.25 GHz. Flex-ready spectrum measurements are required to facilitate the deployment of the flex-grid system. As a result, flex-grid ready ROADM architectures are equipped with new modules that can measure power at desired frequency location and resolution. However, due to cost issues, spectrum measurement is only performed at add-drop nodes and not at amplifier nodes. Moreover, a single OPM module is shared by the multi degree-ROADM so the OPM measurement speed reduces as the number of lines it supports increases. Consequently, the performance of WDM channels in a section (ROADM-to-ROADM) is modeled based on an analytical or a semi-analytical analysis or a machine learning approach. The absence of OPM makes it difficult to have live and accurate network measurement; and hence hard to implement performance optimization. Complete knowledge of spectral content in a network is prerequisite for the effective use of color-, direction-, contention-, grid-, filter-, gap-less ROADM, flexible modulation formats, flexible channels frequencies and spectral assignment.

A variety of different approaches to the problem of spectral sensing with high resolution across a wide band have been disclosed in the literature [1-9] but when scaled to combine acceptable resolution with wideband operation their practical implementation is most often not feasible due to excessive cost, loss and footprint. An integrated solution

for a high resolution (sub-GHz) spectrometer to monitor the power in fixed and flex grid across the entire C band 1530 nm to 1565 nm remains challenging. Nevertheless, a three-stage architecture proposed in a previous publication [10] has been shown to be viable. The first stage is a tunable ring resonator (RR) that defines the resolution. The third stage is an arrayed waveguide grating (AWG) that isolates one RR resonance within each of its channels. The principal innovation is ganged tuning of the RR and AWG to retain the RR resonance at the center of the AWG channel passband. This is achieved by a second stage that uses an MZI to form a coherent superposition of two interleaved AWG channel spectra corresponding to a pair of input ports. Further details can be found in [10]. This paper describes a refinement of the architecture and method that enables the ganged tuning of the AWG to be virtualized. The coherent superposition of a pair of AWG input channels is replaced by the incoherent superposition of pairs of AWG outputs, which may be performed by processing the measured AWG channel powers. The MZI stage is eliminated, releasing the spectrometer from any requirement to control inter-stage optical path lengths and thereby significantly easing manufacture.

In this paper, the circuit architecture design, modelling and integration feasibility of an ultra high-resolution wideband spectrometer based on the refined architecture is presented. The purpose of the proposed circuit is to measure the spectral profile of WDM channels in flex- and fixed-grid architectures across 1530 nm to 1565 nm (C band). The architecture combines a RR and a number M of AWG with interleaved channel spectra. For the purpose of exposition, the $M = 2$ case is first considered but subsequently generalised. Hardware economies may be made by replacing the multiple AWGs by a single time multiplexed M-input AWG. The $M = 3$ architecture has particular merit as the first to offer essentially zero crosstalk. The proposed spectrometer can be fabricated in any mature fabrication platform. However, the resolution bandwidth of the spectrometer primarily depends on the insertion loss (dB/turn) of the RR. Hence in order to meet the specification of the proposed spectrometer, the CMOS compatible Si_3N_4 photonic integration platform has been selected as it offers low loss, tight confinement, low dispersion and a mature thermo-optic phase shifter technology. There are ample reports in the literature of the technological verification of spot size convertors (SSC), multimode interference couplers (MMI), tunable RR, and sub-circuits such as Mach-Zehnder interferometers (MZI) [11-13] and high port count AWG [14] fabricated using the Si_3N_4 integration platform. The detail simulation verification of the proposed architecture is presented using components (RR and AWG) designed for fabrication. A combination of industry standard software tools is used for the component design. A simple but novel signal processing approach enables the spectrometer to scan the entire C-band with high resolution (~1GHz) using only one dynamic control. The original signal processing method renders the proposed architecture robust to fabrication tolerances.

Proposed spectrometer circuit architecture

The schematic diagram of the proposed circuit architecture is shown in Fig. 1(a). The architecture consists of two stages; the first stage is the RR which offers the fine filtering while the last stage AWG offers the coarse filtering. In other words, the RR generates a periodic train of fine resonances spaced by its free spectral range (FSR), while the AWG isolates one RR resonance in each output channel. Hence, the output channel frequency spacing of the AWG must be equal with the FSR of the RR by design. The RR defines the spectrometer resolution bandwidth and is tunable in frequency over one FSR. Two identical AWGs with -3 dB channel passband-width close to half the output channel frequency spacing are required for the proposed circuit architecture implementation. However, the two AWGs are not driven by the same input channel (port), rather they are driven by adjacent input ports as shown in Fig. 1(a). The input channel frequency spacing is equal to half of the output channel frequency spacing (i.e. $1/2$ FSR). The channel spectra of AWG_1 and AWG_2 are thereby interlaced and overlap as illustrated in Fig.1(b) for a 50 GHz channel frequency spacing. For clarity, three only of the channel spectra of each AWG are shown with possible mappings of the comb of RR resonances. In practice, 50 GHz AWGs need 88 channels to cover the whole C-band. The comb of RR resonances is tuned by an intra-ring phase shift θ. The translation in frequency of the comb is proportional to the phase shift and ranges over one FSR as θ ranges over 2π radians. For simplicity of exposition, $\theta = 0$ is taken to correspond to the alignment of the RR resonances with AWG_1 channel passband centre frequencies. It follows that $\theta = \pi$ corresponds to the alignment of the RR resonances with AWG_2 channel passband centre frequencies and $\theta = \pi/2, 3\pi/2$ corresponds to alignment respectively with the intersection between the upper (lower) AWG_1 -3dB channel passband edge and the lower (upper) AWG_2 -3dB channel passband edge.

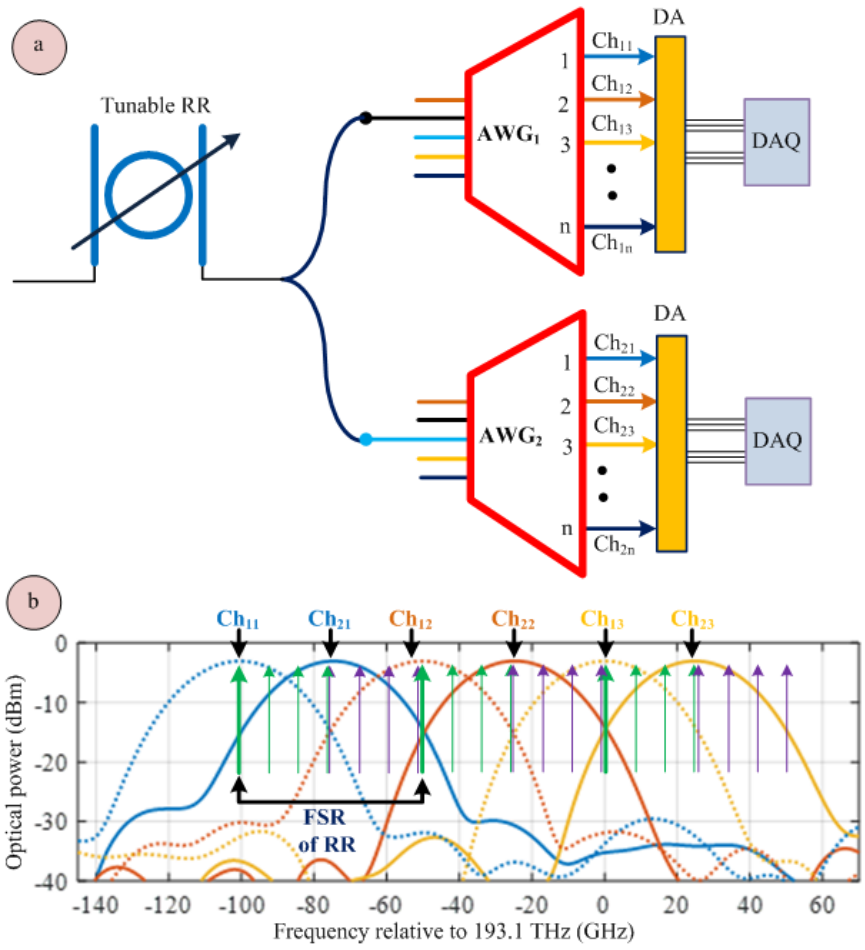

Fig. 1. (a) Schematic of the proposed spectrometer; (b) interlaced optical spectrum of AWG_1 and AWG_2 with the resonance mapping over one FSR. AWG, arrayed waveguide grating; RR, ring resonator; DA, detector array; DAQ, data acquisition Ch; channel; FSR, free spectral range.

The optical power of each output channel of both AWGs is measured by a photodetector array while the RR is scanned over an FSR under the control of the data acquisition system (DAQ). The principal novelty of the spectrometer is the construction of a virtual AWG that is tuned to retain the ring resonance within the passband of its synthesised channels A virtual channel with index m is synthesised by summing the optical power of a selected pair of interlaced AWG_1 and AWG_2 channels in two phases:

Phase 1: As the ring resonance is tuned over the first half of the FSR by a tuning phase shift from $\theta = 0$ to $\theta = \pi$ (green stem in Fig. 1(b)), AWG_1 channel m (Ch_{1m}) and AWG_2 channel m (Ch_{2m}) are summed.

Phase 2: As the ring resonance is tuned over the second half of the FSR by a tuning phase shift from $\theta = \pi$ to $\theta = 2\pi$ (purple stem in Fig. 1(b)), AWG_2 channel m (Ch_{2m}) and AWG_1 channel $m + 1$ ($Ch_{2(m+1)}$) are summed.

If the AWG channels have a raised cosine spectral profile, then the synthesised channels have a perfectly flat passband. In practice the AWG channel profile will differ from the ideal and there will be ripple. However, the ripple will be small as the synthesised channel spectral profile will agree with the ideal when the ring resonance is aligned at either passband centre or at the intersection of the -3dB passband edges of the AWG channels summed. Table 1 tabulates the steps of the data processing algorithm performed in the electronic domain by the data acquisition system. Handover from phase 1 of the processing algorithm to phase 2 occurs at $\theta = 180^{\circ}$ but this is not critical. Handover may occur for θ anywhere between 165° or 195° with very little or no penalty. Hence, the careful tracking of the position of a resonance is not mandatory. However, an integrated wave meter concept presented in [16] can be used to monitor the position of the RR resonance within a single channel of the AWG. Since the resonances are substantially periodic in

frequency, albeit very slightly detuned by chromatic dispersion, the position of the resonance within each channel of the AWG can be mapped easily.

Table 1. Data processing algorithm for a 2 AWG architecture

RR tuning phase	Synthesized channel	Remarks
$\theta \in [0, \pi]$ (1^{st} half FSR)	$\mathrm{Ch}_{11} + \mathrm{Ch}_{21}$ ⋮ $\mathrm{Ch}_{1n} + \mathrm{Ch}_{2n}$	green stem Fig. 1(b)
$\theta \in [\pi, 2\pi]$ (2^{nd} half FSR)	$\mathrm{Ch}_{21} + \mathrm{Ch}_{12}$ ⋮ $\mathrm{Ch}_{2(n-1)} + \mathrm{Ch}_{1n}$	purple stem Fig. 1(b)

The spectrometer requires only one control, which sets the intra-ring phase shift in order to tune the RR resonant frequency comb cyclically over one FSR. Our device and circuit simulations; previously reported experimental demonstrations; and the process development kit support the practicality of a 50 GHz FSR RR. Table 2 shows the detail specifications of the proposed circuit design. For a RR FSR of 50 GHz, the required number of AWG output ports is 88 to cover the entire C-band. The number of output ports can be reduced by increasing the FSR of the RR, since 50→150 GHz channel spacing AWG having output ports up to 96 are available commercially [15]. On the other hand, a RR having FSR of 220 GHz fabricated using double strip TrIPleX^{TM} waveguide technology is already reported in [3].

Table 2. Detail design specifications of the proposed circuit architecture shown in Fig. 1(a)

Design specifications	Numbers	Remarks
RR free spectral range (GHz)	50	
AWG output channel spacing (GHz)	50	equal to the free spectral range of RR
AWG output channel bandwidth (GHz)	20	$\sim \leq 1/2$ AWG output channel spacing
AWG input channel spacing (GHz)	25	half of AWG output channel spacing
Number of AWG output channel	88	
Total spectrum covered (THz)	4.4	$88 \times 50 = 4400$ GHz (entire C band)

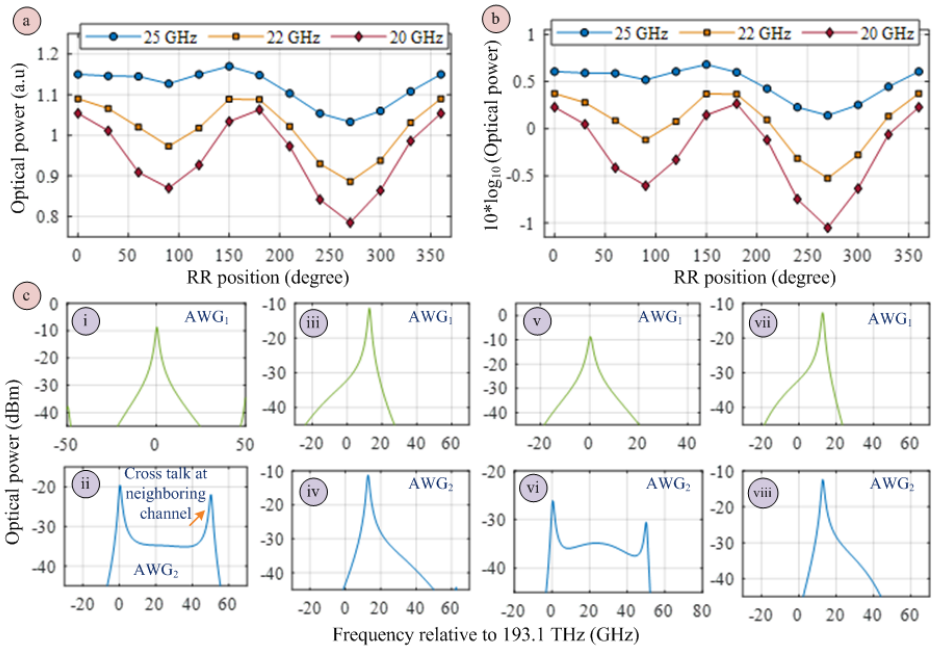

Fig. 2. Simulated optical power as a function of ring resonance for different passband width of the AWG channel, (a) linear scale, (b) logarithmic; (c) optical spectrum of AWG_1 and AWG_2 at channel one for ring resonance position of 0˚ and 90˚ for the passband width of 25 GHz [i-iv] and 20 GHz [v-viii] respectively.

The VPIphotonics simulation tool is used to evaluate the performance of the combined circuit architecture and data processing method. The optical power at each output channel of the both AWGs is monitored while scanning the RR over one FSR. The shape of the AWG is defined by VPIphotonics physical model. The calculation of the power depends on the number of samples used in the simulation time window. Since the signals were widely spread, a moderate time window is used in the simulation to avoid an excessive memory requirement. A slight variation in the result is obtained for different time window settings. The simulated output is then processed using the algorithm presented in Table 1. Figure 2 shows the variation in measured optical power as a function of the resonance position over one FSR for various AWG channel passband widths. Channel 1 & 2 of AWG_1 and channel 1 of AWG_2 are used for the calculation. The results show that the spectral measurement is almost flat with little ripple (~0.5 dB) over the entire FSR for a passband width of 25 GHz. The dependence on the simulation parameters suggest that the magnitude

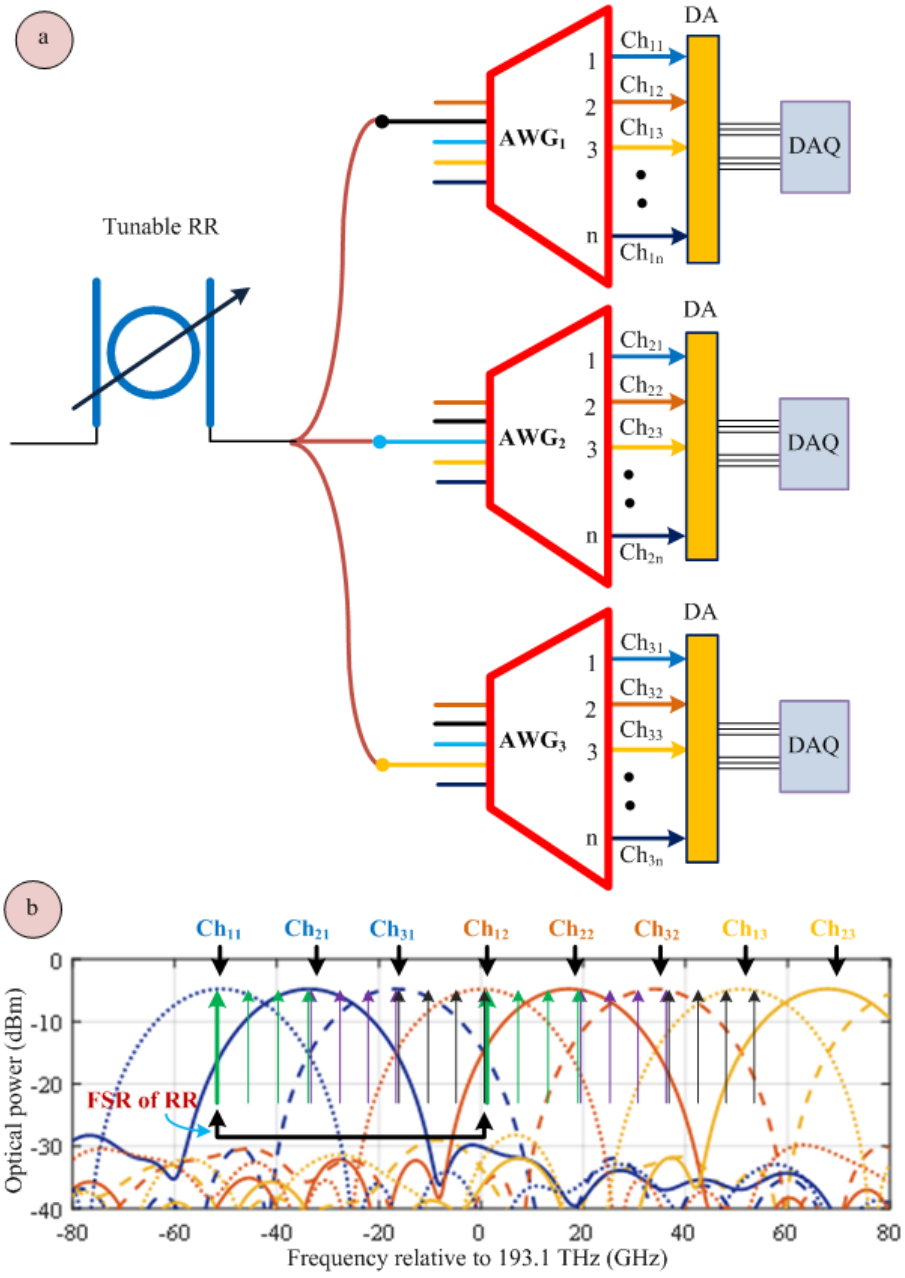

Fig. 3. (a) Schematic of the modified design; (b) interlaced spectrum of AWG_1, AWG_2 and AWG_3 with the resonance mapping over one FSR.

of the ripple is an over estimate and the asymmetry is an artifact. The ripple increases inversely with the AWG passband and reaches ~1.25 dB for a passband width of 20 GHz. Figure 2(c[i-iv]) shows the optical spectrum of AWG_1 and AWG_2 at output channel one (Ch_{11} & Ch_{21}) for ring resonance position of 0˚ and 90˚ respectively for passband

width of 25 GHz. It shows that a strong cross talk component is present at the AWG_2 channel. Hence, the power calculation is misleading at the 0˚ position. The crosstalk component can be reduced by reducing the passband width of the AWG. Figure 2(c[v-viii]) shows the optical spectrum of AWG_1 and AWG_2 at the same resonance position for the pass band width of 20 GHz. The cross talk at the neighboring channel is reduced by ~-6 dB. This leads to a ripple of ~1→1.25 dB over the entire FSR. Since the transmission characteristic of an AWG is substantially periodic, the simulated result will almost be same for any other channel measurement of the AWG. The entire channel spectra of both AWGs are presented in Fig. 8.

To substantially eliminate adjacent channel crosstalk and to reduce the ripple, the architecture is upgraded to three AWG with interlaced channels as shown in Fig. 3(a). For simplicity, assume the three AWGs are identical with input port spacing of $1/3$ of the output channel spacing, with AWG_1, AWG_2 and AWG_3 driven by input port l, $(l+1)$ and $(l+2)$ respectively; where l is an integer. Figure 3(b) shows the interlaced spectrum of the upgraded architecture using the parameters given in Table 3.

Table 3. Detail design specifications of the proposed circuit architecture shown in Fig. 3(a).

Design specifications	Comments	Remarks
RR free spectral range (GHz)	51	
AWG output channel spacing (GHz)	51	equal to the free spectral range of RR
AWG output channel bandwidth (GHz)	16	$\sim \leq 1/3$ AWG output channel spacing
AWG input channel spacing (GHz)	17	half of AWG output channel spacing
Number of AWG output channel	88	
Total spectrum covered (THz)	4.4	$88 \times 51 = 4488$ GHz (entire C band)

A virtual channel with index m is synthesised by summing the optical power of a selected pair of interlaced AWG_1, AWG_2, AWG_3 channels as before but now in three phases:

Phase 1: As the ring resonance is tuned over the first third of the FSR by a tuning phase shift from $\theta = 0$ to $\theta = 2\pi/3$ (green stem in Fig. 3(b)), AWG_1 channel m (Ch_{1m}) and AWG_2 channel m (Ch_{2m}) are summed.

Phase 2: As the ring resonance is tuned over the second third of the FSR by a tuning phase shift from $2\pi/3$ to $\theta = 4\pi/3$ (purple stem in Fig. 3(b)), AWG_2 channel m (Ch_{2m}) and AWG_3 channel m (Ch_{3m}) are summed.

Phase 3: As the ring resonance is tuned over the final third of the FSR by a tuning phase shift from $\theta = 4\pi/3$ to $\theta = 2\pi$ (black stem in Fig. 3(b)), AWG_3 channel m (Ch_{2m}) and AWG_1 channel $m+1$ ($Ch_{1(m+1)}$) are summed.

Table 4. Data processing algorithm for a 3 AWG architecture

RR tuning phase	Synthesized channels	Remarks
$\theta \in [0, 2\pi/3]$ (1st third FSR)	$\mathrm{Ch}_{11} + \mathrm{Ch}_{21}$ ⋮ $\mathrm{Ch}_{1n} + \mathrm{Ch}_{2n}$	green stem Fig. 3(b)
$\theta \in [2\pi/3, 4\pi/3]$ (2nd third FSR)	$\mathrm{Ch}_{21} + \mathrm{Ch}_{31}$ ⋮ $\mathrm{Ch}_{2n} + \mathrm{Ch}_{3n}$	purple stem Fig. 3(b)
$\theta \in [4\pi/3, 2\pi]$ (3nd third FSR)	$\mathrm{Ch}_{31} + \mathrm{Ch}_{12}$ ⋮ $\mathrm{Ch}_{3(n-1)} + \mathrm{Ch}_{1n}$	black stem Fig. 3(b)

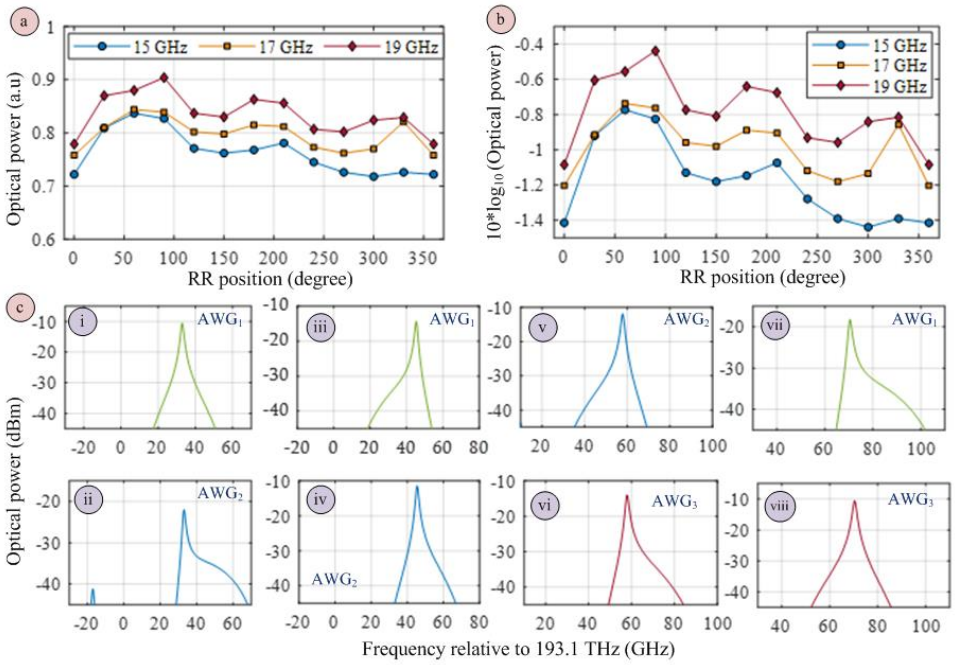

Fig 4. Simulated optical power as a function of ring resonance for different passband width of the AWG channel (a) linear scale (b) logarithmic scale; (c) optical spectrum of AWG_1, AWG_2 and AWG_3 for ring resonance position of 0˚[i-ii], 90˚[ii-iv], 180˚ [v-vi] and 270˚[vii-viii] for the passband width of 17 GHz.

Table 4 tabulates the steps of the data processing algorithm performed in the electronic domain by the data acquisition system. Figure 4 shows the variation in measured optical power as a function of the resonance position over one FSR for three AWG channel passband widths. The ripple in the spectrum sensing is reduced to $\leq$ 0.4 dB for the preferred passband width $1/3$ (17 GHz) of the output channel spacing (51 GHz). Due to fabrication tolerances, the passband width may vary from 17 GHz, as such two other measurements are taken for width of 15 GHz and 19 GHz respectively. Almost identical results are obtained. Ideally, the measured optical power should be constant as there is negligible crosstalk present in the design. The variation is obtained in the simulation due to the time window settings; can be considered as an artifact. Fig. 4(c[i-viii]) shows the optical spectrum at different location of the ring resonance.
There is no crosstalk present in the spectrum and the spectral sensing is very simple and straight forward. Fig. 4(c[i-iv]) shows the spectrum of AWG_1 and AWG_2 for resonance position $\leq$120˚. Figure 4(c[v-vi]) shows the spectrum of AWG_2 and AWG_3 obtained at resonance position 180˚. Finally, Fig. 4(c[vii-viii]) depicts the optical spectrum of AWG_3 and AWG_1 measured at the resonance position of 270˚. Since the overall spectrum is delivered to all the three AWG but the measurement involves summing the outputs of only two AWG, $1/3$ of the total input power is discarded. Furthermore, it requires one more AWG over the scheme presented in Fig. 1(a). The huge advantage of the design is spectral sensing is performed with essentially no adjacent channel crosstalk.

The practical implementation can be made simpler by time multiplexing using a single 3-input AWG and a 1×3 switch as shown in Fig. 5. The input ports are spaced in frequency by $1/3$ of the AWG output frequency spacing. For simplicity, assume the resonance position is at 0˚. The switch is connected to the upper input port of the AWG. The output data is recorded by the DAQ. Now change the switch to the middle input and record the data. Repeat the procedure for resonance position up to 120˚. Alternatively; keeping the switch at upper input port, scan the ring resonance up to 120˚ and record the data. Now change the switch to middle input port, scan the ring resonance from 0˚→120˚ and record data. Now data processing will be done as per Table 4. For resonance position 120˚→240˚, the switch will be toggled between the middle input and last input port of the AWG. Finally, for 240˚→360˚, the switch will toggle between 1st input and third input port of the AWG. As before there is very little penalty in the measured optical power if handover between phases occurs within $\pm$20˚ of the specified tuning phases of 120˚, 240˚, 360˚. The switch does not need to toggle at the exact positions specified and the data acquisition can be performed flexibly.

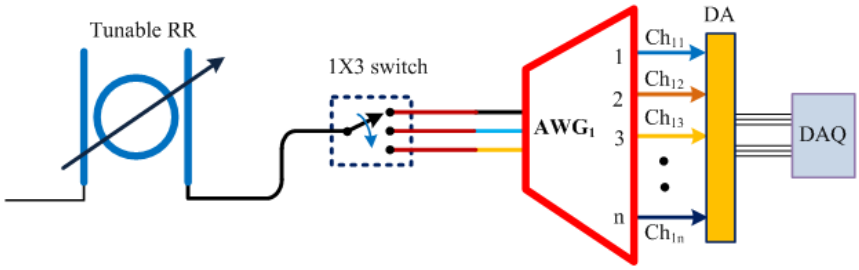

Fig. 5. Schematic diagram showiung practical implementation.

Validation & integration feasibility

A combination software simulation tools are used to validate the concept. For example, VPIphotonics is used for the circuit simulation whereas, Photon Design and OptiBPM is used to verify the function of each component that comprise the architecture. The proposed spectrometer can be fabricated in any mature low-loss photonic integration platform. If the excess loss of the ring per turn is negligible in comparison to the power coupled out per turn, the resolution bandwidth of the spectrometer is determined by the power cross-coupling ratio of the couplers. The ring excess loss per turn consequently limits the achievable resolution. An integration platform supporting the design of low-loss waveguides and low-loss waveguide bends is therefore paramount. Owing to its low loss, tight confinement, low dispersion waveguides and a mature thermo-optic phase shifter technology, the CMOS compatible Si_3N_4 photonic integration platform is selected to meet the specification of the proposed spectrometer circuit. The platform also offers good prospects for further loss-reduction [17] and to lower power consumption, temperature insensitive, alternatives to thermo-optic phase-shift elements [18-19]. For effective use of resources, the original plan for fabrication envisaged

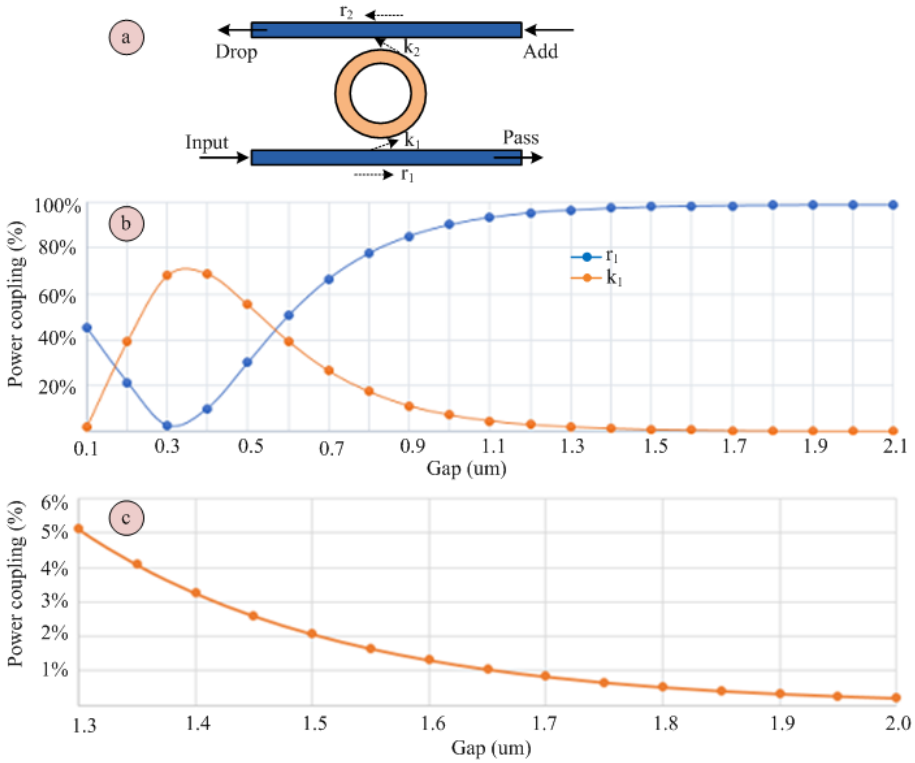

Fig. 6. (a) Schematic diagram of a RR; (b) power coupling between the ports of a directional coupler as a function of spatial separation among them; (c) zoom-in view of the power coupling at the cross port as a function of spatial separation.

access to multi-project wafer MPW runs for test structures followed by a custom wafer run for fabrication of prototypes for demonstration. LioniX only offer Si_3N_4 Triplex technology MPW runs for designs using the asymmetric double strip (ADS) waveguide and the low-cost photolithography used has a minimum feature size of 1 μm. Accordingly, the simulations of the components and sub-circuits that constitute the proposed spectrometer are designed using ADS as reference waveguide. The waveguide characteristic over full C-band is obtained by using the Photon design software tool FIMMWAVE. TE-like mode is used in all the simulation due to its tight confinement, hence it exhibits lower bend loss in comparison to the TM-like mode. The effective group index of the mode at the at the smaller wavelength edge (1530 nm), centre wavelength (1545 nm), and the longer wavelength edge (1565 nm) of the C-band is found to be 1.7725, 1.76841 and 1.7629 respectively.

Figure 6(a) shows the schematic diagram of a RR. As shown, it requires two directional couplers (DC). The resolution of the spectrometer is largely set by DC power cross coupling and is determined by the spatial gap between the interacting waveguides. A variety of numerical and quasi analytical methods involving different approximations are used to bracket a range of gaps targeting 2-4% power coupling. The range of gaps is then sampled by test structures to enable the gap to be refined experimentally. For example, Figure 6(b) shows of one full scanning by OptiBPM of power coupling as a function of the gap. The zoom in view of the power coupling at the cross port of the DC is shown in Fig. 6(c). Simulation result show that, for a gap of 1.3 um the power coupling at the cross port is 5% and it reduces to $<\sim$1% for a gap of 1.7 um. For the MPW run, several ring resonators are laid out on the mask having gaps from 1.3 um to 1.8 um with 0.1 um increment with the objective that at least one RR works well. Two identical DC are used in the ring design.

VPIphotonics software simulation is used to simulate the ring response for different power coupling ratios. The DC is designed first using FIMMWAVE software tool. Then the s-matrix as a function of entire C-band is imported to VPIphotonics. Accordingly, the DCs are configured in VPI to have same characteristics as found using the FIMMWAVE tool. The power splitting ratio of 94.92% and 3.98% at the design wavelength $1545\ nm$ is used in the simulation verification. The excess loss of the DC is found to be 1.1%.

The ADS waveguide ring circumference is calculated to be $3.3928\ mm$ at 1545 nm for an FSR of 50 GHz using the following formula.

$$FSR(\omega) = c/n_g(\omega)l \tag{1}$$

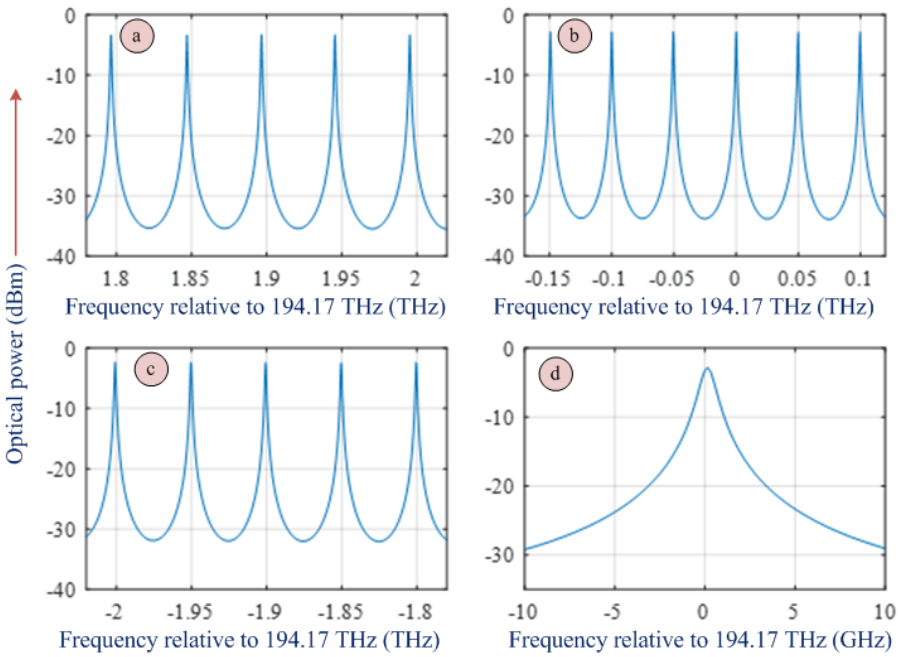

Fig. 7. Simulated transmission spectrum of the RR; (a) smaller wavelength edge; (b) center wavelength; (c) longer wavelength edge; and (d) zoom-in view of the ring resonance at the design wavelength. Waveguide loss is 0.4 dB/cm, the cross coupling is 3.98% with coupler access loss of 1.1%. The simulated full width half maximum (FWHM) is $\leq$ 1 GHz. The insertion loss of the RR is found to be ~3.2 dB.

where, n_g is the group index, l is the length of the delay line to obtain the specified FSR. The corresponding ring radius is 539.99 μm. The bend loss of an ADS waveguide bend of this radius of curvature is negligible over the C-band; the mode is fully bound by the waveguide bend and the only terms contributing loss are absorption and scattering loss. Detailed data on absorption and scattering loss is not available beyond the disclosure that the total waveguide loss is circa 0.1-0.2 dB cm^{-1} for a ring of 50-100 um radii. The waveguide loss is considered as 0.4 dB/cm in the simulation as a conservative assumption.

Table 5. Design specifications detail of the AWG_1 and AWG_2.

Design specifications	Comments	Remarks
AWG output channel spacing (GHz)	50	equal to the free spectral range of RR
AWG output channel bandwidth (GHz)	20	$\sim \leq 1/2$ AWG output channel spacing
AWG input channel spacing (GHz)	25	half of AWG output channel spacing
Number of input channel	8	
Number of output channel	32	
Free spectral range FSR (GHz)	1600	32×50 GHz

Figure 7 (a-c) shows the simulated transmission spectra of the RR at various point of the C-band. The peak transmission of the RR varies 1→ 1.25 dB from the longer wavelength edge to the shorter wavelength edge of the C-band. Furthermore, the FSR is slightly less than 50 GHz at the edge of the short wavelength due to variation of the effective index across the band from the index at the design wavelength, 1545 nm. This is due to the presence of group velocity dispersion. To minimise the relative detuning between the RR and AWG, the AWG channel passband center frequencies can be offset slightly. Further, digital signal processing can be used to provide the quantitative spectrum. Fig. 7(d) shows the zoom-in view of the ring resonance at the design wavelength. The full width half maximum (FWHM) bandwidth of the RR is found to be around 1 GHz. The insertion loss of the simulated ring resonator is found to be 3.2 dB at the worst cases. The LioniX MPW fabrication process offers only thermo-optic phase shifts. Hence,

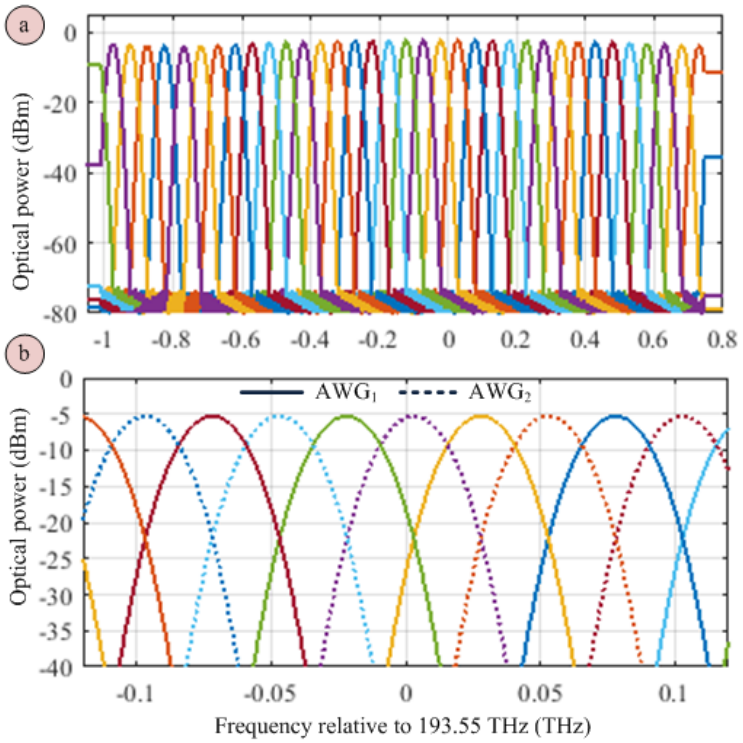

Fig. 8. (a) Simulated spectrum of the AWG_1 with input light launch from upper left port (port 1); (b) zoom-in view of the interlaced spectrum between AWG_1 and AWG_2. The input light is launched from the identical input port (port 1).

the RR will be tuned using such a phase shifter. The precision of the RR tuning over one FSR depends on the applied voltage to the phase shifter. The tuning can be done through a high bit number digital to analog (DAC) converter having moderate sample rate (~256 kbps). However, due to low drive voltage, low drive power and linear voltage to index relationship, electro-optic tuning offers smooth operation with better efficiencies [20]. As an alternative means of tuning, the insertion of piezo-electric actuator augurs well for the future [19].

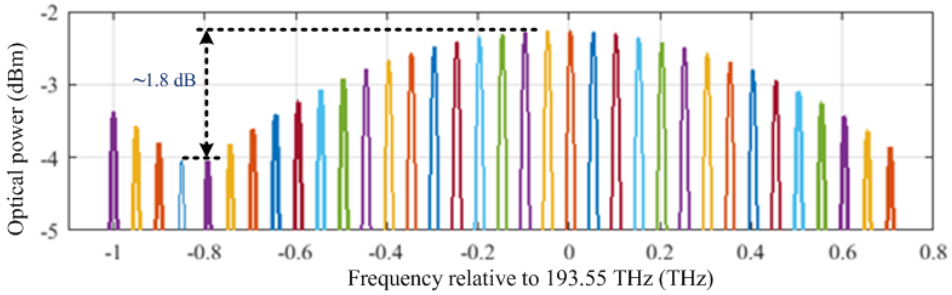

Fig. 9. Transmission spectra of the AWG output-channels. Zoom-out view of Fig. 8(a).

While the fine tuning of the RR is performed, the AWGs perform the coarse filtering, that is isolating each resonance of the RR at the output ports of the AWGs. The AWG design is by Bright Photonics BV to the specification given in Table 5. Two identical AWGs except for a channel spectrum shifted by 25 GHz have been laid on the mask. Figure 8(a) shows the designed transmission spectra of the upper AWG as a function of frequency. As shown in the table, a 32-channel cyclic AWG is designed for fabrication. Two AWGs (AWG_1 & AWG_2) are identical in design apart from a 25 GHz relative shift of the channel spectra. Figure 8(b) shows a zoomed-in view of the interlaced AWG_1 and AWG_2 channel spectra when light is launched from the input channel one. It also shows that the crossover between the channels are down to ~-22 dB, this was the main aim of the reduction of the passband width to 20 GHz. Similar results were obtained when light is launched from other input ports. For a ring resonator having FSR of 50 GHz, an AWG of 86~88 channels are required to cover the whole spectrum. The 32- channel AWG design presented here can easily be scaled up to 86 or 88 channels since a higher number (96) of output channels commercial AWG is already available [15]. Since the designed 32-channel AWG is cyclic, the output spectrum is periodic with a period of 32. Hence, with the aid of a tunable optical bandpass filter the spectrum of the whole C-band can be measured to prove the concept. Figure 9 shows the zoom-out spectra of the designed AWG. It shows that the envelop of the AWG passband is ~1.8 dB down at the edges of the AWG FSR compared to the center of the AWG FSR. This can be reduced significantly by increasing the FSR of the AWG.

The circuit level simulation has been implemented using VPIphotonics to evaluate the overall performance. The RR is configured as explained in Fig.7. The S matrix of the AWGs provided by Bright Photonics BV is imported into VPIphotonics accordingly. The scanning is performed by changing the position of the ring resonance across one FSR while recording the available optical power at the PIN diode at the output of each AWG channel. The arithmetic summation is performed offline as per Table 1 to obtain the plot as shown in Fig.10 (a-b) and 11 (a-b). The results presented in Fig. 10 are obtained when both the AWGs are driven from input channel one (1). Whereas, Fig. 11 is obtained by launching the light from input channel four (4). Both the figures are almost identical. Fig. 10 (a-b) shows the available optical power at the PIN photodiode over one complete FSR. Figure 10 (a) represents the optical power variation as a function of frequency on a linear scale, whereas Fig. 10 (b) uses a semi log scale. The optical power variation is plotted on a logarithmic scale. The measured power at the edges of the FSR is ~1.5→2 dB less than the power at the center of the FSR. This finding is consistent with the envelop of the AWG passband reported in Fig. 9. The inset shows a zoomed-in view of the plot at three different resonance locations within the FSR. It shows that a ripple of ~1→1.25 dB is present in the detected power; this is identical with the findings presented in Fig. 2(b) obtained by simulation for the ideal case. Figure 10 (c) shows the optical spectrum obtained from two different channel located at the edges (left and right) of the AWG FSR for two different position of the RR. The spectrum presented in the upper row is obtained at the output channel of AWG_1 while the spectrum in the lower row is obtained from AWG_2. Figure 10 (c) (i,-iv) is obtained for the RR position of 0˚. The position 0˚ refers to the alignment of the ring resonances with the passband centre of the AWG. This is taken as the reference (starting) point to simplify the calculation. Whereas spectrum presented in Figure 10 (c) (v-viii) obtained for ring position of 90˚; slightly to the right of the origin at 0˚. Figure 10 (c) (ii, iv) shows that the crosstalk contribution in the neighbouring channel is reduced greatly by reducing

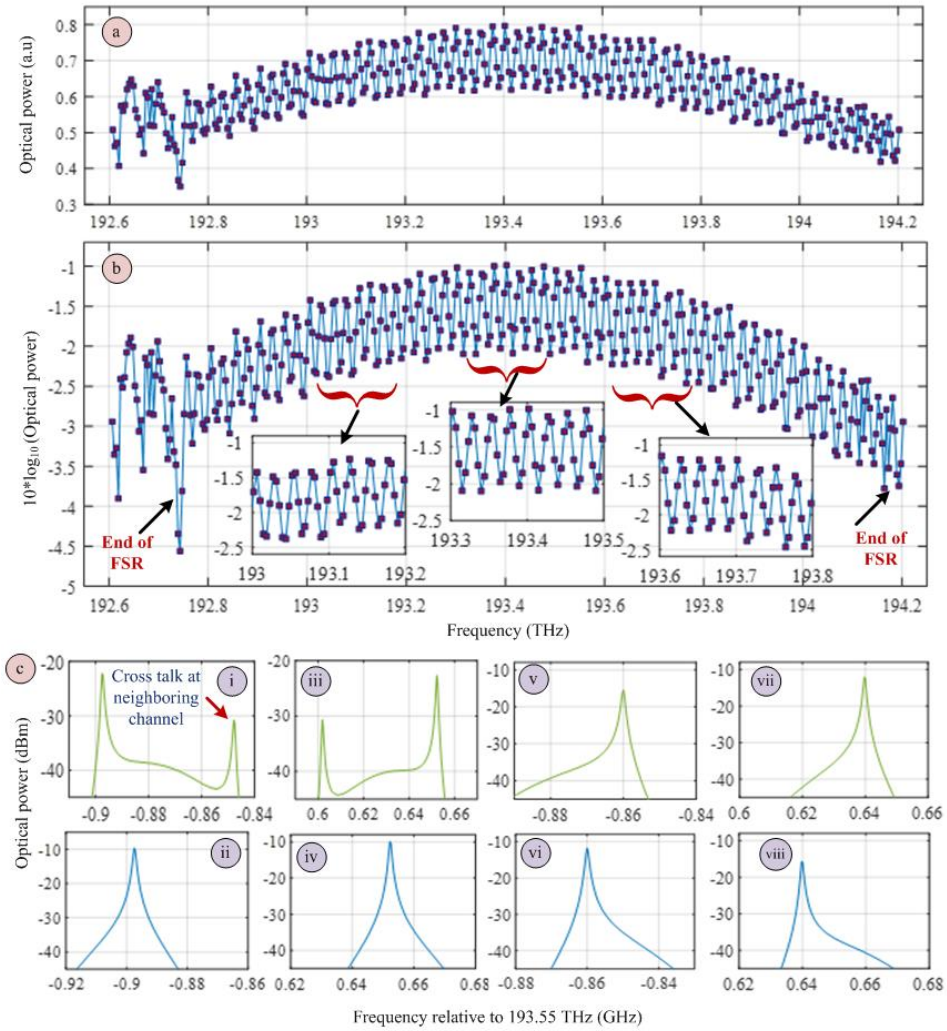

Fig. 10. Simulated result of the whole circuit when light is launched from input channel one (1) of both AWG; (a) optical power available at the PIN photodiode as a function of frequency; (b) logarithmic representation of the optical power measured in (a); (c) optical spectrum at the left (i-ii & v-vi) and right edges channel (iii-iv & vii-viii) of the AWG FSR for 0˚ and 90˚ degree position of the RR respectively. Upper row represents the spectrum of AWG_1 while lower row represents the spectrum of AWG_2. The spectrum sensing is obtained in (a) by simply summing the detectable optical power in AWG_1 and AWG_2. In this case (i)+(ii) for the frequency offset ~-0.89 THz and (iii)+(iv) for frequency offset ~0.65 THz from the center (193.55 THz) of the AWG FSR.

the AWG passband bandwidth to 20 GHz. The simulated crosstalk at the neighbouring channel is less than < -30 dB for the worst cases. Figure 11 is identical to Fig. 10 albeit the light is launched from input channel four (4). In addition, the spectrum presented in Figure 11 (c) (v- viii) is for the RR position of 120˚ rather than for 90˚ in Fig. 10. Figure 10 (c) shows the optical spectrum obtained from two different channel located at the edges (left and right) of the AWG FSR for two different position of the RR. The spectrum presented in the upper row is obtained at the output channel of AWG_1 while the spectrum in the lower row is obtained from AWG_2. Figure 10 (c) (i-iv) is obtained for the RR position of 0˚. The position 0˚ refers to the alignment of the ring resonances with the passband centre of the AWG. This is taken as the reference (starting) point to simplify the calculation. Whereas spectrum presented in Figure 10 (c) (v-viii) obtained for ring position of 90˚; slightly to the right of the origin at 0˚. Figure 10 (c) (ii, iv) shows that the crosstalk contribution in the neighbouring channel is reduced greatly by reducing the AWG passband bandwidth to 20 GHz. The simulated crosstalk at the neighbouring channel is less than < -30 dB for the worst cases. Figure 11 is identical to Fig. 10 albeit the light is launched from input channel four (4). In addition, the spectrum presented in Figure 11 (c) (v- viii) is for the RR position of 120˚ rather than for 90˚ in Fig. 10.

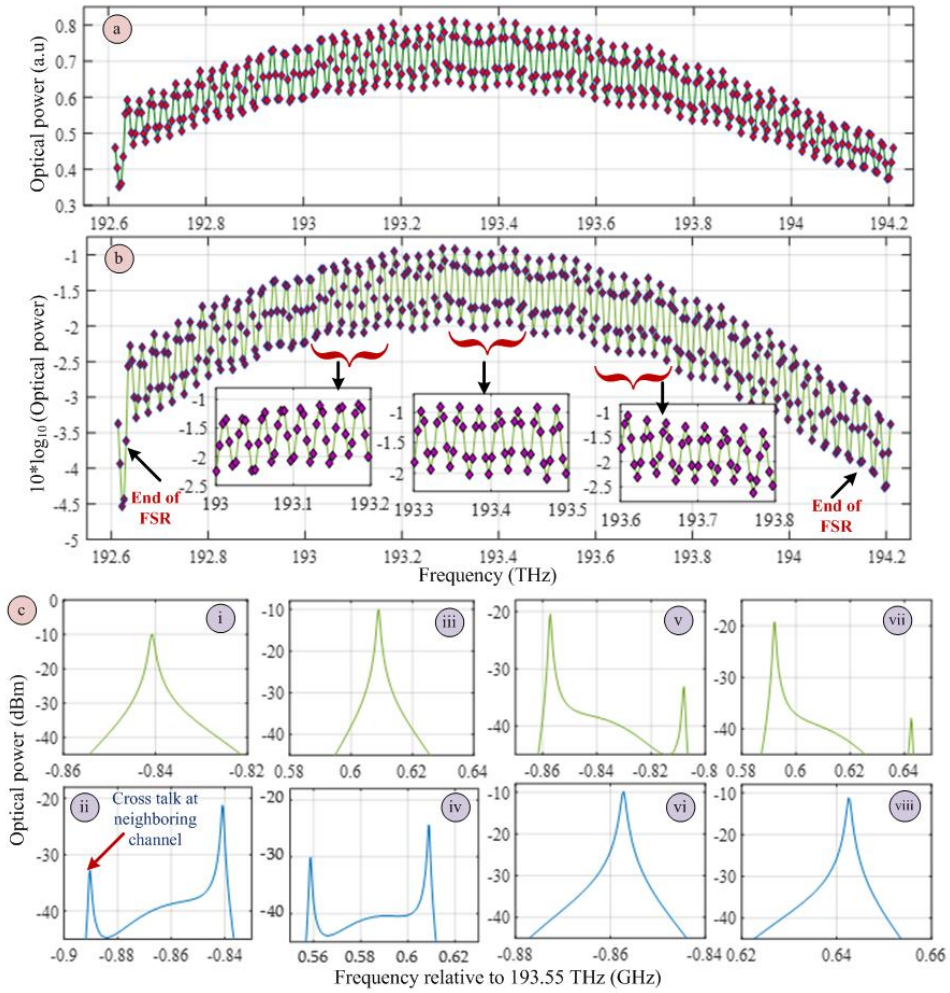

Fig. 11. Simulated result of the whole circuit when light is launched from input channel four (4) of both AWG; (a) optical power available at the PIN photodiode as a function of frequency; (b) logarithmic representation of the optical power measured in (a); (c) optical spectrum at the left (i-ii & v-vi) and right edges channel (iii-iv & vii-viii) of the AWG FSR for 0˚ and 120˚ degree position of the RR respectively. Upper row represents the spectrum of AWG_1 while lower row represents the spectrum of AWG_2.

Finally, the simulation results obtained using components designed for fabrication bode well for sensing the whole C-band with high resolution bandwidth albeit with some ripple present in the detectable optical power which may be corrected, if required, by digital signal processing to provide the quantitative spectrum.

Conclusion

In summary, a simple circuit architecture for on-chip spectral monitor with high resolution is presented. The newly proposed signal processing method and feasibility for photonic integration places the spectrometer in the forefront of the state of the art. Detailed simulation results are presented using constructor design data. The CMOS compatible Si_3N_4 platform is selected for fabrication due to its low loss and maturity. Simulation result verify that the spectrum monitoring can be performed over the entire C-band with peak power flatness ∼1→1.25 dB. The incoherent summation architecture proposed herein is less compact but is more robust to fabrication process variations than the coherent summation architecture proposed previously. A refinement of the architecture is proposed to provide a completely flat spectral response with zero adjacent channel crosstalk at least in theory. Finally, a novel circuit architecture using the combination of an optical switch and multi-input AWG is proposed as a practical more compact alternative implementation.

Funding

Huawei Canada sponsored research agreement ‘Research on ultra-high resolution on-chip spectrometer’.

Acknowledgments
Mehedi Hasan acknowledges the Natural Sciences and Engineering Research Council of Canada (NSERC) for their support through the Vanier Canada Graduate Scholarship program. Trevor J. Hall is grateful to Huawei, Canada for their support of this work. Trevor J. Hall is also grateful to the University of Ottawa for their support of a University Research Chair.

Disclosures
The authors declare no conflicts of interest.

References

1. Z. Xia, A. A. Eftekhar, M. Soltani, B. Momeni, Q. Li, M. Chamanzar, S. Yegnanarayanan, and A. Adibi, "High resolution on-chip spectroscopy based on miniaturized microdonut resonators," Opt. Express 19, 12356-12364 (2011).
2. C. Xiang, P.A. Morton, J. Khurgin, C. Morton, and J. E. Bowers, "Widely tunable Si3N4 triple-ring and quad-ring resonator laser reflectors and filters," IEEE 15th International conference on group IV photonics, Cancun, Mexico, 1-2 (2018).
3. Y. Li, J. Li, H. Yu, H. Yu, H. Chen, S. Yang, and M. Chen, "On-chip photonic microsystem for optical signal processing based on silicon and silicon nitride platforms," Adv. Opt. Technol. 7, 81-101 (2018).
4. M. Kita, H. lin, A. Agarwal, K. Richardson, I. Luzinov, T. Gu, and J. Hu, "On-chip infrared spectroscopic sensing: Redefining the benefits of scaling," IEEE J. Sel. Topics in Quantum Electron. 23, 340-349, (2017).
5. Elham Heidari, Xiaochuan Xu, Chi-Jui Chung, and Ray T. Chen, "On-chip Fourier transform spectrometer on silicon-on-sapphire," Opt. Lett. 44, 2883-2886 (2019).
6. E. Ryckeboer, A. Gassenq, M. Muneeb, N. Hattasan, S. Pathak, L. Cerutti, J.B. Rodriguez, E. Tournié, W. Bogaerts, R. Baets, and G. Roelkens, "Silicon-on-insulator spectrometers with integrated GaInAsSb photodiodes for wide-band spectroscopy from 1510 to 2300 nm," Opt. Express 21, 6101-6108 (2013).
7. X. Ma, M. Li and J. He, "CMOS-compatible integrated spectrometer based on echelle diffraction grating and MSM photodetector array," IEEE Photonics J. 5, 6600807-6600807 (2013).
8. B. Kyotoku, L. Chen, and M. Lipson, "Sub-nm resolution cavity enhanced micro-spectrometer," Opt. Express 18, 102-107 (2010).
9. G. Yurtsever, and R. Baets, "Integrated spectrometer on silicon on insulator," 16th Annual Symposium of the IEEE photonics, Ghent, Belgium, 273-276 (2011).
10. M. Hasan, M. Rad, G.M. Hasan, P. Liu, P. Dumais, E. Bernier and T. J. Hall, "Ultra-high resolution wideband On-chip spectrometer," IEEE Photonics J. 12, 1-17 (2020).
11. C. G. H. Roeloffzen , M. Hoekman , E. J. Klein, L. S. Wevers, R. B. Timens , D. Marchenko, D. Geskus, R. Dekker, A. Alippi, R. Grootjans, A. V. Rees , R. M. Oldenbeuving, J. P. Epping, R. G. Heideman, K. Wörhoff, A. Leinse, D. Geuzebroek , E. Schreuder, P. W. L. Van Dijk, I. Visscher, C. Taddei , Y. Fan , C. Taballione, Y. Liu , D. Marpaung , L. Zhuang , M. Benelajla, K.-J. Boller, 'Low-loss Si3N4 TriPleX optical waveguides: technology and applications overview', IEEE J. Sel. Topics in Quantum Electron. 24, 4400321, (2018).
12. L. Zhuang, D. Marpaung, M. Burla, W. Beeker, A. Leinse, and C. Roeloffzen, "Low-loss, high-index-contrast Si3N4/SiO2 optical waveguides for optical delay lines in microwave photonics signal processing," Opt. Express 19, 23162-23170 (2011).
13. Xie, Y., Zhuang, L. & Lowery, A., Picosecond optical pulse processing using a terahertz-bandwidth reconfigurable photonic integrated circuit. Nanophotonics 7, 837-852 (2018).
14. D. Seyringer, M. Sagmeister, A. Maese‐Novo, M. Eggeling, E. Rank4, P. Muellner, R. Hainberger, W. Drexler, M. Vlaskovic, H. Zimmermann, G. Meinhardt, J. Kraft, 'Technological verification of size‐optimized 160‐channel silicon nitride‐based AWG-spectrometer for medical applications', Applied Physics B, 125: 88, (2019).
15. https://www.neophotonics.com/products/dwdm-mux-dmux-athermal-awg/.
16. E. Kleijn, E. M. van Vliet, D. Pustakhod, M. K. Smit and X. J. M. Leijtens, "Amplitude and Phase Error Correction Algorithm for 3X3 MMI Based Mach–Zehnder Interferometers," Journal of Lightwave Technology, vol. 33, no. 11, pp. 2233-2239, June 2015.
17. J. F. Bauters, M. J. R. Heck, D. D. John, J. S. Barton, C. M. Bruinink, A. Leinse, R. G. Heideman, D. J. Blumenthal, J. E. Bowers, "Planar waveguides with less than 0.1 dB/m propagation loss fabricated with wafer bonding," Opt. Exp. 19, 24090-24101 (2011).
18. L. Chang, M. H. P. Pfeiffer, N. Volet, M. Zervas, J. D. Peters, C. L. Manganelli, E. J. Stanton, Y. Li, T. J. Kippenberg, J. E. Bowers, "Heterogeneous integration of lithium niobate and silicon nitride waveguides for wafer-scale photonic integrated circuits on silicon", Opt. Lett., 42, 803-806 (2017).
19. W. Jin, R. G. Polcawich, P. A. Morton, J. E. Bowers, "Piezoelectrically tuned silicon nitride ring resonator," Opt. Exp. 26, 3174-3187 (2018).
20. A. N. R. Ahmed, S. Shi, M. Zablocki, P. Yao, D. W. Prather, "Tunable hybrid silicon nitride and thin-film lithium niobate electro-optic micro resonator," Opt. Lett. 44, 618-621, (2019)

CHAPTER 4

Frequency shifting/SSB modulation

4.1 Summary

Theoretical modelling of a photonic integrated circuit based on a two-stage cascaded MZM architecture for in-phase & quadrature phase (IQ) RF modulation in general and specifically frequency up conversion/frequency shifting is proposed. Hither to, there has been no disclosure in the scientific literature of cascaded MZM circuit architecture capable of these functions. In the proposed design, a 1×2 splitter is used at the input, a 2×1 combiner is used at the output, and a 2×2 coupler interconnects the two stages. A 2×2 MMI or 2×2 directional coupler (DC) may be used in each of these positions. The dynamic phase shift is provided by driving one stage by the in-phase signal and driving the other stage by the quadrature-phase signal. The first and second 2×2 MMI/DC with the first stage phase-modulators together form a 2×2 MZM, i.e. an MZM with two input ports and two output ports. The innovation here is that the exit coupler of a first stage 2×2 MZM and the entrance coupler of the second stage 2×2 MZM are merged together to form a special coupling and phase bias component. An immediate consequence is that there is no intrinsic loss introduced between the two stages which reduces the optical insertion loss by 3-dB compared to the orthodox arrangement. Each light path is modulated twice (1^{st} stage & 2^{nd} stage) in this architecture, so the RF power required to achieve a specified phase modulation magnitude is 3-dB less than the RF power required for the same phase modulation by a parallel MZM architecture, which modulates each light path only once. Hence, the proposed circuit is 6-dB (3-dB optical and 3-dB electrical) advantageous compared to the functionally equivalent DP-MZM. The experimental verification of the energy efficient I-Q modulator has also been demonstrated. photonic integrated circuit fabricated by University of Laval group for another application containing a three-stage cascaded MZM circuit was adapted to the purpose of the experimental verification. In addition, an alternative implementation based on polarization modulators is presented.

4.2 Contribution

The theoretical modelling part of this chapter were published in *Optics Letters* and *Journal of Modern Optics* respectively. I contributed the original idea, formulated the theoretical model, performed the numerical simulations, generated the result and wrote the manuscript. Dr. Hall contributed to the theoretical modelling and revised the manuscript. The experimental demonstration part was published in *Photonics Technology Letters.* I performed the experiment and wrote the manuscript. Dr. Hall and Prof. Sophie Larochelle from University of Laval edited the manuscript. Mr. Omid Jafari and Mr. Xun Guan contributed to the alignment of the light input to- and output from the tested photonic integrated circuit.

4.3 Article

This section is a reproduction of articles published in Optics Letters, IEEE Photonic Technology Letters and Journal of Modern Optics.

M. Hasan, and T. Hall, "Cascade photonic integrated circuit architecture for electro-optic I-Q / SSB modulation or frequency conversion," *Optics Letters* 40(21), 5038-5041 (2015).

M. Hasan, O. Jafari, X. Guan, L. A. Rusch, S. Larochelle, and T. J. Hall, "Experimental demonstration of SSB modulation/ frequency conversion using cascaded silicon MZM" *IEEE Photonics Technology Letters* 32 (18), 1147-1150 (2020).

M. Hasan and T. J. Hall, "Complex modulation using tandem polarization modulators," *Journal of Modern Optics* 64(20), 2268-2272 (2017).

Cascade photonic integrated circuit architecture for electro-optic In-phase Quadrature / Single Side Band modulation or frequency conversion

Mehedi Hasan[1,*] Trevor Hall,[1]

[1] Photonic Technology Laboratory, University of Ottawa, 800 King Edward Avenue, Ottawa, K1N 6N5, ON, Canada

A Photonic integrated circuit architecture for implementing frequency up-conversion is proposed. The circuit consists of a 1×2 splitter and 2×1 combiner interconnected by two stages of differentially driven phase modulators having a 2×2 MMI between the stages. A transfer matrix approach is used to model the operation of the architecture. The predictions of the model are validated by simulations performed using an industry standard software tool. The intrinsic conversion efficiency of the proposed design is improved by 6 dB over the alternative functionally equivalent circuit based on dual parallel Mach-Zehnder modulators known in the prior art. A two-tone analysis is presented to study the linearity of the proposed circuit and a comparison is provided over the alternative. The proposed circuit is suitable for integration in any platform that offers linear electro-optic phase modulation such as $LiNbO_3$, Silicon, III-V or hybrid technology.

OCIS codes: *(250.5300) Photonic Integrated Circuits, (060.5625) Radio frequency photonics, (130.4110) Modulators*

http://dx.doi.org/10.1364/OL.99.099999

Electro-optic in-phase–quadrature (I-Q) modulation or single side-band (SSB) modulation or frequency conversion are functions ('the desired function') fundamental to radio frequency photonic systems. To the best of the authors' knowledge, an integrated SSB modulator based on a Ti-diffused $LiNbO_3$ optical waveguide circuit driven by an in-phase and quadrature signal at 2 GHz. was reported for the first time in 1981 [1]. The circuit configuration used is same as the dual-parallel Mach-Zhender modulator (DP-MZM) used today. Since then, there has been a plethora of publications [2-13] describing different techniques of achieving the desired function. In [2-4] the desired function is achieved by electro-optic amplitude modulation of an optical carrier. A custom electro-absorption modulator (EAM), driven by a mm-wave RF source, is used to externally amplitude-modulate a distributed feedback laser (DFB) and a fibre-Bragg grating (FBG)) is used to extract a single side-band. The conversion efficiency is low, which reduces receiver sensitivity. Moreover, the EAM, DFB laser, and FBG must be very closely matched in frequency of operation that entails temperature control, which is undesirable in terms of energy consumption. Alternatively, the desired function is achieved by electro-optic phase-modulation of an optical carrier. Typically, pairs of phase modulators are combined to form Mach-Zehnder modulators (MZMs), which are used to amplitude-modulate the in-phase (I) and quadrature (Q) components of the optical carrier. Circuit architectures using a dual-drive MZM (DD-MZM) [5-7], two DD-MZM [8] and a DP-MZM [9] have been investigated. The use of the intrinsic phase relationship between ports of a multimode interference coupler (MMI) coupler has been proposed to improve the linearity of an electro-optic modulator by selective suppression of unwanted inter-modulation products [10-11]. A requirement for precise RF-drive level, static DC bias of the electro-optic modulators, and/or passive phase shift elements are common features of most designs. A notable advance, reported in [12-13], are DC bias-less and filter-less architectures with no requirement to set a precise electrical drive level. Most reported architectures [1, 5-13] are directly equivalent to single stage generalized Mach-Zehnder Interferometer (GMZI) circuit: a $1 \times N$ splitter directly interconnected to a $N \times 1$ combiner via an array of N linear electro-optic phase modulators. Few two-stage architectures have been reported and, to the best of the authors' knowledge, none reported capable of the desired function; only architectures useful for frequency-multiplication are known in the prior art [14]. The search for a two-stage architecture capable of the desired function was motivated by the authors' finding [15]- that a two-stage MZM architecture for frequency multiplication required 3 dB less RF-drive power than its functionally equivalent GMZI architecture. As far as the authors are aware, a two-stage MZM capable of performing the desired function is reported for the first time in this letter. The proposed design has a 6 dB conversion gain advantage compared to a single stage circuit, for example, a DP-MZM. Fig. 1 shows a schematic of the proposed circuit. Three splitter / combiners are interconnected by two stages of differential phase shifters. A 1×2 splitter is used at the input, a 2×1 combiner is used at the output, and a 2×2 coupler interconnects the two stages. A 2×2 MMI or 2×2 directional coupler (DC) may be used in each of these positions. The dynamic phase shift is provided by driving one stage by the in-phase signal and driving the other stage by the quadrature signal. The first and second 2×2 MMI/DC with the first stage phase-modulators together form a 2×2 MZM, i.e. an MZM with two input ports and two output ports. Similarly, the second 2×2 MMI/DC with the second stage phase-modulators together form a MZM with two input ports and two output ports. Standard MZM are often equipped with only one input and one output port. A cascade of such two such MZM stages results in a back-to-back arrangement of a 2×1 and 1×2 combiner and splitter at their interface. This constrains the phase shifts experienced by the four light-paths that traverse the structure preventing the provision of useful functions for odd order sidebands of the carrier induced by the phase modulation.

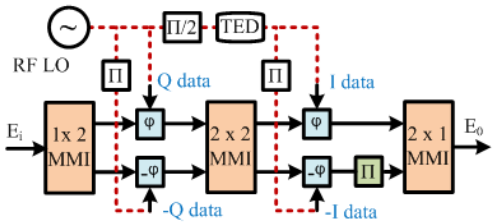

Fig. 1. Schematic diagram of the proposed design; RF LO, radio frequency local oscillator; TED, tunable electrical delay; I, in-phase; Q, quadrature.

The innovation here is that the exit coupler of a first stage 2×2 MZM and the entrance coupler of the second stage 2×2 MZM are merged together to form a special coupling and phase bias component. With the addition of a static phase shift of π in one arm of the second stage the desired functions are enabled. An immediate consequence is that there is no intrinsic loss introduced between the two stages which reduces the insertion loss by 3 dB compared to the orthodox arrangement. The static phase-shift may be distributed more symmetrically around the input and output ports of the central coupler to emphasize its role as a special coupling and phase bias element and provided either by appropriate dc-biasing of the phase modulator(s) or via a passive waveguide element(s).

For simplicity, initially assume there is negligible propagation delay between the stages. Using a transfer matrix approach, the output of the whole circuit is given by:

$$E_0 = \frac{1}{2\sqrt{2}}[1 \quad 1]\begin{bmatrix}1 & 0\\ 0 & -1\end{bmatrix}[T_2]\begin{bmatrix}1 & -i\\ -i & 1\end{bmatrix}[T_1]\begin{bmatrix}1\\ 1\end{bmatrix}E_i. \qquad \textbf{(1)}$$

where

$$\frac{1}{\sqrt{2}}\begin{bmatrix}1\\ 1\end{bmatrix};\ \frac{1}{\sqrt{2}}\begin{bmatrix}1 & -i\\ -i & 1\end{bmatrix};\ \text{and}\ \frac{1}{\sqrt{2}}[1 \quad 1]$$

are the transfer matrix of 1×2 MMI, 2×2 MMI and 2×1 MMI respectively; and,

$$T_1 = \begin{bmatrix}e^{i\varphi_1} & 0\\ 0 & e^{-i\varphi_1}\end{bmatrix} \quad \& \quad T_2 = \begin{bmatrix}e^{i\varphi_2} & 0\\ 0 & e^{-i\varphi_2}\end{bmatrix}.$$

are the transfer matrix of the 1st stage and 2nd stage optical phase modulators. Here:

$$\varphi_j = \pi v_j(t)/v_\pi. \qquad \textbf{(2)}$$

is the optical phase shift induced by the RF signal, $v(t)$, and v_π is the half-wave voltage that characterizes the phase modulators. Simplifying Eq. (1) gives:

$$E_0 = \frac{1}{\sqrt{2}}i[sin(\varphi_1 + \varphi_2) + i\, sin(\varphi_1 - \varphi_2)]E_i. \qquad \textbf{(3)}$$

If one sets:

$$v_1 + v_2 = \sqrt{2}v_I \quad \& \quad v_1 - v_2 = \sqrt{2}v_Q \qquad \textbf{(4)}$$

Then for $|v_I|, |v_Q| \ll v_\pi$ one finds:

$$E_0 = \frac{\pi}{v_\pi}i(v_I + iv_Q)E_i. \qquad \textbf{(5)}$$

It is clear that the circuit acts as an I-Q modulator up to an irrelevant overall carrier phase shift. For large signals, the I and Q inputs should be pre-distorted to compensate the sine function characteristic. This is straight forward to implement for digital modulation formats. Note that one may directly connect the I and Q channels to electrical ports 1 and 2. This follows from the fact that a linear combination of the I and Q channels that conserves power is equivalent to a rotation of the constellation which is equivalent to a carrier phase shift. For example, let:

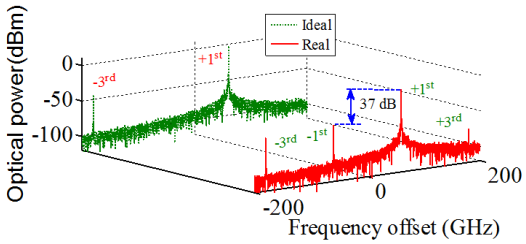

Fig. 2. Optical spectra for frequency up-conversion. The optical noise floor is determined by the laser line-width. A resolution bandwidth of 156.25 MHz is used for the optical spectrum analyzer.

$$v_1 = v_Q \quad \& \quad v_2 = v_I \qquad \textbf{(6)}$$

Then:

$$\begin{aligned} E_0/E_i &= i\frac{1}{\sqrt{2}}\frac{\pi}{v_\pi}\left[(v_Q + v_I) + i(v_Q - v_I)\right] \\ &= \frac{\pi}{v_\pi}\frac{1}{\sqrt{2}}(1+i)(v_I + iv_Q) \\ &= \frac{\pi}{v_\pi}(v_I + iv_Q)\, exp(i\pi/4) \end{aligned} \qquad \textbf{(7)}$$

In the case of an applied RF-signal with peak amplitude of v_{RF} and frequency ω of the form:

$$v_1(t) = v_{RF}\, sin(\omega t) \quad \& \quad v_2(t) = v_{RF}\, cos(\omega t) \qquad \textbf{(8)}$$

it follows immediately that the circuit provides upper single side band modulation or equivalently acts as an electro-optic up-conversion mixer (inverting the quadrature drive provides the lower sideband).

Eq. (5) & (7), invoke a small RF signal condition, $v_{RF}/v_\pi \ll 1$, a non-necessary condition if recourse is made to the Jacobi-Anger expansion, which yields:

$$E_0 = \sqrt{2}\sum_{n=0}^{\infty}(-1)^n J_{2n+1}(m)exp[(-1)^n(2n+1)\omega t]E_i \qquad \textbf{(9)}$$

where, J_{2n+1} is the Bessel function of the first kind of order $2n+1$ and

$$m = \sqrt{2}\pi\frac{v_{RF}}{v_\pi} \qquad \textbf{(10)}$$

It can be seen from Eq. (9) that all even orders are suppressed, including the carrier. The principal side-bands are -3, 1 and 5. The $\sqrt{2}$ pre-factor in Eq. (9) & (10) yield the 3 dB optical and 3 dB electrical advantages of the proposed architecture over the circuits presented in [12-13].

Due to the nonlinearity of the MZM, the proposed circuit will generate nonlinear distortions such as intermodulation distortions (IMDs) and harmonic distortions. The third-order IMD (IMD3) dominates the IMD as it has components with frequencies that fall within the band of interest which cannot be removed by filtering. Two complex tones $v_{RF}e^{i\omega_1 t}$ and $v_{RF}e^{i\omega_2 t}$ are applied to the input of the proposed I/Q modulator, such that the real and imaginary parts of the RF drive signals are:

$$v_I = v_{RF}(cos\omega_1 t + cos\omega_2 t)$$
$$v_Q = v_{RF}(sin\omega_1 t + sin\omega_2 t) \quad \textbf{(11)}$$

For $\varphi_j \ll 1$ Eq. (3) may be approximated using the Taylor series expansion to give

$$E_0 = \frac{1}{\sqrt{2}} i[\{(\varphi_1 + \varphi_2) + i(\varphi_1 - \varphi_2)\} - 1/3!\{(\varphi_1 + \varphi_2) + i(\varphi_1 - \varphi_2)\}^3]E_i. \quad \textbf{(12)}$$

Substituting Eq. (11) into Eq. (12) making use of Eq. (2) and simplifying, the component of the output at the signal frequencies is:

$$E_{\omega_{1,2}} = E_i \left\{\frac{\pi v_{RF}}{v_\pi} - \frac{3}{4}\left(\frac{\pi v_{RF}}{v_\pi}\right)^3\right\} e^{i\omega_{1,2}t} e^{\frac{i\pi}{4}}. \quad \textbf{(13)}$$

The component of the output with frequency $(2\omega_{1,2} - \omega_{2,1})$ is:

$$E_{2\omega_{1,2}-\omega_{2,1}} = E_i \left\{\frac{1}{4}\left(\frac{\pi v_{RF}}{v_\pi}\right)^3\right\} e^{i(2\omega_{1,2}-\omega_{2,1})t} e^{\frac{i\pi}{4}}. \quad \textbf{(14)}$$

The component of the output at frequency $(3\omega_{1,2})$ is:

$$E_{3\omega_{1,2}} = E_i \left\{\frac{1}{12}\left(\frac{\pi v_{RF}}{v_\pi}\right)^3\right\} e^{i(3\omega_{1,2})t} e^{\frac{i\pi}{4}}. \quad \textbf{(15)}$$

The optical signal at the output of parallel MZM configuration with identical function [12-13] is:

$$E_0 = \frac{1}{2}[sin(\varphi_1) + i\, sin(\varphi_2)]E_i. \quad \textbf{(16)}$$

For $\varphi_j \ll 1$, Eq. (16) may be approximated using the Taylor series expansion to give:

$$E_0 = \frac{1}{2}[\{(\varphi_1) + i(\varphi_2)\} - \frac{1}{3!}\{(\varphi_1) + i(\varphi_2)\}^3]E_i. \quad \textbf{(17)}$$

Following the same procedure as before components of the output at the signal frequencies, in-band IMD3 and the third harmonic components are:

$$E_{\omega_{1,2}} = E_i \left\{\frac{1}{2}\frac{\pi v_{RF}}{v_\pi} - \frac{3}{16}\left(\frac{\pi v_{RF}}{v_\pi}\right)^3\right\} e^{i\omega_{1,2}t}. \quad \textbf{(18)}$$

$$E_{2\omega_{1,2}-\omega_{2,1}} = E_i \left\{\frac{1}{16}\left(\frac{\pi v_{RF}}{v_\pi}\right)^3\right\} e^{i(2\omega_{1,2}-\omega_{2,1})t}. \quad \textbf{(19)}$$

$$\boldsymbol{E_{3\omega_{1,2}} = E_i \left\{\frac{1}{48}\left(\frac{\pi v_{RF}}{v_\pi}\right)^3\right\} e^{i(3\omega_{1,2})t}}. \quad \textbf{(20)}$$

If one compensates for the reduced power requirement and reduced insertion loss of the cascade architecture compared to the parallel architecture by setting $v_{RF} \rightarrow (1/\sqrt{2})v_{RF}$ & $E_{in} \rightarrow (1/\sqrt{2})E_{in}$ in Eq. (13), (14) and (15), then Eq. (13) becomes equal to Eq. (18), Eq. (14) becomes equal to Eq. (19) and Eq. (15) as same as Eq. (20). Hence, for same output optical power, the proposed circuit requires 6 dB (3 dB optical and 3 dB electrical) less power than the parallel circuit presented in [10-12] and has exactly the same intermodulation distortion.

A simulation using the industry standard (VPIphotonicsTM) software tool is used to verify the operation of the proposed architecture. A continuous wave DFB laser diode set at 1550 nm, power of 5 mW, and line-width of 200 kHz is used as the optical input. Ideal phase modulators are used. Y-splitter, optical coupler and Y-combiner are selected from the Photonic-Integrated Circuit library. A RF driving signal of peak amplitude $v_{RF} = 0.1v_\pi$ ($v_\pi = 1$ volts) volts with 60 GHz angular frequency is applied to the four phase modulators with phase relation of $0, +\pi$ to the first stage and $+\pi/2$ and $-\pi/2$ to the second stage. Fig. 2 shows the optical spectrum of the resultant upper side-band which verifies the theoretical prediction.

VPI simulates the Y-splitter, optical coupler and Y-combiner as ideal components, i.e. there is no propagation delay associated between the input and output light-wave when it travels through the components. In practice, the input light-wave will encounter a propagation delay at the output of the first stage (output of the 2×2 MMI according to Fig. 1) and hence the RF drive to the second stage needs to be delayed by the same amount to ensure proper operation. VPI simulates an MMI as a real device. Hence the circuit was also simulated with the Y-splitter, optical coupler and Y-combiner replaced by a 1×2 MMI splitter, 2×2 MMI coupler and 2×1 MMI combiner. An optical delta pulse is first applied to a 2×2 MMI in order to determine its propagation delay. Fig. 3 (a) shows the relation between input and output optical pulse shape. The length of the MMI was found from the field distribution, which is 1030 µm approximately. The propagation delay τ can be calculated from $\tau = Ln/c$, where L is the length of the MMI, n is the refractive index and c is the velocity of light. For a refractive index of 1.50, τ is calculated as 5.15 ns. Adjusting the delay provided by the tunable electrical delay line to 5.15 ns, the output of the circuit is as shown in Fig. 2 (real). It shows that the harmonics of interest (+1st) is 37 dB greater than the unwanted harmonics (-1st). It is clear from Fig. 3 (a), the output optical pulse is not only delayed but also broadened as many modes travel the whole length of MMI. Fine tuning of the electrical delay line about the theoretical delay results in improved suppression of unwanted harmonics. Fig. 3 (b) shows the optical spectrum of the proposed circuit when the delay is set to 5.22 ns. It shows that the unwanted -1st harmonics is suppressed almost completely. A side harmonic suppression ratio of more than 40 dB is achieved in this case. Furthermore, in practice the length of 2×2 MMI

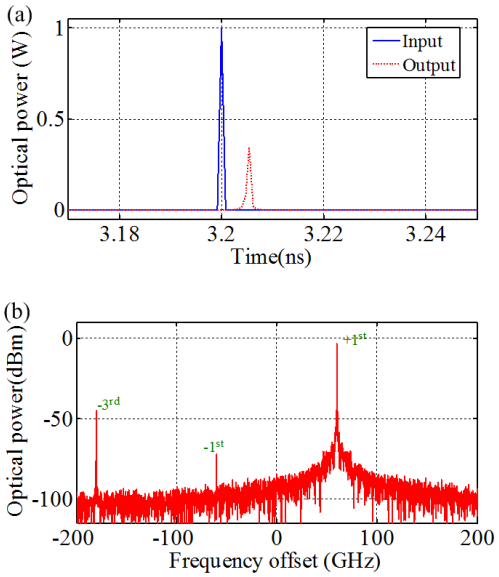

Fig. 3. (a) Propagation delay between the input and output optical signal of a 2×2 MMI. (b) Optical spectra for frequency up-conversion with adjusted propagation delay.

for high index contrast integration platform can be much smaller (~48 μm), which decreases both the delay and the delay spread.

To assess the linearity of the proposed circuit, the output optical power of the first-order harmonic (FOH), third-order harmonic and third-order intermodulation product calculated from two-tone analysis (both numerical and simulation) is plotted in Fig. 4 as a function of applied RF voltage. As described in the mathematical analysis, the IMD3 is more dominant than the third order harmonic. Furthermore, the simulation verification validates the numerical simulation up to an applied RF voltage of 0.3 volt approximately, beyond which contribution from high order terms cause a deviation. The linearity of the proposed circuit described through the relation between the FOH at ω_1 and the third-order intermodulation product at $(2\omega_1 - \omega_2)$ is illustrated in Fig. 4. For a 50 Ω load, an input RF power of −30 dBm (modulation index m is about 0.044), the ratio of FOH to IMD3 achieved is over 55 dB. As the RF power increases, the ratio decreases. For an input RF power of -5 dBm (modulation index m is about 0.79), the ratio of FOH to the IMD3 decreases to 20 dB; suggesting the end of the linear region. The simulation results show that the proposed up-conversion mixer can be a very effective solution for the transport of weak RF signals given sufficient the receiver sensitivity.

The performance of the proposed circuit may deviate from ideal due to various reasons. It is reported [16] that the length of the waveguides connected between the RF drive signal and the phase modulators is the critical part of the design compared to the phase errors and power imbalances between the ports of MMIs. As a tunable electrical delay is used at the second stage to compensate the propagation delay introduced at the first stage, a further precise tuning can overcome the relative phase errors of RF drive signals. On the other hand, using a sub-wavelength engineered MMI, the phase errors and power imbalances between the output ports can be substantially reduced compared to a conventional MMI and assure broadband operation [17].

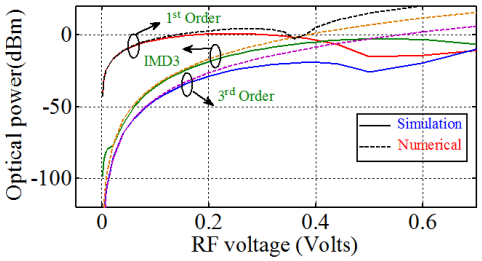

Fig. 4. Output power of fundamental signal, third-order harmonics and third-order IMD as a function of applied RF voltage ($volt$).

In summary, a photonic integrated circuit based on a two stage MZM architecture has been proposed for frequency up-conversion of an electrical domain signal to the optical domain. Theoretical analysis and simulation verification show that the proposed circuit is 6 dB advantageous than the functionally equivalent single stage parallel structure. The circuit can also be used for complex modulation. The linearity of the I/Q modulator has been analyzed and the simulation results illustrate the range of operation of the modulator. In addition to the mature $LiNbO_3$ technology, recent developments of linear electro-optic phase modulators based on Silicon or Silicon hybrid [18-19] or III-V [20] with preferred photonic integration technology [21] makes the implementation of the circuit practical.

Funding. Natural Sciences and Engineering Research Council of Canada (NSERC); Canada Research Chairs (CRC) Program.

References

1. M. Izutsu, S. Shikama, and T. Sueta, IEEE J. of Quntum. Electron. **17**, 2225 (1981).
2. M.-T. Zhou, A. B. Sharma, Z.-H. Shao, and M. Fujise, Int. Topical Meeting on Microw. Photon., Seoul, Korea, (2005), 121-124.
3. D. Zibar, R. Sambaraju, A. C. Jambrina , R. Alemany, J. Herrera, and I. T. Monroy, ECOC, Torino, Italy, (2010).
4. A. Caballero, D. Zibar, R. Sambaraju, J. Marti, and I. T. Monroy, Journal of Lightwave Technol. **30**, 147 (2012).
5. G. H. Smith, D. Novak, and Z. Ahmed, IEEE Trans. Microw. Theory Techn. **45**, 1410 (1997).
6. G. H. Smith, D. Novak, and Z. Ahmed, Electron. Lett. **33**, 74 (1997).
7. J. Yu, Z. Jia, L. Yi, Y. Su, G.-K. Chang, and T. Wang, IEEE Photon. Technol. Lett. **18**, 265 (2006).
8. A. Wen, M. Li, L. Shang, and Y. Chen, Opt. & Laser Technol. **43**, 1061 (2011).
9. C. W. Chow, C. H. Wang, C. H. Yeh, and S. Chi, Opt. Express **19**, 10973 (2011).
10. J.-G. Zhao, Z.-J. Liu, X.-L. Liu, T. Shang, and P. Yue, Opt. Commun. **282**, 4353 (2009).
11. J.-G. Zhao, Z. J. Liu, X.-L. Liu, T. Shang, and P. Yue, IET Optoelectron. **4**, 183 (2010).
12. M. Hasan, R. Maldonado-Basilio, and T. J. Hall, Opt. Lett. **40**, 2501 (2015).
13. R. Maldonado-Basilio, M. Hasan, H. Nikkhah, S. Abdul-Majid, R. Guemri, F. Lucarz, J.-L. de Bougrenet de la Tocnaye, and T. J. Hall, J. of Mod. Opt. **62**, 1405 (2015).
14. W. Li, and J. Yao, IEEE Trans. on Microwave Theory and Techn. **58**, 3259 (2010).
15. M. Hasan, and T. J. Hall, "A photonic frequency octo-tupler with reduced RF drive power and extended spurious sideband suppression," Opt. and Laser Technol., (Submitted).
16. M. Hasan, R. Maldonado-Basilio, F. Lucarz, J-L de Bougrenet and T. J. Hall, Opt. Lett. **39**, 6950, (2014).
17. R. Halir, P. J. Bock, P. Cheben, A. Ortega-Monux, C. Alonso-Ramos, J. H. Schmid, J. Lapointe, D. Xu, J. G. Wanguemert-Perez, I Molina-Fernandez, and S. Janz, Laser Photonics Rev. **9**, 25 (2015).
18. D. Korn, R. Palmer, H. Yu, P. C. Schindler, L. Alloatti, M. Baier, R. Schmogrow, W. Bogaerts, S. K. Selvaraja, G. Lepage, M. Pantouvaki, J. M. D. Wouters, P. Verheyen, J. V. Campenhout, B. Chen, R. Baets, P. Absil, R. Dinu, C. Koos, W. Freude, and J. Leuthold, Opt. Express **21**, 13219 (2013).
19. S. Dogru, and N. Dagli, Opt. Lett. **39**, 6074 (2014).
20. M. J. R. Heck, J. F. Bauters, M. L. Davenport, J. K. Doylend, S. Jain, G. Kurczveil, S. Srinivasan, Y. Tang, and J. E. Bowers, IEEE J. Sel. Topics Quantum Electron. **19**, 6100117 (2013).
21. D. Marpaung C. Roeloffzen, R. Heideman, A. Leinse, S. Sales, and J. Capmanyet, Laser Photonics Rev. **7**, 506 (2013).

Integrated optical SSB modulation / frequency shifting using cascaded silicon MZM

Mehedi Hasan, *Student Member, IEEE*, Omid Jafari, Xun Guan, Leslie A. Rusch, *Fellow, IEEE*, Sophie Larochelle, *Senior Member, IEEE* and Trevor Hall, *Senior Member, IEEE*

***Abstract*— A frequency conversion mixer or single side band modulator using two cascaded MZM is proven experimentally. The operation of the circuit is modelled by a transfer matrix approach and verified by simulation in support of the experiment. A 10 GHz shift of the optical carrier in both left and right direction is demonstrated. The residual sideband suppression relative to the enhanced sideband is 22 dB for the best cases. Numerical analysis shows that the circuit has 3-dB optical and 3-dB electrical intrinsic advantage over the functionally equivalent DP-MZM.**

***Index Terms*—MZM, SSB, SSB-SC, Silicon photonics, Photonic integrated circuit.**

INTRODUCTION

EFFICIENT single side band suppressed carrier (SSB-SC) modulation technology for frequency conversion or shifting is a growing need and fundamental to radio frequency photonic systems. Starting from the very first demonstration [1] of an integrated SSB modulator based on a Ti-diffused $LiNbO_3$ optical waveguide circuit driven by an in-phase (I) and quadrature (Q) signal at 2 GHz, there has been a plethora of publications [2-9] describing different techniques for obtaining the desired functions. All the architectures presented in references [1-5, 7-9] use circuits of Mach-Zehnder Modulators (MZM). Typically, pairs of electro-optic phase modulators are combined to form an MZM. A dual-drive MZM (DD-MZM) is used in [2, 4] to generate the SSB-SC modulation. In this scheme, the optical carrier is modulated by the in-phase and quadrature component of the RF drive signal. However, a dual-parallel Mach Zehnder Modulator (DP-MZM) is the most widely used solution because of its superior carrier and sideband suppression [3,5,7-9]. In this scheme, two child MZM are biased at the minimum transmission point (MITP) while the parent MZM is kept at the quadrature bias point (QTP). Then the I and Q components of the RF signal are applied to the two child MZM. The use of the intrinsic phase relationship between ports of a 1×3 multimode interference coupler (MMI) has been proposed for selective suppression of unwanted harmonics [6]. A notable advance on the design of the desired function is presented in [7] and a DC bias-less and filter-less scheme based on MMI couplers has been reported [8]. A silicon-based DP-MZM architecture for 1 GHz frequency shifting is reported in [9]. All these architectures are directly equivalent to a single stage generalized Mach-Zehnder Interferometer (GMZI) circuit: an $1\times N$ splitter directly interconnected to a $N\times 1$ combiner via an array of N linear electro-optic phase modulators. A search for a two-stage cascaded architecture capable of performing SSB was inspired by a publication on frequency multiplication [10]; a cascaded MZM structure requires 3-dB less RF power than the functionally equivalent parallel architecture. Finally, a cascaded MZM architecture capable of performing I-Q and/or SSB modulation with 6-dB intrinsic advantage (3-dB electrical and 3-dB optical) was proposed and verified by simulation in [11]. An alternative implementation based on polarization modulators was reported in [12]. This letter reports the test and measurement of a prototype cascaded MZM architecture on a silicon photonics platform that proves experimentally the proposed architecture and theoretical predictions disclosed in [11]. The three-stage cascaded MZM architecture was designed to be used as an optical digital-to-analog converter for high baud rate PAM transmission. It was fabricated on the same multi project wafer (MPW) run, and with the same RF transmission line design, as the single MZM with segmented

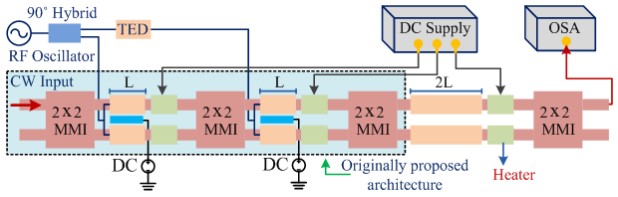

Fig. 1. Schematic diagram of the photonic integrated circuit architecture and experimental arrangement; OSA, optical spectrum analyzer; TED, tunable electrical delay; DC, direct current; CW, continuous wave.

Mehedi Hasan and Trevor Hall are with Photonic Technology Lab (PTL), University of Ottawa, 25 Templeton St, Ottawa, K1N 6X1, ON, Canada. Omid Jafari, Xun Guan, Leslie A. Rusch and Sophie Larochelle are with Centre d'optique, photonique et laser (COPL), Université Laval, 2375 rue de la Terrasse, Québec QC, Canada, G1V 0A6

electrodes in [13]. The details of the fabrication technology of the silicon photonic chip and the electrode electro-optic (E/O) characterization can be found in [13]. Ideally, the present demonstration of SSB generation would have required a two-stage cascaded MZ structure. Consequently, the three stage MZM, readily available in our laboratory, was adapted for this application by appropriate tuning of the exit stage.

PRINCIPAL OF OPERATION

Fig. 1 shows the schematic of the fabricated circuit architecture used for the experimental verification. The originally proposed circuit architecture consisting of two cascaded MZM is highlighted in the schematic. It can be seen that the original architecture is identical to the fabricated chip except for the last stage MMI. The novelty of the circuit architecture is the coupling between the two MZM used. A 2×2 MMI is used as the exit coupler of the 1st MZM and entrance coupler for the 2nd stage MZM. Thereby creating special coupling and phase bias. Since there is no unused port between the stages, the optical insertion loss is reduced by 3 dB from the orthodox arrangements given that the phase modulators are lossless (or negligible loss) and equal in length for both cascade and parallel cases. For lossy modulators, the optical advantage will be reduced by the attenuation of the additional stage. However, the architecture has less intrinsic loss due to reduced (halved) number of splitters and combiners. An additional 90˚ optical phase shift is required in both the stages for the target application. Each light path is modulated twice (1st stage & 2nd stage) in this architecture, so the RF power required to achieve a specified phase modulation magnitude is 3-dB less than the RF power required for the same phase modulation by a parallel MZM architecture, which modulates each light path only once. Hence, the proposed circuit is 6-dB (3-dB optical and 3-dB electrical) advantageous in principle.

To implement the same function using the three stage MZM, the 90˚ optical phase bias is applied in the 3rd stage instead of the 2nd stage as in the original design. The in-phase and quadrature-phase RF signal is applied to the 1st stage and 2nd stage respectively. The 2×2 MMI present in the fabricated chip are identical in design as in [14]. A thermo-optic phase shifter is present in each of the arms between stages. The modulator was fabricated at IME A*star on the same run and with the same electrode design as the segmented MZM in [13].

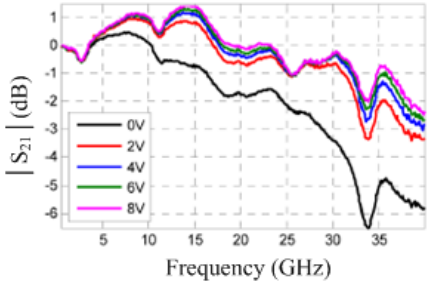

Fig. 2. Normalized E/O $|S_{21}|$ for 2000 μm long phase shifter with reverse bias voltages from 0 to 8 V. Adapted with permission from [1] © The Optical Society.

The phase-shifter length of the first two stages is L=1500 μm and 2L=3000 μm for the third stage, for a total phase shifter length of 6 mm (compared to 3.5 mm in [13]). The MZM is designed to be driven in a push-pull (PP) configuration. A 50 Ω termination is used in the MZM for impedance matching with the RF drivers. Deep UV photolithography is used to fabricate the modulator. The BOX thickness was 3μm, whereas a top-silicon layer of 200 nm was used in the wafer. The width of the modulator ridge waveguide is 500 nm; whereas slab thickness is 90 nm [13]. Figure 2 shows the E/O characterization of the modulator with a length of 2000 μm. The 3-dB bandwidth of the modulator is found to be ∼38 GHz. However, the bandwidth of the 1500 μm phase shifter will be greater than 38 GHz due to low microwave loss and reduced velocity mismatch between the optical and electrical wave.

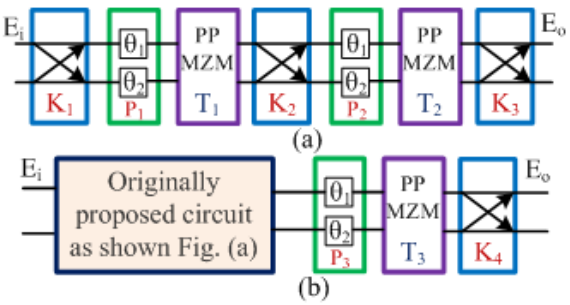

Fig. 3. Functional diagram; (a) originally proposed circuit; (b) circuit adopted for experimental demonstration; PP, push-pull.

Neglecting the propagation delay between the stages the functional diagram (Fig. 3) may be represented by transfer matrices. The output of the originally proposed circuit can be written:

$$E_o = \frac{1}{2\sqrt{2}} K_3 P_2 T_2 K_2 T_1 P_1 K_1 E_i \quad (1)$$

where:

$$K_j = \frac{1}{\sqrt{2}} \begin{bmatrix} 1 & -i \\ -i & 1 \end{bmatrix}$$

describes a 2× 2 MMI; and P_1, P_2 describe the static optical phase shifts applied in the 1st & 2nd stage MZM, respectively. Here, E_i and E_o are 2×1 column vectors. The choice of input and output port is determining which of their two elements is chosen as non-zero. Given an upper port input for upper sideband (USB) or lower sideband (LSB) modulation with upper (UEP) or lower (LEP) exit port:

$$P_1 = \begin{bmatrix} i & 0 \\ 0 & 1 \end{bmatrix} (USB) \quad ; \quad P_1 = \begin{bmatrix} 1 & 0 \\ 0 & i \end{bmatrix} (LSB)$$
$$P_2 = \begin{bmatrix} i & 0 \\ 0 & 1 \end{bmatrix} (UEP) \quad ; \quad P_2 = \begin{bmatrix} 1 & 0 \\ 0 & i \end{bmatrix} (LEP)$$

and:

$$T_1 = \begin{bmatrix} e^{i\varphi_1} & 0 \\ 0 & e^{-i\varphi_1} \end{bmatrix} \quad \& \quad T_2 = \begin{bmatrix} e^{i\varphi_2} & 0 \\ 0 & e^{-i\varphi_2} \end{bmatrix}$$

describe the 1st & 2nd stage optical phase modulators. Here:

$$\varphi_j = \pi \, v_j / v_\pi \quad (2)$$

is the optical phase shift induced by the RF signal v_j and v_π is the half-wave voltage of the phase modulators. Simplifying (1)

gives:

$$E_0 = \left(1/\sqrt{2}\right) i[\sin(\varphi_1 + \varphi_2) + i\sin(\varphi_1 - \varphi_2)]E_i \quad (3)$$

Setting:

$$v_1 = v_Q \quad \& \quad v_2 = v_I \quad (4)$$

then for $|v_I|, |v_Q| \ll v_\pi$

$$E_0/E_i = (\pi/v_\pi)\left(v_I + iv_Q\right)\exp(i\,\pi/4) \quad (5)$$

demonstrating that circuit performs I-Q modulation.

The implementation of the same function using a three-stage cascaded MZM is not as straight forward as described in the preceding. The second stage optical phase shift is applied in the 3rd stage to ensure the quadrature operation of the final stage MZM. On the other hand, the I and Q signals are applied in the 1st stage and 2nd stage MZM as per the originally proposed architecture. The total transmission may be written as:

$$E_o/E_i = (1/4)K_4P_3K_3T_2K_2T_1P_1K_1 \quad (6)$$

where P_1,P_2 are chosen as before. Equation (6) simplifies to:

$$E_0/E_i = (1/2)i[\sin(\varphi_1 + \varphi_2) + i\sin(\varphi_1 - \varphi_2)] \quad (7)$$

Equation (7) is identical to (3) except for the reduction of the optical amplitude by a factor of $1/\sqrt{2}$ due to the redundant 3rd stage of the photonic integrated circuit used. In the case of an applied RF-signal of the form:

$$v_1(t) = v_{RF}\cos(\omega t) \quad \& \quad v_2(t) = v_{RF}\sin(\omega t) \quad (8)$$

The circuit provides lower sideband modulation or frequency down conversion. By interchanging the drive signals, one can obtain frequency up-conversion or upper side band modulation. Hence, the circuit works as electro-optic up/down conversion mixer or frequency shifter. Invoking the Jacobi Anger expansion, Eq. (7) may be rewritten:

$$E_0/E_i = \sum_{n=0}^{\infty}(-1)^n J_{2n+1}(m)\exp\left[i(-1)^n(2n-1)\left(\omega t - \frac{\pi}{4}\right)\right] \quad (9)$$

where, J_ν is the Bessel function of the first kind of order ν and

$$m = \sqrt{2}\pi\, v_{RF}/v_\pi \quad (10)$$

is the modulation index. The pre-factor $\sqrt{2}$ confirms the 3-dB electrical advantage of the proposed architecture in comparison to circuits presented in [5, 8-9]. The 3-dB optical advantage is not realised because of the presence of the third stage. However, the original design confirms the 3-dB optical advantage as well. It can be understood from (9), that all the even harmonics are suppressed including the carrier. The principal sidebands are -1, +3, and -5.

RESULT

The circuit architecture proposed is validated by the industry-standard software tool (VPIphotonics™) and laboratory experiment. In the simulations, a 1540 nm CW-DFB laser having power of 0 dBm is used as the optical input. All the MMIs are configured to have more than 1° phase error and 1% power imbalances. A 10 GHz RF source having peak amplitude of $v_{RF} = 0.1v_\pi$ V (m~0.44 as per (10)) and appropriate phase shift is chosen to emulate the experiment. Fig. 4 shows the simulated optical spectrum of the frequency shift operation. In the laboratory experiment, the coupling and on-chip loss is found to be 25 dB (~16 dB coupling loss and ~9 dB on-chip loss). The 9 dB on-chip loss is in agreement with the loss value (5 dB) reported in [13] considering the longer phase shifters and routing waveguides, and the presence of two additional MMI. However, the coupling loss is 4 dB higher (16 dB vs 12 dB) due to a non-optimum fiber array. Hence, a 25-dB attenuator is used in the simulated circuit to account for the coupling and on-chip loss. Note that state-of-the-art silicon photonic modulators can be designed with lower than 1 dB of coupling loss using edge couplers [15], subwavelength gratings [16], or photonic wire bonding [17].

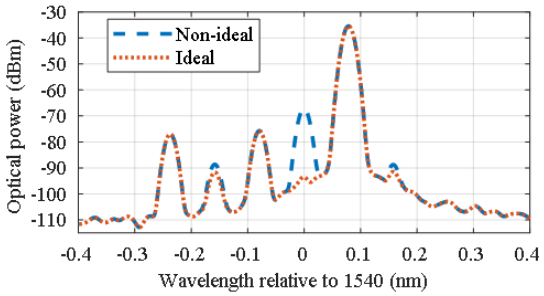

Fig. 4. Simulated optical spectrum; Ideal, refers to the exact optical phase shift between the stages and Non-ideal represent slight detuning from the ideal. The optical noise floor is determined by the laser linewidth.

The theoretical analysis of the circuit architecture is relatively straightforward; however, achieving the correct quiescent operating point experimentally is complicated by imbalance of the optical path lengths in the different stages of the test architecture and other impairments due to fabrication errors. Nevertheless, thermo-optic phase shifters are present in every stage for appropriate phase tuning. Firstly, a DC characterization was performed with the assistance of the algorithm presented by Wilkes et al [18]. Using the algorithm, the extinction ratio at the upper output port is maximized to greater than 40 dB. The lower port extinction is improved similarly. The algorithm works on the principle that the first stage MZI acts as a variable beam splitter and the last stage MZI acts as a variable beam combiner while the complete circuit acts as a single MZI controlled by the phase shifters in the central stage. The high extinction at the upper output port ensures that the complete circuit acts as an ideal MZI; when the second stage phase shifter is adjusted to maximized transmission, the optical input to the upper input port exits only from the upper output port. Following the achievement of this bias state an additional 90° optical phase bias is applied at the 1st stage and 3rd stage to achieve the correct bias state for single sideband modulation. A fine tuning of the bias voltages is required for proper operation. A laser source providing 0 dBm power at a vacuum wavelength of 1540.01 nm was used as the optical input. An Anritsu 3695C RF signal generator was used as RF signal source. A 10 GHz sinusoid having power of 18

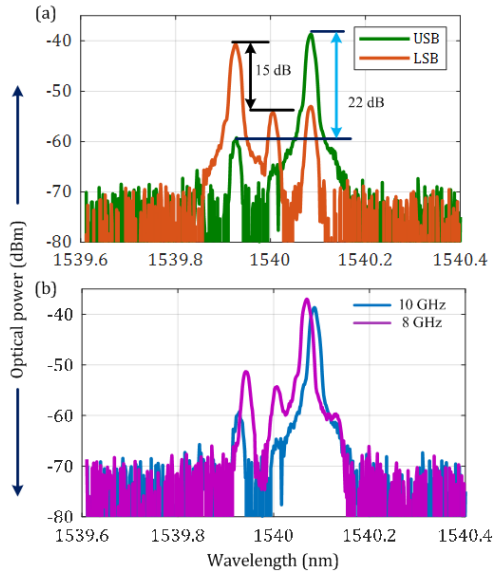

Fig. 5. Measured optical spectra for (a) upper side band (USB) and lower side band modulation (LSB); (b) upper side band modulation for two different RF frequency. A resolution bandwidth of 0.02 nm is used for measurement.

dBm was used as the analog RF input to the circuit. A 90˚ RF hybrid coupler from Krytar (model 3014320; 1.4-32 GHz) was used to create the in-phase (I) and quadrature-phase (Q) channels. The insertion loss of the hybrid is about 3.5 dB, while the amplitude imbalances and phase imbalances are ± 1.55 dB and $\pm 12^{\circ}$ respectively. A mechanical phase shifter from API technologies (OPS -0002) was used in one of the arms at the output of the hybrid coupler for fine tuning of the phase of the RF signal. The insertion loss of the device was 3-5 dB. Finally, the RF signal was applied to the RF pad of the circuit using a RF probe. The RF coaxial cable connected between the RF probe and the 90˚ hybrid added a further 2-3 dB of loss. Fig. 5 (a) shows the measured frequency down-conversion (green) from the upper output port. The bias voltages at the thermo-optic phase shifters are 5.10 V, -3.24 V and 3.20 V for the 1st stage, 2nd stage and 3rd stage respectively. The optical spectra show that a side harmonic suppression ratio of more than 20 dB can be obtained by fine tuning of the bias voltages. Frequency up-conversion (orange) is obtained from the same output port when the input optical signal is changed from upper input port to the lower input port. For the identical bias voltages, the side harmonic suppression is reduced to some extent from the previous case. The modulation index is ~ 0.35-0.40, far from the peak ($m =\sim 2$) of the first harmonics. A low v_{π} modulator can be used to improve the conversion efficiency. Fig. 5 (b) shows the output optical spectra for 10 GHz and 8 GHz RF signal. Since the chip was not wire bonded, and there is no heat sink to stabilize the temperature, slight variation in the optical spectra were observed due to thermal drift of the bias point. Nevertheless, a side harmonic suppression ratio of 15 dB or more is obtained in all cases.

CONCLUSION

In summary, the experimental verification of a previously proposed two stage cascaded circuit architecture for single side band modulation was performed. A three-stage cascaded circuit architecture fabricated for high baud rate PAM transmission was adapted for the experimental demonstration. The experimental result shows that, the circuit can perform SSB modulation with a side harmonic suppression ratio of at least 15 dB or more. Careful design and experiment are required to improve the performance further. However, it is now proven that a two-stage cascaded MZM can be used for SSB and/or I-Q or complex modulation with greater energy efficiency. The device was fabricated using CMOS compatible silicon photonics technology.

ACKNOWLEDGMENT

The authors acknowledge Dr Alexandre D. Simard for the cascaded MZM design. Device fabrication was made possible with the help of TeraXion, CMC Microsystems and NSERC through CRD project grant 438811-12.

REFERENCES

[1] M. Izutsu, S. Shikama, T. Sueta, 'Integrated optical SSB modulator / frequency shifter', 'IEEE J. Quantum Electron., vol. 17, no. 11, pp. 2225-2227, Nov. 1981.
[2] G. H. Smith, D. Novak, and Z. Ahmed, "Overcoming chromatic-dispersion effects in fiber-wireless systems incorporating external modulators," IEEE Trans. Microw. Theory Tech., vol. 45, no. 8, pp. 1410-1415, Aug. 1997.
[3] S. Shimotsu et al., Single side-band modulation performance of a LiNbO3 integrated modulator consisting of four-phase modulator waveguides," IEEE Photon. Technol. Lett., vol. 13, no. 4, pp. 364-366, Apr. 2001.
[4] J. Yu, Z. Jia, L. Yi, Y. Su, G.-K. Chang, and T. Wang, "Optical millimeter-wave generation or up-conversion using external modulators," IEEE Photon. Technol. Lett., vol.18, no. 1, pp.265-267, Jan. 2006.
[5] C. W. Chow, C. H. Wang, C. H. Yeh, and S. Chi, "Analysis of the carrier-suppressed single-sideband modulators used to mitigate Rayleigh backscattering in carrier-distributed PON" Opt. Express, vol. 19, no. 11, pp. 10973-10978, May 2011.
[6] J.-G. Zhao, Z. J. Liu, X.-L. Liu, T. Shang, and P. Yue, "Optimisation of carrier-to-sideband ratio by triple-arm Mach-Zehnder modulators in radio-over-fibre links," IET Optoelectron., vol. 4, no. 5, 183-188, Oct. 2010.
[7] M. Hasan, R. Maldonado-Basilio, and T. J. Hall, "A dual-function photonic integrated circuit for frequency octo-tupling or single-side-band modulation" Opt. Lett., vol. 40, no. 11, pp. 2501-2504, May 2015.
[8] R. Maldonado-Basilio et al., Electro optic up-conversion mixer amenable to photonic integration," J. Mod. Opt., vol. 62, no. 17, pp.1405-1411, May 2015.
[9] Kodigala et al., Silicon Photonic Single-Sideband Generation with Dual-Parallel Mach-Zehnder Modulators," in Proc. CLEO, San Jose, CA, USA, 2019.
[10] M. Hasan, T. J. Hall, "A photonic frequency octo-tupler with reduced RF drive power and extended spurious sideband suppression," Opt. Laser Technol., vol. 81, pp. 115-121, Jul. 2016.
[11] M. Hasan and T. Hall, "Cascade photonic integrated circuit architecture for electro-optic in-phase quadrature/single sideband modulation or frequency conversion," Opt. Lett., vol. 40, no. 21, pp. 5038-5041, Sep. 2015.
[12] M. Hasan and T. Hall, "Complex modulation using tandem polarization modulators," J. M. Opt., vol.64, no. 20, pp. 2268-2272, Jun 2017.
[13] A. Simard, B. Filion, D. Patel, D. Plant, and S. LaRochelle, "Segmented silicon MZM for PAM-8 transmissions at 114 Gb/s with binary signaling," Opt. Express, vol. 24, no. 17, pp. 19467-19472, Aug. 2016.
[14] A. Simard and S. LaRochelle, "Complex apodized Bragg grating filters without circulators in silicon-on-insulator," Opt. Express, vol. 23, no. 13, pp. 16662-16675, Jun. 2015.

[15] T. Tsuchizawa et al., Microphotonics devices based on silicon microfabrication technology," IEEE J. Sel. Top. Quantum Electron., vol. 11, no. 1, pp. 232-240, Feb. 2005.
[16] P. Cheben et al., Refractive index engineering with subwavelength gratings for efficient microphotonic couplers and planar waveguide multiplexers," Opt. Lett., vol. 35, no. 15, pp. 2526-2528, Jul. 2010.
[17] N. Lindenmann et al., Photonic wire bonding: a novel concept for chip-scale interconnects," Opt. Express, vol. 20, no. 16, pp. 17667-17677, Jul. 2012.
[18] C. Wilkes et al.,60 dB high-extinction auto-configured Mach–Zehnder interferometer," Opt. Lett., vol. 41, no. 22, pp. 5318-5321, Nov. 2016.

Complex Modulation using tandem Polarization Modulators

Mehedi Hasan[1*], and Trevor Hall[1]

[1]Photonic Technology Laboratory, University of Ottawa, 800 King Edward Avenue, Ottawa, K1N 6N5, ON, Canada

***Abstract*— A novel photonic technique for implementing frequency up-conversion or complex modulation is proposed. The proposed circuit consists of a sandwich of a quarter-wave plate between two polarization modulators, driven respectively by an in-phase and quadrature-phase signals. The operation of the circuit is modeled using a transmission matrix method. The theoretical prediction is then validated by simulation using an industry-standard software tool. The intrinsic conversion efficiency of the architecture is improved by 6 dB over a functionally equivalent design based on dual parallel Mach-Zehnder modulators. Non-ideal scenarios such as imperfect alignment of the optical components and power imbalances and phase errors in the electric drive signals are also analyzed. As light travels, along one physical path, the proposed design can be implemented using discrete components with greater control of relative optical path length differences. The circuit can further be integrated in any material platform that offers electro-optic polarization modulators.**

I. INTRODUCTION

Frequency up-conversion or single side-band (SSB) modulation in the uplink is one of the key functions required by a radio-over-fiber (RoF) link. The generation of SSB and complex (in-phase (I) and quadrature (Q)) modulation using single and multiple Mach-Zehnder modulator (MZM) has been extensively investigated previously [1-7]. Hitherto a circuit architecture using a dual parallel Mach-Zehnder (DP-MZM) modulator has proved to be the most suited to practical implementation [7] but requires the control of three large bias voltages to prevent drifts. This issue may be alleviated by making good use of the intrinsic phase relations between the output ports of multimode interference (MMI) couplers used to form the MZM to eliminate the requirement large DC bias, at least in principle [8-9]. All the architectures reported in [1-9] are equivalent to the same generalized Mach-Zehnder Interferometer (GMZI) where a parallel array of N linear electro-optic phase modulators interconnect a $1 \times N$ splitter at the front and $N \times 1$ combiner at the rear. Motivated by the authors' finding [10] that a cascade MZM architecture for frequency multiplication required 3 dB less in radio frequency (RF) power than its functionally equivalent parallel architecture, it was shown for the first time that an unorthodox series arrangement of two MZM can provide the same function (SSB, I-Q modulation) as the parallel arrangement of two MZM within a DP-MZM, with a 6-dB advantage in intrinsic conversion efficiency [11]. The demonstration of an optical single side band polarization modulation (unsuppressed carrier) with high sideband suppression ratio (30 dB) using two cascaded polarization modulators as presented in [12], motivates the authors to design an I-Q modulator using cascaded polarization modulator. In this paper, a design based on similar principles [11] is proposed using polarization optics.

The fundamental operating principle of a polarization modulator is two-mode interference. The two-modes are a pair of eigenmodes with orthogonal polarization aligned along the principal axes of the electro-optic modulator. The two modes may both be excited using a polarizer to present linearly polarized light at the input inclined at an angle to the principal axes; both modes are equally excited if this angle is set to 45°. In the typical case, a field-applied to the using a polarization analyzer oriented at an angle to the principal axes of electro-optic material induces a differential phase-shift between these two modes, which may be brought to interference using an analyzer inclined at an angle to the principal axes. The contrast of the interference is maximized if this angle is set to 45°. The polarization modulator may be equipped with a pair of complementary input and output ports by using polarizing beam splitters to implement the polarizer and analyzer, which combined with appropriately oriented half-wave and quarter-wave plates, function as variable beam-splitters. As a two-mode interferometer a polarization modulator is functionally equivalent to any other two-mode interferometer such as a conventional Mach-Zehnder interferometer in which the two modes are distinct spatially. Nevertheless, the polarization modulator offers some technical advantages. For most applications a conventional MZI is only practical when implemented on a suitable integration platform because of its sensitivity to path-length errors between its arms. A polarization modulator is far more robust to such errors because the two-modes

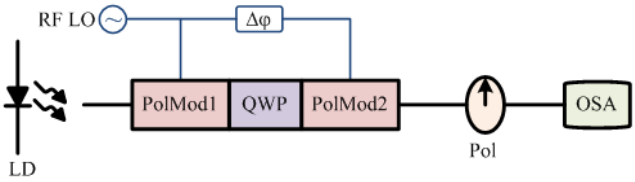

Fig. 1. Schematic diagram of the proposed frequency up-converter. LD: laser diode; PolMod1: polarization modulator 1; QWP: quarter wave plate; PolMod2: polarization modulator 2; Pol: polarizer; OSA: optical spectrum analyzer. RF LO: radio frequency local oscillator.

overlap spatially and follow an identical physical path which cancels the common part of path-length errors. The control of relative optical path-length differences between the modes is eased sufficiently that an implementation using discrete components is practical. Moreover, the implementation of static optical phase phases is also eased considerably. The use of polarizing beam splitters permits beam-splitting ratios corresponding to sums or differences and commonly used static optical phase biases may be implemented by insertion of a suitably orientated half- or quarter-wave plate.

In [11], it was shown for the first time that I-Q modulation using cascaded MZM, can be achieved using an unorthodox inter-stage coupler with specific phase relations between its ports. The novelty of the design lies in making use of both output ports of the first-stage MZM and both input ports of the second MZM rather than the usual practice of leaving one output port and one input port unused. A 2×2 MMI is used as a combined exit-coupler of first stage MZM and entrance-coupler of the second stage MZM, thus forming a special coupling and optical bias element for the MZM. In [12], an inter-stage polarization controller is used, effectively, as an appropriately oriented half-wave plate to rotate the output of the first polarization modulator by 45° to obtain single side band modulation with *unsuppressed* carrier. However, in order to obtain I-Q modulation or single side band modulation with a *suppressed* carrier with a cascade of polarization modulators, the inter-stage coupler must be functionally equivalent to the special coupling element described in reference [11]. It turns out that the equivalent element is an appropriately oriented quarter-wave plate.

The proposed architecture is a sandwich of two electro-optic polarization modulators with a quarter wave plate between them as illustrated schematically in Figure 1. The axes of the polarization modulators are aligned with the x and y axes. The light entering the device is linearly polarized at 45 degrees to the x and y axes. The polarizer is crossed with respect to the input polarization in order to form the difference between the x and y components of the polarization. An innovative part of the design is the use of a quarter-wave plate with its axes oriented at 45 degrees to the x & y axes to mix the x- & y- components of the polarization between the two polarization modulators. Since the quarter-wave plate is notionally lossless the insertion loss of the overall device is reduced by 3 dB in comparison to the orthodox methods of I-Q modulation. To the best of the author's knowledge, the resulting architecture has not been reported previously.

For simplicity, assume there is no transmission delay between the stages. Consider a pair of polarization modulators with principal axes aligned with the x and y direction. Then in x and y co-ordinate system their Jones matrices are given by

$$T_{EOM} = \begin{bmatrix} \exp(i\varphi) & 0 \\ 0 & \exp(-i\varphi) \end{bmatrix} \tag{1}$$

where, $\varphi = \pi v(t)/v_{\pi}$ is the optical phase shift induced by RF signal, $v(t)$ and v_{π} is the half-wave voltage of the modulator. The Jones matrix of a wave plate with fast axis vertical (y) and slow axis horizontal (x) with retardant $\alpha = \pi/2$ for quarter wave plate,

$$T_{wp} = \begin{bmatrix} \exp(i\alpha/2) & 0 \\ 0 & \exp(-i\alpha/2)) \end{bmatrix} \tag{2}$$

If one rotates the wave plate so the slow axis is inclined at an angle θ to the horizontal (when looked at in the direction of beam propagation) then the Jones matrix becomes:

$$T_{wp} = \begin{bmatrix} \cos(\alpha/2) + i\sin(\alpha/2)\cos(2\theta) & i\sin(\alpha/2)\sin(2\theta) \\ i\sin(\alpha/2)\sin(2\theta) & \cos(\alpha/2) - i\sin(\alpha/2)\cos(2\theta) \end{bmatrix} \tag{3}$$

If $\theta = 45^{\circ}$, then the transfer matrix of a quarter wave plate with respect to the x and y axis is given by:

$$T_{wp} = \frac{1}{\sqrt{2}} \begin{bmatrix} 1 & i \\ i & 1 \end{bmatrix} \tag{4}$$

The input is linearly polarized inclined at 45° to the x and y axis and hence:

$$E_{in} = \frac{1}{\sqrt{2}}\begin{bmatrix}1\\1\end{bmatrix} a_{in} \tag{5}$$

The output is selected by a polarizer crossed with the input polarization; hence the output of the whole circuit can be written as:

$$E_{out} = \frac{1}{\sqrt{2}}[1 \quad -1] T_{EOM1} T_{wp} T_{EOM2} \frac{1}{\sqrt{2}}\begin{bmatrix}1\\1\end{bmatrix} a_{in} \tag{6}$$

Carrying out the matrix multiplications results in:

$$E_{out} = \frac{1}{\sqrt{2}}[i \sin(\varphi_1 + \varphi_2) + \sin(\varphi_1 - \varphi_2)] a_{in} \tag{7}$$

If one sets $v_1 = v_I$ and $v_2 = v_Q$, then for $|v_I|, |v_Q| \ll v_\pi$ one finds:

$$E_{out} = \frac{\pi}{v_\pi}\left(v_I + i v_Q\right) \exp(i\,\pi/4)\, a_{in} \tag{8}$$

which demonstrates in the small signal approximation that the circuit acts as an I-Q modulator up to a rotation of the constellation. In the case of narrow-band RF modulation then

$$\begin{aligned} v_1(t) &= v_{RF} \cos(\omega t) \\ v_2(t) &= v_{RF} \sin(\omega t) \end{aligned} \tag{9}$$

and, invoking the Jacobi-Anger expansion, Eq. (7) may be rewritten as:

$$E_{out} = \sqrt{2} \sum_{n=0}^{\infty} (-1)^n J_{2n+1}(m) exp[(-1)^n (2n+1)\omega t]\, a_{in} \tag{10}$$

where

$$m = \sqrt{2}\pi \frac{v_{RF}}{v_\pi} \tag{11}$$

is the modulation index and, J_{2n+1} is the Bessel function of the first kind of order $2n+1$. It can be seen from Eq. (10), that the orders of the principal side-bands are -3, 1 and 5. The $\sqrt{2}$ pre-factors in Eq. (10) & (11) yield the 3-dB optical and 3 dB electrical enhancement of conversion efficiency of the proposed design over the circuits presented in the prior art [1-9].

II. Simulation Results

A VPI software simulation is used to verify the operation of the proposed design. A continuous wave distributed feedback (DFB) laser with a wavelength of 1550 nm and power of 10 mW is used as the optical input. The input light is linearly polarized at an angle of 45° to one of the principal axes. A 20 GHz sinusoidal drive signal having amplitude of 0.1V ($v_\pi = 1$V) is applied to each modulator with the proper phase relation as specified in the earlier section. A SSB modulation is obtained at the output port as shown in Fig 2(a). It shows that an optical sub-harmonics suppression ratio (SHSR) of near about 42 dB can be achieved in ideal conditions, i.e. when the power splitting ratio of the RF drive signals are 50:50 and in quadrature phase. In practice, path imbalances in the electrical waveguides that connect the drive signals to the phase modulators will occur and minimizing this imbalance is the most critical aspect of the design [13]. Figure 2(b) shows the simulated optical SHSR for a $\pm 4^{\circ}$ phase error between the in-phase and quadrature RF drive signals. Simulation result shows that a SHSR of 30 dB still can be achieved for 4° of phase error. The suppression ratio (30 dB) of the proposed scheme is much larger than the functionally equivalent configuration found in [14] using a dual parallel MZM (the SHSR is about 22~23 dB).

Furthermore, as the output is selected by a polarizer; a fine tuning of the polarizer angle around 45° can improve the SHSR by another 2~3 dB or more. The inset shows the corresponding optical spectrum. It shows that still there is no carrier breakthrough. In [1-9] and all other functionally equivalent designs known in prior art, a residual carrier is always present because of the finite extinction ratio of the MZM. As the proposed design uses only one physical path along which light travels, the carrier breakthrough will only occur if there is an error in the orientation of the

components.

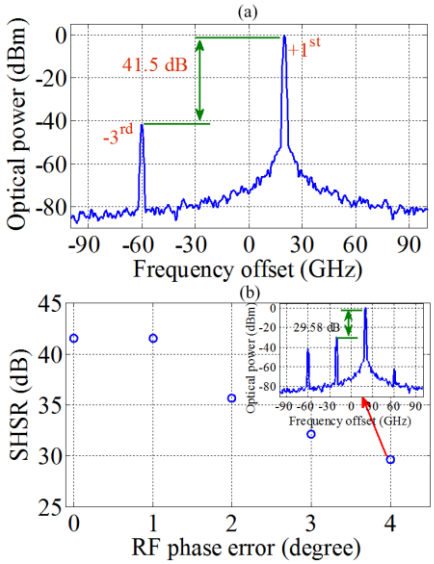

Fig. 2. (a) Simulated optical spectrum; (b) impact of RF drive phase error on SHSR. A resolution bandwidth of 1 GHz is used for the optical spectrum analyzer.

To assess the impact of the incorrect alignment of the components, a further investigation is carried out. First of all, a 3° phase error and 5% power imbalance is created between the I and Q drive. The peak amplitude of the RF drive signal is set to 0.2V to ensure that the circuit operates in the linear region or nearby. Then the orientation of the wave plate (with respect to the ideal 45°) is varied and the peak optical power of the harmonics of interest and unwanted harmonics are plotted in Fig 3. It shows that the carrier breakthrough is dominant only when the orientation error is $\pm 2^{\circ}$ and above. The SHSR remains close to 25 dB. However, the carrier breakthrough can be reduced significantly (20-30 dB) by adjusting the polarization of the input light wave slightly; which ensured a SHSR of 30 dB or more. Fig 4 shows the simulated optical spectrum for a $\pm 2^{\circ}$ error in the alignment of the quarter wave plate with the drive signals errors specified in the preceding. Table I gives the combination of the polarizer angle and input light wave polarization to obtain the spectrum presented in Fig 4. The table shows that when PA and LPA both are set to ideal values (a), the signal of interest (+1 harmonic) is about 22.5 dB stronger than the carrier (Fig 4(a)). A further tuning in either PA or LPA improve the suppression ratio by a further 3 dB, making the overall suppression near 25.5 dB (Fig 4 (b)). A fine tuning in both PA and LPA suppresses the carrier further, making the signal to carrier suppression ratio reach 55 dB or more. In addition, the suppression ratio with respect to the strongest harmonics (-1) is about 30

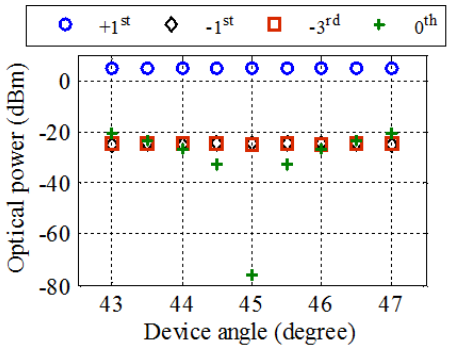

Fig. 3. Optical power of the harmonics of interest ($+1^{st}$) and unwanted harmonics for a range of device (quarter wave plate) angle selection.

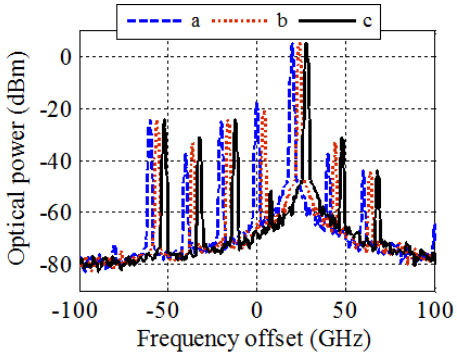

Fig. 4. Simulated Optical spectrum for different settings of the polarizer angle and the angle of input polarization. Plots "b" and "c" have been frequency shifted by 4 GHz and 8 GHz respectively.

dB and it can be filtered out easily if required. As the proposed circuit offers two degrees of freedom (tuning of the polarizer angle and polarization of the input light wave) over the convectional integrated circuit, a fine tuning of the orientation of the components can suppress the residual carrier significantly and improve overall performance.

Table 1. Different settings of the polarizer angle (PA) and input Laser's polarization angle (LPA) to address the alignment error among the principle components

Spectrum (Figure 4)	Polarization angle (degree)	Polarization angle of the input light wave (degree)
a	45˚	-45˚
b	45˚	-47˚
c	43˚	-47˚

III. CONCLUSION

In summary, a photonic circuit architecture capable of implementing frequency up-conversion is proposed and verified by simulation. The circuit can also be used as an I and Q modulator. The proposed design is advantageous by 6 dB in terms of conversion efficiency compared to the functionally equivalent single stage parallel circuit. Residual carrier and other sub-harmonic suppression ratios are improved as light travels along only one physical path. The proposed architecture can easily be implemented using discrete components. Moreover, developments in high speed polarization modulators and improved photonic integration technology [15] provide prospects of photonic integrated circuit implementation.

ACKNOWLEDGMENT

Mehedi Hasan is grateful to Vanier Canada Graduate Scholarship program for their financial support. The authors acknowledge the Natural Sciences and Engineering Research Council of Canada (NSERC) for their support through a Strategic Project Grant.

REFERENCES

1. M. Izutsu, S. Shikama, T. Sueta, "Integrated optical SSB modulator / frequency shifter," *IEEE J. Quantum. Electron*. Vol. 17, no. 11, pp. 2225-2227, Nov. 1981.
2. A. Caballero, D. Zibar, R. Sambaraju, J. Marti, I. T. Monroy, "High-capacity 60 GHz and 75-110 GHz band links employing all-optical OFDM generation and digital coherent detection," Journal of Lightwave Technol. Vol. 30, no. 1, pp. 147-155, Jan. 2012.
3. G. H. Smith, D. Novak, and Z. Ahmed, "Overcoming chromatic-dispersion effects in fiber-wireless systems incorporating external modulators," IEEE Trans. Microw. Theory Techn. Vol. 45, no. 8, pp. 1410-1415, Aug. 1997.
4. G. H. Smith, D. Novak, and Z. Ahmed, "Technique for optical SSB generation to overcome dispersion penalties in fibre-radio systems," Electron. Lett. Vol. 33, no. 1, 74-75, Jan. 1997.
5. J. Yu, Z. Jia, L. Yi, Y. Su, G.-K. Chang, and T. Wang, "Optical millimeter-wave generation or up-conversion using external modulators," IEEE Photon. Technol. Lett. Vol. 18, no. 1, pp. 265-267, Jan. 2006.
6. A. Wen, M. Li, L. Shang, and Y. Chen, "A novel optical SSB modulation scheme with interfering harmonics suppressed for ROF transmission link," Opt. & Laser Technol. Vol. 43, no. 7, pp. 1061-1064, Oct. (2011).

7. C. W. Chow, C. H. Wang, C. H. Yeh, and S. Chi, "Analysis of the carrier-suppressed single-sideband modulators used to mitigate Rayleigh backscattering in carrier-distributed PON" Opt. Express Vol. 19, no. 11, pp. 10973-10978, May 2011.
8. M. Hasan, R. Maldonado-Basilio, and T. J. Hall, "A dual-function photonic integrated circuit for frequency octo-tupling or single-side-band modulation" Opt. Lett. Vol 40, no. 11, pp. 2501-2504, Dec. (2015).
9. R. Maldonado-Basilio, M. Hasan, H, Nikkah, S. Abdul-Majid, R. Guemri, F. Lucarz, J. Tocnaye, and T. J. Hall, "Electro optic up-conversion mixer amenable to photonic integration," J. of Mod. Opt. Vol 62, no. 17, pp. 1405-1411, 2015.
10. M. Hasan and T. J. Hall, "A photonic frequency octo-tupler with reduced RF drive power and extended spurious sideband suppression," Opt. Laser Technol. Vol. 81, pp. 115-121, Jan. 2016.
11. M. Hasan, and T. J. Hall, "Cascade photonic integrated circuit architecture for electro-optic in-phase quadrature/single sideband modulation or frequency conversion," Opt. Lett. Vol. 40, no. 21, pp. 5038-5041, Nov. 2015.
12. Y. Zhang, F. Zhang, and S. Pan, "Optical single sideband polarization modulation for radio-over-fiber system and microwave photonic signal processing" Photon. Res. Vol. 2, no. 4, pp. B80-B85, Aug. 2014.
13. M. Hasan, R. Guemri, R. Maldonado-Basilio, F. Lucarz, J-L de Bougrenet and T. J. Hall, "Photonic integrated circuit for frequency 8- and 24-tupled millimeter wave signal generation", Opt. Lett. Vol. 39, no. 24, pp. 6950-6953, Dec. 2014.
14. H. Yamazaki, T. Saida, T. Goh, A. Mori, and S. Mino, "Dual-carrier IQ modulator with a complementary frequency shifter," Opt. Express Vol. 19, no. 26, pp. B69-B74, Dec. 2011.
15. D. Marpaung, C. Roeloffzen, R. Heideman, A. Leinse, S. Sales, and J. Capmany, "Integrated microwave photonics", Laser Photonics Rev. Vol. 7, no. 4, pp. 506-538, Jan. 2013.

CHAPTER 5

Photonic generation of broadband RF phase shift

5.1 Summary

In this chapter, a broadband RF-photonic vector (IQ) modulator / phase shifter is described. The proposed circuit architecture is based on two parallel DP-MZM circuit that requires no additional control or filter for proper operation. Furthermore, the linearity of the phase shifter remains valid for a wide range of frequencies. The proposed phase shifter can generate any phase without bound. The complex transmission of the modulator may follow a trajectory that may encircle the origin of the complex plane an arbitrary number of times in either direction. A simulation verification is provided using industry standard software tool. An equivalent experimental demonstration is also provided at low frequencies using in-house off the shelf electronics.

5.2 Contribution

The results demonstrated in this chapter is submitted as article for publication in *Optics Express*. The idea was conceived by I and Dr. Hall equally. I performed the numerical simulation along with the manuscript writing. I completed the experimental setup and measurements. Dr. Hall contributed to the interpretation of the results, revised the manuscript, and provided guidance on the experimental setup.

5.3 Article

The published or submitted article follows verbatim

Photonic generation of broadband RF phase shift with unbounded phase trajectory

MEHEDI HASAN,[1,*] AND TREVOR HALL,[1]

[1]Photonic Technology Laboratory, Centre for Research in Photonics, Advanced Research Complex, University of Ottawa, 25 Templeton Street, Ottawa, K1N 6N5, ON, Canada

Abstract: A means of applying an adjustable RF phase shift over a broad band of frequencies is a requirement of diverse application. Photonic solutions to the generation of RF phase shifts have receive significant attention for reasons of reduced cost, compactness and simplicity, yet the achievement of a phase shift extending beyond 360˚ range remains a challenge. The circuit architecture of a compact and broadband RF phase shifter with unbounded range based on two parallel DP-MZM architecture is presented and verified by simulation verification and emulated using off the shelf low frequency electronic components. Results demonstrate that the complex transmission of the phase shifter follows a trajectory that may r encircle the origin an arbitrary number of times in either direction. The proposed architecture can be implemented using commercially available DP-QPSK modulator or can be integrated in any material platform that offers linear electro-optic phase modulators.

1. Introduction

A precise and broadband radio frequency (RF) phase shifter is needed in a variety of applications including phased array antenna systems to support high speed wireless communication and radar; and self interference cancellation (SIC) systems in a full duplex technology to improve the attainable spectral efficiency of a 5G network. The photonic generation of microwave phase shifts is receiving significant attention due to its simplicity, light weight, low cost, small size and broadband operation with minimal phase errors. The underlying principle is based on frequency shifting an optical carrier via single side band suppressed carrier (SSB-SC) modulation using RF carrier of interest followed by the re-insertion of a copy of the original optical carrier that is shifted in phase by a variety of means such as an optical phase modulator based on p-n junction devices; z-cut lithium niobate (LiNbO3); or a polarization controller within a number of different circuit architectures [1-8].

In reference [1] an optical carrier is divided in to two paths, one used to generate SSB-SC modulation, while the other path is phase shifted using an optical phase modulator. Both the paths are then combined on a photodiode to generate the phase shifted RF signal. A similar strategy to obtain the phase shift is followed in references [2,3] using a dual-polarization dual-parallel Mach Zehnder Modulator (DP-MZM); in which one DP-MZM generates the SSB-SC modulation while the other DP-MZM is biased at maximum transmission point to maximize the output power of the carrier. The outputs of the both DP-MZM are then combined using a polarization beam combiner (PBC). The relative phase of the orthogonally polarised optical carrier and sideband is then adjusted by a polarization dependent optical phase shifter (OPS) [2] or a combination of polarization controller and polarizer [3]. A DP-MZM based scheme is presented in [4-7]. In [4], one child MZM is biased at the minimum transmission point (MITP) and driven by an RF signal, thereby generating double sideband suppress carrier (DSB-SC) modulation; while the other child MZM is biased at the MATP to pass the carrier. The two outputs are combined by using an optical coupler [5]. The optical phase shift is applied by tuning the phase adjust voltage of the parent MZM. Finally, an optical bandpass filter (OBF) is used to suppress one of the sidebands. A similar method is described in [5] except the combining is done through a PBC and the optical phase shift is implemented using polarization dependent OPS. Reference [6] describes a DP-MZM based scheme capable of a 360˚-degree phase shift founded on the precise settings of the phase and amplitude of the optical carrier and two sidebands using predetermined modulator bias voltages. An architecture consisting of, two parallel MZM driven by in-phase and quadrature phase RF signal modulate orthogonally polarised optical carriers combined on a photodiode is demonstrated in [7]. The slope about the operating point of the two MZM is varied by adjustment of their respective DC bias voltage, thereby the sign and magnitude of the in-phase and quadrature phase modulation components is adjusted resulting in the phase shift of the superimposed components. For proper operation of the scheme, the modulation depth should be small which leads to high insertion loss and careful adjustment of the two bias voltages is required as, for a constant magnitude RF output, both bias voltages depend on the desired phase shift. A photonic integrated phase shifter based on silicon-on-insulator technology is presented in [8]. A single side band (SSB) full carrier modulation is generated using a DP-MZM. An optical deinterleaver filter is used to separate

the optical carrier and the sideband. The phase of the isolated carrier is then shifted by using a p-n junction based optical phase shifter and combined with the sideband on a photodiode. All these methods require either an optical deinterleaver filter or optical bandpass filter, precise control of the polarization and/or polarizer, bias voltages or suffers from lack of phase shift linearity and range. Moreover, the need for a *continuous* phase shift range extending beyond 360˚ degree is gaining appreciation. For an example, improved robustness to loss of lock of an optoelectronic oscillator has been demonstrated by enlarging the RF tuning phase shift ranges from 350˚ degrees to 1160˚ degree using a frequency conversion pair [9].

In this chapter, a circuit architecture is proposed based on a parallel pair of dual-parallel Mach-Zehnder modulators (DP-MZM) that requires no additional control or filter for proper operation. Furthermore, the linearity of the phase shifter remains valid for a wide range of frequencies. The proposed phase shifter can generate any phase without bound. The complex transmission of the phase shifter follows a trajectory in the complex plane that may encircle the origin an arbitrary number of times in either direction. The practical implementation of the proposed design can be demonstrated using a commercially available dual polarization quadrature phase shift keying (DP-QPSK) modulator. Due to unavailability of a-QPSK modulator, experimental verification by an electronic emulation of the proposed concept is presented using off the shelf components.

2. Principal of operation

The circuit diagram of the proposed braodband phase shifter is given in fig. 1. The circuit consists of two DP-MZM. The upper DP-MZM generates the suppressed carrier-single side band modulation of the applied RF drive signal. To obtain this function, the bias of the two parallel child MZM is set to their minmum tranmission points (MITP), while the mother MZM is set to its quadrature transmission point (QTP). Then the in-phase (I) and quadrature-phase (Q) of the RF drive signal is applied to the upper and lower child MZM respectively [10]. SSB-SC modulation can also be regarded as the shifting of the optical carrier frequency by an amount equal to the RF frequency. The bias of the lower DP-MZM is set similarly to the upper DP-MZM. A static or low frequency in-phase and quadrature-phase signal is applied to the two child MZM to shift the phase of the optical carrier. When the output of the two DP-MZM imping on a photodiode, a phase shifted version of the RF drive signal is recovered.

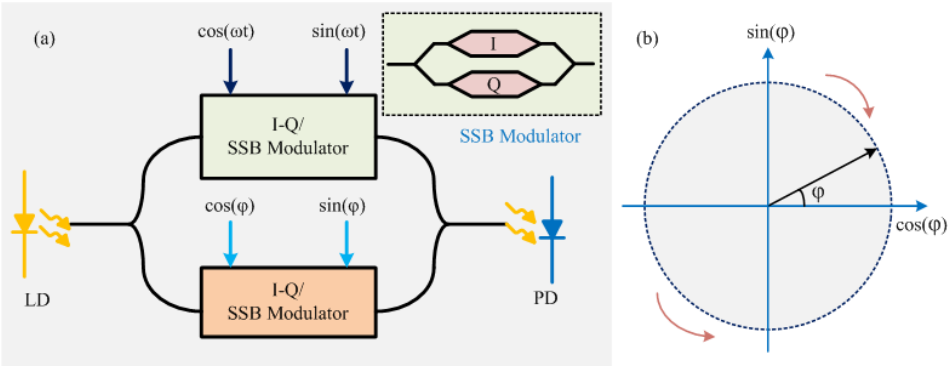

Fig. 1. (a) Schematic diagram of the proposed broadband phase shifter; (b) phase shift trajectory (either clockwise or anti-clockwise); LD, Laser diode; SSB, Single side band; PD, Photodiode.

In the small modulation index (m_1) approximation, the transmission [10] of the upper DP-MZM is

$$T_{upper\ DP-MZM} = (1/4)\, m_1 \exp\big(i(\omega_c \pm \omega_{rf})t\big) \tag{1}$$

where, ω_c and ω_{rf} is the optical and RF carrier frequency. Depending on the phase lead-lag between upper MZM and lower MZM, either an upper SSB-SC or lower SSB-SC modulation is obtained. Alternatively, one output port generates either upper/lower SSB-SC modulation while the other output port generates the complementary SSB-SC modulation for a two-output port DP-MZM [11]. The modulation index m_1 is defined by:

$$m_1 = \pi v_{RF}/v_\pi \tag{2}$$

where, v_{RF} is the amplitude of the applied RF signal and v_π is the half-wave voltage of the phase modulator used to form the MZM. Similar way, the output transmission of the lower DP-MZM can be written:

$$T_{Lower\ DP-MZM} = (1/4)\, m_2 \exp\big(i(\omega_c t \pm \varphi)\big) \tag{3}$$

where φ is the applied phase shift to the optical carrier through I-Q modulation at the lower DP-MZM. The modulation index m_2 can be written as:

$$m_2 = \pi v_p / v_\pi \qquad \text{where} \qquad v_p = \sqrt{v_I^2 + v_Q^2}$$

The v_π here may be different than for m_1 due to the difference in the frequency of the RF modulation and the IQ controls. The output of the upper DP-MZM and lower DP-MZM is combined and impinged to a photodiode. Finally, the beat signal of interest at the output of the photodiode is,

$$\propto \cos\big(\omega_{rf} t \mp \varphi\big) \tag{4}$$

The phase shift φ of the RF signal given by Eq. (4) may be continuously varied by a continuous variation of the bounded I and Q bias at the lower DP-MZM. The small modulation index m_1 is a non-necessary condition. Jacobi Anger expansion leads to same solution while providing details on the amplitude of the Bessel sidebands [12].

Rather than applying the IQ RF and IQ bias separately to a parallel pair of IQ modulators, the vector sum of the IQ RF drive and IQ bias may be applied to a single IQ modulator to obtain the same result to the extent that an IQ modulator has a transmission is linear with respect to the IQ vector. Consequently, a single DP-MZM can be used to perform a similar operation [13]. However, without special linearization [14] measures the single DP-MZM arrangement is limited to small modulation indices m_1, m_2 resulting in high insertion loss compared to the parallel DP-MZM solution.

3. Simulation verification & experimental result

Circuit simulation using VPIphotonics is performed to verify the theoretical prediction. A Distributed Feedback (DFB) laser having wavelength of 1550 nm and an output power of 10 dBm is used as the optical source. The insertion loss and extinction ratio of each MZM is set to be 4 dB and 30 dB respectively. The half-wave voltage of each MZM is set to 5 V. The in-phase and quadrature phase of the RF drive signal with peak amplitude of 1.2 V and a frequency of 10 GHz is applied to the upper DP-MZM. This results in a frequency shift of the optical carrier by an amount of 10 GHz. Although suppressed-carrier modulation is desired, the suppression is not complete due to the finite extinction of the MZM. For the purpose of demonstrating the operating principle by simulation, a very low frequency cosine- and sine-waveform are applied to the in-phase and quadrature-phase inputs to the lower DP-MZM to generate a slow linear ramp of the optical carrier phase. Once both the output of the upper and lower DP-MZM are combined at the photodiode, the desired phase shifted RF carrier can be observed.

Figure 2 shows the phase shift at different static phase (φ) of the low frequency drive signal predicted by the simulation. The output phase shift exactly matches the applied phase shift and without bound. The corresponding phasor can rotate about the origin of the complex plane in either direction (clockwise or anti-clockwise) an arbitrary number of times. The power variation of the recovered signal at different phase shifts is found to be ∼1.8 dB maximum. This variation is the result of the nonlinear transmission function of the DP-MZM and may be corrected by pre-

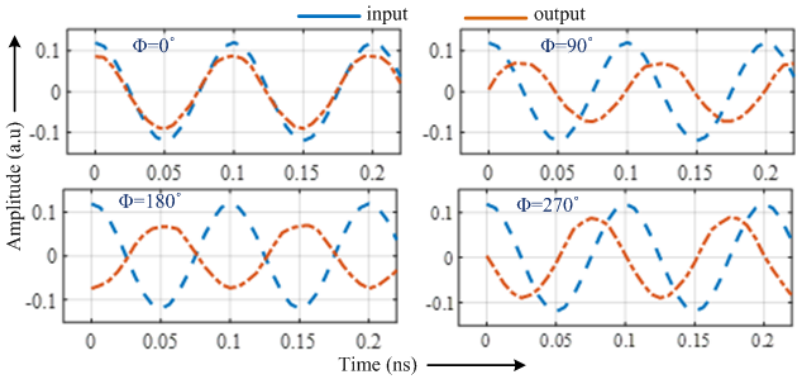

Fig. 2. Simulated phase relationship between the input and output RF signal.

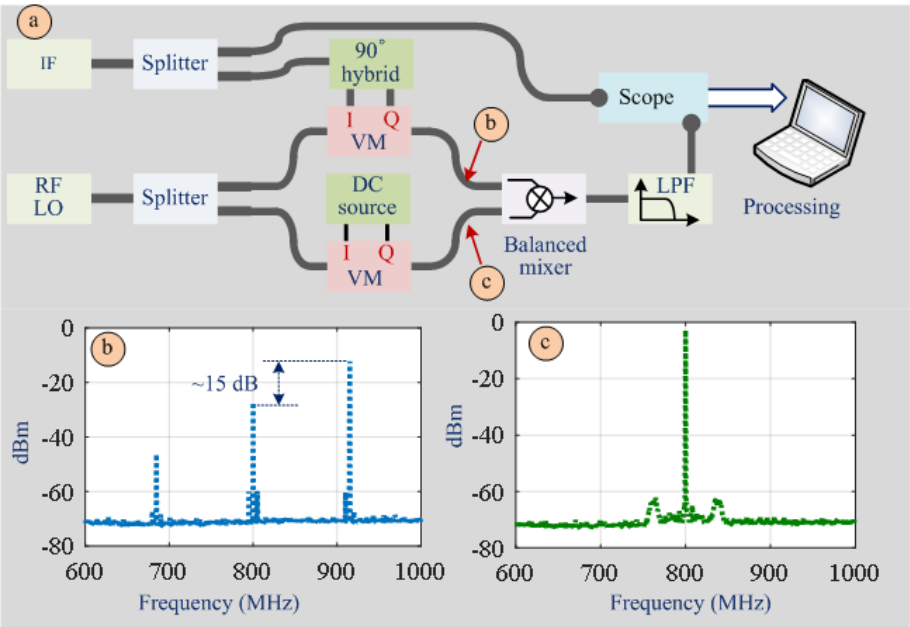

Fig. 3. (a) Schematic of the experimental setup; (b) and (c) are the measured spectra (electrical) of the signal at point (b) and (c) in schematic (a); IF, intermediate frequency; LO, local oscillator; VM, vector modulator; DC, direct current. An electrical resolution bandwidth of 1 kHz with is used to capture the data.

distortion of the in-phase and quadrature phase controls of the lower DP-MZM or by application of alternative methods [14] of the lower DP-MZM. The proposed circuit can be used up to the bandwidth of the phase modulators used to form the DP-MZM. The practical implementation of the proposed circuit can be realized by commercially available dual polarization quadrature phase shift keying (DP-QPSK) modulator. Hybrid integration of silica and modulator based on LiNbO3 can be used to verify the concept [15].

Due to unavailability of a DP-QPSK-modulator and vector network analyzer, the concept is verified experimentally using off the shelf lower frequency electronic components. Figure 3 shows the schematic diagram of the experimental setup. An Analog Devices HMC630 used as vector modulator to emulate the function of a DP-MZM. The vector modulator has one input port, one output port and two other input ports for the application of I and Q controls. The operating frequency range is 700-1000 MHz, whereas the 3dB bandwidth of the I and Q ports are 180 MHz. A Minicircuits ADP-2-10W (5 to 1000 MHz) is used as the input power splitter. To emulate the function of a photodiode, a double balanced mixer (ADE-2+) from Minicircuits is used. A RF signal with a frequency of 800 MHz and 10.5 dBm output power is used as the input carrier. A Rohde & Schwarz SMB 100A signal generator is used as the RF LO. An IF signal having frequency of 115 MHz is applied to a 90˚ hybrid (Minicircuits ADQ-22+) to generate the in-phase and quadrature-phase components. The in-phase and quadrature-phase component is then applied to the I and Q ports respectively of the upper vector modulator.

Figure 3(b) shows the measured electrical spectrum of the SSB-SC modulation generated at a frequency 915 MHz. The sideband (at 915 MHz) to carrier (at 800 MHz) suppression ratio is 15 dB. In an optical implementation, the RF LO is replaced by an optical carrier and the IF signal is by RF signal that is needed to be phase shifted. In optics, a sideband to carrier suppression ratio of ~20-22 dB was reported experimentally using a DP-MZM architecture [11-12] a decade ago. A suppression of ~40 dB is obtained [15] using a phase shifter and/or variable optical attenuator (VOA) as a trimming means. The phase of the carrier that passes through the lower vector modulator is adjusted by applying a DC voltage in the range of 0.5 V to 2.5 V to the I and Q port of the lower vector modulator using a precision DC source (Agilent B2912A). To adhere the specified ranges, the applied I and Q voltages are defined by:

$$I = 1.5 + \cos(\varphi) \tag{5}$$

$$Q = 1.5 + \sin(\varphi) \tag{6}$$

A phase ramp is applied to the carrier by changing the value of φ, results in equal amount of phase shift at the recovered IF signal at the output of the mixer. Figure 3(c) shows the electrical spectrum of the measured carrier for a particular combination of I and Q values. A similar length of semi rigid RF cable is used to connect the two vector modulators

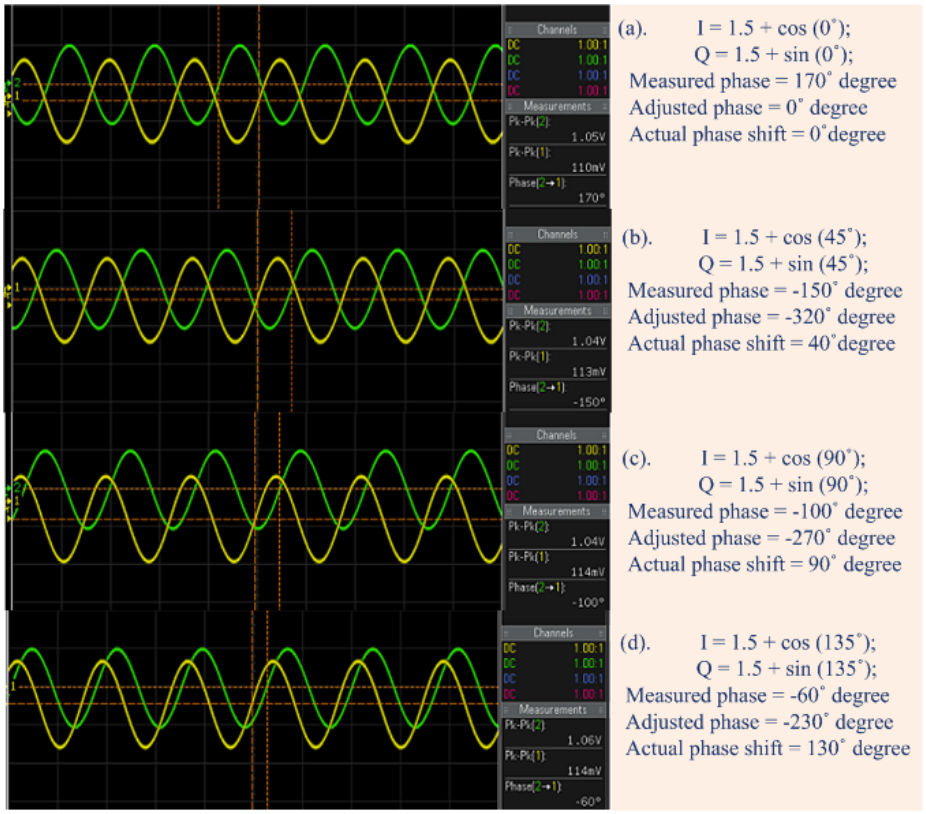

Fig. 4. Screen image of the oscilloscope showing the phase difference between the generated RF signal and a reference signal for various target phase shift as input; (a) target phase shift 0˚; (b) target phase shift 45˚; (c) target phase shift 90˚ and (d) 135˚ respectively.

with the double balanced mixer, making sure that the path lengths remain same. In a photonic integrated circuit, this can easily be achieved. The output of the mixer is then passed through a low pass filter (LPF) to the digital storage oscilloscope. Since, there is no vector network analyzer (VNA), the length of connection between the LPF and oscilloscope is kept to a minimum so that the actual phase at the output of the LPF is measured by the oscilloscope. Nevertheless, an error of ~2-3˚ is added due to the different path lengths. Figure 4 and 5 shows the screen image of the measured phase difference between the recovered IF signal and the reference signal for various input phase values φ.

Table 1. Experimental details of the applied input voltage (target phase), measured phase, actual phase shift and peak to peak voltage of the recovered IF signal.

Input voltage (volts)		Target phase degree	Phase shift with respect to reference signal (degree)	Adjusted phase (degree)	Actual phase shift (degree)	Amplitude $V_{peak-peak}$ (mV)
I-port	Q-port					
2.5	1.5	0	170	$170-170=0$	0	110
2.406	1.922	25	-170	$-170-170=-340$	20	111
2.207	2.207	45	-150	$-150-170=-320$	40	113
1.5	2.5	90	-100	$-100-170=-270$	90	114
0.793	2.207	135	-60	$-60-170=-230$	130	114
0.5	1.5	180	-19	$-19-170=-189$	171	112
0.633	1.0	210	10	$10-170=-160$	200	110
0.793	0.793	225	29	$29-170=-141$	219	109
1	0.633	245	50	$50-170=-120$	240	110
1.5	0.5	270	80	$80-170=-90$	270	112
2.207	0.793	315	120	$120-170=-50$	310	110
2.406	1.077	335	140	$140-170=-30$	330	110

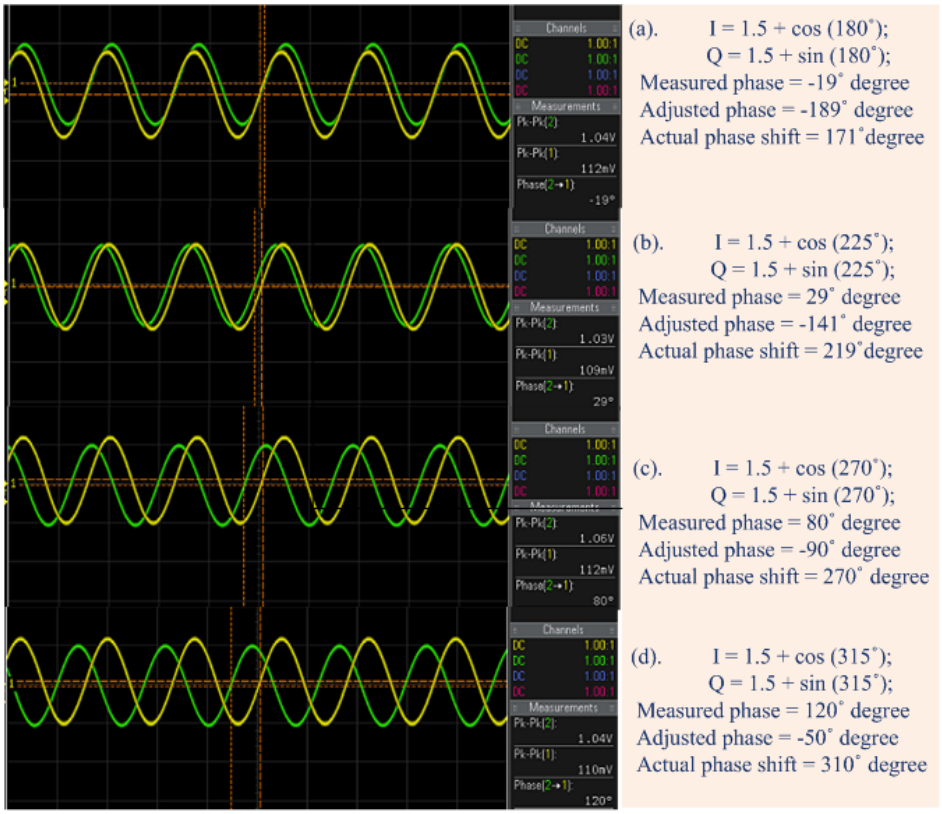

Fig. 5. Screen image of the oscilloscope showing the phase difference between the generated RF signal and a reference signal for various target phase shift as input; (a) target phase shift 180˚; (b) target phase shift 225˚; (c) target phase shift 270˚ and (d) 315˚ respectively.

The measured phase difference is then adjusted by subtracting an equal amount of phase shift from all the measured phase to obtain the actual phase shift. Table 1 shows the details of applied voltage to the I and Q port, measured phase difference and actual phase shift. Figure 6. (a) plots the measured phase shift as a function of applied phase shift (target phase shift). A straight line is obtained using curve fitting which also justify the theoretical prediction. A very small error is obtained between the target phase shift and actual phase shift. In some cases, the measured phase shift is identical to the target shift. Measurement results also verify that the peak to peak amplitude of the recovered IF signal

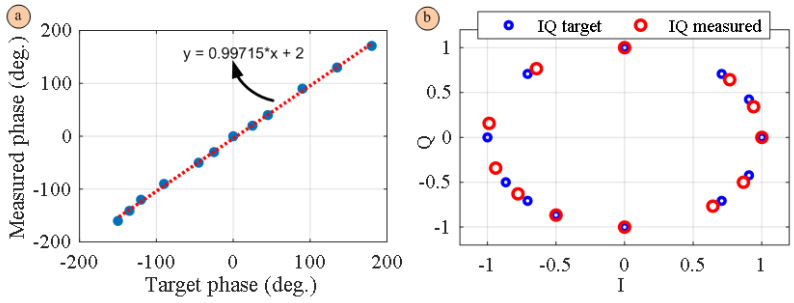

Fig. 6. (a) Relationship between target and measured phase shift; (b) measured I-Q value versus expected I-Q value.

remain almost constant. Figure 6. (b) shows the comparison between expected I-Q values and measured I-Q values. A maximum error of 9-10˚ degree is obtained for two cases. However, the phase measurement using a VNA will

certainly improve the precision of the measurement. Nevertheless, a 360˚-degree rotation is obtained experimentally. The phase trajectory can rotate on the unit circle either way (clockwise or anti clockwise) indefinite amount of times.

4. Conclusion

In summary, a novel photonic technique for obtaining the phase shift of a RF signal is reported with simulation verification. The proposed circuit can function for a wide range of frequencies and it can generate a phase without bound. The circuit may be implemented in practice using a commercially available DP-QPSK modulator. The bandwidth of the operation depends on the bandwidth of the phase modulators that forms the MZM. An experimental verification of the concept is presented using off the shelf low frequency electronics. Results show that a RF phase shift of 360˚ degree or more can be obtained with negligible penalty at the amplitude of the phase shifted signal. Results also show that an SSB-SC modulation having sideband to carrier suppression ratio of only 15 dB or more is good enough for the proposed architecture to function correctly

Funding
No funding.

Acknowledgments
Mehedi Hasan acknowledges the Natural Sciences and Engineering Research Council of Canada (NSERC) for their support through the Vanier Canada Graduate Scholarship program. Trevor J. Hall is also grateful to the University of Ottawa for their support of a University Research Chair.

Disclosures
The authors declare no conflicts of interest.

References
1. J. Han, B. Seo, S. Ku. Kim, H. Zhang and H. R. Fetterman, “Single-chip integrated electro-optic polymer photonic RF phase shifter array,” J. Lightwave Technol. 21, 3257-3261, (2003).
2. T. Niu, X. Wang, E. H. W. Chan, X. Feng and B. O. Guan, “Dual-polarization dual-parallel MZM and optical phase shifter-based microwave photonic phase controller,” IEEE Photonics J. 8, 1-14, (2016).
3. S. Zhu, M. Li, X. Wang, N. Hua Zhu, and W. Li, “1 × N hybrid radio frequency photonic splitter based on a dual-polarization dual-parallel Mach Zehnder modulator,” Optics Comm. 431, 10-13, (2019).
4. G. Li, Y. Xiang and S. Pan, “Wideband optical cancellation of RF interference with phase change,” 2017 16th International Conference on Optical Communications and Networks (ICOCN), Wuzhen, 2017, pp. 1-3.
5. T. Li, E. H. W. Chan, X. Wang, X. Feng and B. Guan, “All-optical photonic microwave phase shifter requiring only a single DC voltage control,” IEEE Photonics J. 8, 1-8, (2016).
6. E. H. W. Chan, W. Zhang, and R. A. Minasian, “Photonic RF phase shifter based on optical carrier and RF modulation sidebands amplitude and phase control,” J. Lightwave Technol. 30, 3672-3678 (2012).
7. X. Wang, T. Niu, E. H. W. Chan, X. Feng, B. Guan and J. Yao, “Photonics-based wideband microwave phase shifter,” IEEE Photonics J. 9, 1-10, (2017).
8. C. Porzi, G. Serafino, M. Sans, F. Falconi, V. Sorianello, S. Pinna, J. E. Mitchell, M. Romagnoli, A. Bogoni, and P. Ghelfi , “Photonic integrated microwave phase shifter up to the mm-wave band with fast response time in silicon-on-insulator technology,” J. Lightwave Technol. 36, 4494-4500, (2018).
9. J. Dai, Z. Zhao, Y. Zeng, J. Liu, A. Liu, T. Zhang, F. Yin, Y. Zhou, Y. Liu, and K. Xu, “Stabilized optoelectronic oscillator with enlarged frequency-drift compensation range,” IEEE Photon. Technol. Lett. 30, 1289-1292, (2018).
10. R. Maldonado-Basilio, M. Hasan, H, Nikkah, S. Abdul-Majid, R. Gumeri, F. Lucarz, J. Tocnaye, and T. J. Hall, “Electro-optic up-conversion mixer amenable to photonic integration,” J. Mod. Optics 62, 1405-1411, (2015).
11. H. Yamazaki, T. Saida, T. Goh, A. Mori, and S. Mino, “Dual-carrier IQ modulator with a complementary frequency shifter,” Opt. Express 19, B69-B74 (2011).
12. C. W. Chow, C. H. Wang, C. H. Yeh, and S. Chi, “Analysis of the carrier-suppressed single-sideband modulators used to mitigate Rayleigh backscattering in carrier-distributed PON” Opt. Express 19, 10973-10978, (2011).
13. Wen-Jr Jiang, Chun-Ting Lin, Chung-hung Ho, Chia-Chien Wei, Po-Tsung Shih, Jason (Jyehong) Chen, and Sien Chi, “Photonic vector signal generation employing a novel optical direct-detection in-phase/quadrature-phase up conversion,” Opt. Lett. 35, 4069-4071 (2010).
14. H. Yamazaki, H. Takahashi, T. Goh, Y. Hashizume, T. Yamada, S. Mino, H. Kawakami, and Y. Miyamoto, “Optical modulator with a near-linear field response,” J. Lightwave Technol.34, 3796-3802 (2016).
15. H. Yamazaki, T. Saida, T. Goh S. Mino, M. Nagatani, H. Nosaka, K. Murata, “Dual-carrier dual-polarization IQ modulator using a complementary frequency shifter,” IEEE J. Selec. Top. Quantum Electron. 19 (6), 3400208, (2013).

CHAPTER 6

Conclusion

The transition from incoherent to coherent optical systems is a technological revolution that remains in progress in the fields of optical communications and microwave-photonics. Compared to RF wireless systems, it is far more challenging to implement coherent optical systems since the relative path lengths must be controlled at the level of $\sim 1\ nm$ (for a vacuum optical wavelength ~ 1 μm) if the phase is to be well defined within a complex system. Fortunately, another technological revolution is the migration from discrete components to photonic integrated components, which with continuing advancements in microfabrication can deliver path-length control at the requisite level. This thesis provides new insight and advancement in the field of coherent optical signal processor architecture through the design, verification by simulation and, test and measurement of some prototypes. All the contributions reported in this thesis make use of commercially viable technology that is amenable to integration. The applications of this thesis research range from RF photonics to optical communications.

6.1 Summary of findings and contributions

A universal coherent electro-optic circuit architecture that generates a frequency comb consisting of *N* spatially separated orders has been described in Chapter 2. The circuit consists of a 1 × N splitter that feeds light into a parallel array of electro-optic phase modulators each driven from the same RF source with a progressive phase shift with increment of 2π/N. The output of the phase modulator array is processed by an N × N optical DFT. The circuit is not limited to a DFT and any linear optical transformation may be substituted. The circuit subsumes many prior RF photonic circuit architectures given an appropriate choice of output port(s) and dimension *N*, although the principal application envisaged in this work is phase correlated subcarrier generation. The predictions of a transfer matrix model of the circuit operation have been validated by simulations performed using an industry standard software tool for the dimension $N = 4$. A novel extension of the circuit architecture is also presented, that replaces the 4×4 DFT network using the combination of a properly chosen phase shifter and a single 4×4 MMI coupler. The

experimental verification is also provided. A photonic integrated circuit based on silicon photonics technology having eight parallel phase shifters connected between 4×4 MMI at the input and output was configured for the target application. Experimental results verify the theoretical predictions but the unwanted harmonics suppression ratio specifically the carrier suppression is inadequate. There are two reasons responsible. Firstly, the phase shifters are driven at a low modulation index due to the unavailability of a high-power RF signal source having four output channels. At low modulation index, the carrier amplitude is considerably stronger than $\pm 1^{st}$ harmonics, and consequently, although the carrier is suppressed substantially by the circuit, the carrier breakthrough due to fabrication errors remains high in magnitude relative to the $\pm 1^{st}$ harmonics. Secondly, there is no tuning element in the circuit to compensate the MMI output power imbalances and phase errors due to fabrication process errors.

Two original circuit architectures for on-chip spectral monitoring with sub-GHz resolution over the entire C-band have been presented in Chapter 3. Reliable spectral measurement across the optical communications network is a key enabling technology. Complete knowledge of the state of the network is a prerequisite to enabling SDN-EON-AI to make effective use of colour-less, direction-less, contention-less, grid-less, filter-less, gap-less ROADM, flexible channels centre frequencies and width, flexible sub-carriers in super-channels, flexible modulation formats and forward error control coding transponders, and impairment-aware wavelength routing and spectral assignment. The first architecture described consists of three stages. The first stage is a tunable ring resonator (RR) that defines the resolution. The third stage is an arrayed waveguide grating (AWG) that isolates one RR resonance within each of its channels. The second stage uses an MZI to form a coherent superposition of two interleaved AWG channel spectra corresponding to a pair of AWG input ports; establishing gang tuning of the RR and AWG to retain the RR resonance at the center of the AWG channel passband. The second architecture described is a refinement of the first architecture in which the coherent superposition of a pair of AWG input channels is replaced by the incoherent superposition of pairs of AWG output channels. This eliminates the MZI stages, and as a consequence the spectrometer does not require any control of the inter-stage optical path length, which renders the spectrometer more robust to fabrication process variations. Detailed simulation verification is provided using constructor design data. Simulation results verify that the spectrum monitoring can be performed over the entire C-band with peak power flatness $\sim 1 \rightarrow 1.25$ dB. A further modification of the second architecture is proposed to provide a completely flat

spectral response with zero adjacent channel crosstalk, at least in theory. The CMOS compatible Si_3N_4 platform is selected for fabrication due to its low loss and maturity.

An original circuit architecture for SSB/I-Q modulation based on a two-stage cascaded MZM has been described in Chapter 4. SSB/I-Q modulator is at the heart of coherent optical communication and coherent radio-over-fibre (RoF) technology for performing multi-level modulation and single side band modulation. The proposed design is advantageous by 6 dB in terms of conversion efficiency compared to the functionally equivalent single stage parallel circuit. The experimental verification is provided using a three-stage cascaded circuit fabricated for high baud rate PAM transmission. The experimental result shows that, the circuit can perform SSB modulation with a side harmonic suppression ratio of at least 15 dB or more. Furthermore, a new architecture is proposed to implement the same functionality but using polarization optics. The residual carrier and other sub-harmonic suppression ratios are improved as light travels along only one physical path.

A novel photonic technique of generating a broadband RF phase shift has been described in Chapter 5. A precise and broadband RF phase shifter is needed for phased array antenna systems to support high speed wireless communication and radar applications. The circuit architecture consists of two parallel DP-MZM with outputs combined by a photodetector. The circuit requires no additional control or filter for proper operation. Furthermore, the linearity of the phase shifter remains valid for a wide range of frequencies. The proposed phase shifter can generate any phase without bound. The complex transmission of the phase shifter follows a trajectory that may encircle the origin in either direction an arbitrary number of times. An experimental verification of the concept is presented using off the shelf RF electronics.

In summary, the thesis contributes to the advancement of the field through the conception, theoretical modelling, verification by simulation, and experimental demonstration of original photonic processor circuit architectures amenable to photonic integration that include:

- a universal RF-photonic processor that garners into a systematic formalism the ad hoc design processes of much of the prior art, elucidates the fundamental operating principles, and extends the applications inter alia to phase correlated sub-carrier generation for Tbit/s data transfer using optical orthogonal frequency division multiplexing (OFDM);
- an optical power monitor (OPM) that provides for the first time a panoramic view of the power spectrum across the entire C-band with <1GHz resolution bandwidth;

- a unique energy efficient I-Q or SSB modulator;
- a broadband high frequency RF phase shifter that can generate for the first time a continuous phase without bound.

In conclusion, electro-photonic technology offers a means to accommodate ever increasing capacity demands of applications as data rates outpace (in speed, low energy consumption, weight, size etc.) all-electronic solutions. The photonic circuit architectures introduced by this thesis belong to a new class of coherent optical processor made increasingly practical by advances in microfabrication and algorithms [59]. The most pressing need found in this work is the development of:

(i) drift-free, negligible power consumption on-chip phase bias trimmers required to set the operating point (i.e. provide the actuators / controls of a plant);

(ii) on-chip sensors to monitor the state of the system;

(iii) on-chip controllers and algorithms to initialize and maintain (online) the quiescent state of these fundamentally analogue coherent optical systems.

6.2 Suggestions for future work

In addition to the pressing needs identified, the research thesis may be advanced further through:

- the photonic integrated circuit implementation of:
  - the universal RF photonic processor introduced in Chapter 2 using both modulator and delay line arrays up to initially the dimension $N = 8$ and then beyond.
  - the spectrometer architecture based on three (3) AWG introduced in Chapter 3 as it offers robust performance: sub-GHz resolution; wideband operation; flat spectral response; compactness; and essentially zero crosstalk.
  - the polarization insensitive spectrometer introduced in Chapter 3.
  - the two-stage cascaded circuit architecture for SSB modulation introduced in Chapter 4 and found to offer a 3 dB electrical and 3 dB optical advantage over a functionally equivalent single stage parallel circuit (i.e. a DP-MZM). The inherent advantages were verified by simulation but only implementation using linear electro optic modulator (for example $LiNbO_3$ on Si or Si_3N_4) can provide an apple to apple comparison needed to evaluate the extent to which the advantage can be realized in practice. In addition, research on for high baud rate transmission using cascaded MZM can be advanced.

- the RF photonic phase shifter introduced in Chapter 5. The proposed circuit architecture can be implemented using commercially available DP-QPSK modulator but fabrication permits custom design to address drift-free phase bias, increasing the GMZI dimension beyond N=4 to decrease insertion loss and improve linearity, and alternative methods of linearization.

- research on circuit symmetries and emerging trimming algorithms to approach perfect photonic systems using imperfect components, including online machine learning approaches to quiescent operating point control with minimal disturbance to concurrent operation.

Bibliography

[1] M. Reck, A. Zeilinger, H. J. Bernstein, and P. Bertani, "Experimental realization of any discrete unitary operator," Phys. Rev. Lett., 73, 58-61 (1994).

[2] J. Carolan, C. Harrold, C. Sparrow, E. Martín-López, N. J. Russell, J. W. Silverstone, P. J. Shadbolt, N. Matsuda, M. Oguma, M. Itoh, G. D. Marshall, M. G. Thompson, J. C. F. Matthews, T. Hashimoto, J. L. O'Brien, and A. Laing, "Universal linear optics," Science 349 (6249), 711-716 (2015).

[3] D. Miller, "Perfect optics with imperfect components," Optica 2(8), 747-750 (2015).

[4] M. Izutsu, S. Shikama, T. Sueta, "Integrated optical SSB modulator / frequency shifter," IEEE J. Quantum Electron. 17, 2225-2227 (1981).

[5] G. H. Smith, D. Novak, and Z. Ahmed, "Overcoming chromatic-dispersion effects in fiber-wireless systems incorporating external modulators," IEEE Trans. Microwave Theory Tech. 45, 1410-1415 (1997).

[6] A. Wen, M. Li, L. Shang, and Y. Chen, "A novel optical SSB modulation scheme with interfering harmonics suppressed for ROF transmission link," Opt. Laser Technol. 43, 1061-1064 (2011).

[7] C. W. Chow, C. H. Wang, C. H. Yeh, and S. Chi, "Analysis of the carrier-suppressed single-sideband modulators used to mitigate Rayleigh backscattering in carrier-distributed PON," Opt. Express 19, 10973-10978 (2011).

[8] M. Hasan, R. Maldonado-Basilio, T. J. Hall, "Comments on X. Yin, A. Wen, Y. Chen, and T. Wang, "Studies in an optical millimeter-wave generation scheme via two parallel dual-parallel Mach-Zehnder modulators," J. Mod. Opt. 62, 581-583 (2015).

[9] P.-T. Shih, J. Chen, C.-T. Lin, W.-J. Jiang, H.-S. Huang, P.-C. Peng, and S. Chi, "Optical millimeter-wave signal generation via frequency 12-tupling," J. Lightwave Technol. 28, 71-78 (2010).

[10] H. Yamazaki, T. Saida, T. Goh S. Mino, M. Nagatani, H. Nosaka, K. Murata, "Dual-carrier dual-polarization IQ modulator using a complementary frequency shifter," IEEE J. Sel. Top. Quantum Electron. 19, 3400208 (2013).

[11] R. Maldonado-Basilio, M. Hasan, R. Guemri, F. Lucarz, and T. J. Hall, "Generalized Mach–Zehnder interferometer architectures for radio frequency translation and multiplication: suppression of unwanted harmonics by design," Opt. Comm. 354, 122-127 (2015).

[12] M. Hasan, R. Maldonado-Basilio, and T. J. Hall, "A dual-function photonic integrated circuit for frequency octo-tupling or single-side-band modulation," Opt. Lett. 40, 2501-2504 (2015).

[13] R. Maldonado-Basilio, M. Hasan, H, Nikkhah, S. Abdul-Majid, R. Gumeri, F. Lucarz, J. Tocnaye, and T. J. Hall, "Electro optic up-conversion mixer amenable to photonic integration," J. Mod. Opt. 62, 1405-1411 (2015).

[14] Y. Ma, Q. Yang, Y. Tang, S. Chen, and W. Shieh, "1-Tb/s single-channel coherent optical OFDM transmission over 600-km SSMF fiber with subwavelength bandwidth access," Opt. Express 17, 9421-9427 (2009).

[15] K. Takiguchi, and T. Miwa, "Integrated-optic OFDM signal multiplexer composed of optical IFFT circuit," Electron. Lett. 51, 505-506 (2015).

[16] K. Takiguchi, M. Oguma, H. Takahashi and A. Mori, "Integrated-optic eight-channel OFDM demultiplexer and its demonstration with 160 Gbit/s signal reception," Electron. Lett. 46, 575-576 (2010).

[17] K. Takiguchi, T. Kitoh, A. Mori, M. Oguma, and H. Takahashi, "Integrated-optic OFDM demultiplexer using slab star coupler based optical DFT circuit," 36th European Conference and Exhibition on Optical Communication (ECOC), Torino, 2010, pp. 1-3.

[18] W. Li, X. Liang, W. Ma, T. Zhou, B. Huang, and D. Liu, "A planar waveguide optical discrete Fourier transformer design for 160 Gb/s all-optical OFDM systems," Opt. Fiber Technol. 16, 5-11 (2010).

[19] B. Kyotoku, L. Chen, and M. Lipson, "Sub-nm resolution cavity enhanced micro-spectrometer," Opt. Express 18, 102-107 (2010).

[20] G. Yurtsever, and R. Baets, "Integrated spectrometer on silicon on insulator," 16th Annual Symposium of the IEEE photonics, Ghent, Belgium, 273-276 (2011).

[21] E. Ryckeboer, A. Gassenq, M. Muneeb, N. Hattasan, S. Pathak, L. Cerutti, J.B. Rodriguez, E. Tournié, W. Bogaerts, R. Baets, and G. Roelkens, "Silicon-on-insulator spectrometers with integrated GaInAsSb photodiodes for wide-band spectroscopy from 1510 to 2300 nm," Opt. Express 21, 6101-6108 (2013).

[22] X. Ma, M. Li and J. He, “CMOS-compatible integrated spectrometer based on echelle diffraction grating and MSM photodetector array,” IEEE Photonics J. 5, 6600807-6600807 (2013).

[23] Z. Xia, A. A. Eftekhar, M. Soltani, B. Momeni, Q. Li, M. Chamanzar, S. Yegnanarayanan, and A. Adibi, “High resolution on-chip spectroscopy based on miniaturized microdonut resonators,” Opt. Express 19, 12356-12364 (2011).

[24] C. Xiang, P.A. Morton, J. Khurgin, C. Morton, and J. E. Bowers, “Widely tunable Si3N4 triple-ring and quad-ring resonator laser reflectors and filters,” IEEE 15th International conference on group IV photonics, Cancun, Mexico, 1-2 (2018).

[25] Y. Li, J. Li, H. Yu, H. Yu, H. Chen, S. Yang, and M. Chen, “On-chip photonic microsystem for optical signal processing based on silicon and silicon nitride platforms,” Adv. Opt. Technol. 7, 81-101, (2018).

[26] M. Kita, H. lin, A. Agarwal, K. Richardson, I. Luzinov, T. Gu, and J. Hu, “On-chip infrared spectroscopic sensing: Redefining the benefits of scaling,” IEEE J. Sel. Topics in Quantum Electron. 23, 340-349, (2017).

[27] Elham Heidari, Xiaochuan Xu, Chi-Jui Chung, and Ray T. Chen, “On-chip Fourier transform spectrometer on silicon-on-sapphire,” Opt. Lett. 44, 2883-2886 (2019).

[28]C. G. H. Roeloffzen , M. Hoekman , E. J. Klein, L. S. Wevers, R. B. Timens , D. Marchenko, D. Geskus, R. Dekker, A. Alippi, R. Grootjans, A. V. Rees , R. M. Oldenbeuving, J. P. Epping, R. G. Heideman, K. Wörhoff, A. Leinse, D. Geuzebroek , E. Schreuder, P. W. L. Van Dijk, I. Visscher, C. Taddei , Y. Fan , C. Taballione, Y. Liu , D. Marpaung , L. Zhuang , M. Benelajla, and K.-J. Boller, “Low-loss Si3N4 TriPleX optical waveguides: Technology and applications overview,” IEEE J. Sel. Topics in Quantum Electron., 24, 1-21, (2018).

[29] L. Zhuang, D. Marpaung, M. Burla, W. Beeker, A. Leinse, and C. Roeloffzen, “Low-loss, high-index-contrast Si3N4/SiO2 optical waveguides for optical delay lines in microwave photonics signal processing,” Opt. Express, 19, 23162-23170, (2011).

[30] Y. Xie, L. Zhuang, and A. Lowery, “Picosecond optical pulse processing using a terahertz-bandwidth reconfigurable photonic integrated circuit,” Nanophotonics 7, 837-852, (2018).

[31] D. Seyringer, M. Sagmeister, A. Maese‑Novo, M. Eggeling, E. Rank, P. Muellner, R. Hainberger, W. Drexler, M. Vlaskovic, H. Zimmermann, G. Meinhardt, and J. Kraft,

"Technological verification of size‐optimized 160‐channel silicon nitride‐based AWG-spectrometer for medical applications," Appl. Phys. B, 125, 88, (2019).

[32] M.-T. Zhou, A. B. Sharma, Z.-H. Shao, and M. Fujise, "Optical single-sideband modulation at 60 GHz using electro-absorption modulators," in International Topical Meeting on Microwave Photonics, Seoul, Korea, 2005, p. 121-124.

[33] D. Zibar, R. Sambaraju, A. Caballero Jambrina, R. Alemany, J. Herrera, I. Tafur Monroy, "16 Gb/s QPSK wireless-over-fibre link in 75-110 GHz band employing optical heterodyne generation and coherent detection," presented at ECOC, Torino, Italy, 2010.

[34] A. Caballero, D. Zibar, R. Sambaraju, J. Marti, I. T. Monroy, "High-capacity 60 GHz and 75-110 GHz band links employing all-optical OFDM generation and digital coherent detection," J. Light. Technol., 30, 147-155, (2012).

[35] G. H. Smith, D. Novak, and Z. Ahmed, "Technique for optical SSB generation to overcome dispersion penalties in fibre-radio systems," Electron. Lett. 33, 74-75 (1997).

[36] J. Yu, Z. Jia, L. Yi, Y. Su, G.-K. Chang, and T. Wang, "Optical millimeter-wave generation or up-conversion using external modulators," IEEE Photon. Technol. Lett., 18, 265-267 (2006).

[37] J.-G. Zhao, Z.-J. Liu, X.-L. Liu, T. Shang, and P. Yue, "Generation of radio signals using a novel Mach-Zehnder modulator with four arms," Opt. Commun. 282, 4353-4357 (2009).

[38] J.-G. Zhao, Z. J. Liu, X.-L. Liu, T. Shang, and P. Yue, "Optimisation of carrier-to-sideband ratio by triple-arm Mach-Zehnder modulators in radio-over-fibre links," IET Optoelectron. 4(5), 183-188 (2010).

[39] W. Li, and J. Yao, "Investigation of photonically assisted microwave frequency multiplication based on external modulation," IEEE Trans. Microw. Theory Tech., 58, 3259-3268 (2010).

[40] M. Hasan, and T. J. Hall, "A photonic frequency octo-tupler with reduced RF drive power and extended spurious sideband suppression," Opt. Laser Technol. 81, 115-121(2016).

[41] A. Simard, B. Filion, D. Patel, D. Plant, and S. LaRochelle, "Segmented silicon MZM for PAM-8 transmissions at 114 Gb/s with binary signaling," Opt. Express 24, 19467-19472, (2016).

[42] C. Wilkes, X. Qiang, J. Wang, R. Santagati, S. Paesani, X. Zhou, D. Miller, G. Marshall, M. Thompson, and J. O'Brien, "60 dB high-extinction auto-configured Mach–Zehnder interferometer," Opt. Lett. 41, 5318-5321 (2016).

[43] J. Han, B. Seo, S. Ku. Kim, H. Zhang and H. R. Fetterman, "Single-chip integrated electro-optic polymer photonic RF phase shifter array," J. Lightwave Technol. 21, 3257-3261, (2003).

[44] T. Niu, X. Wang, E. H. W. Chan, X. Feng and B. O. Guan, "Dual-polarization dual-parallel MZM and optical phase shifter-based microwave photonic phase controller," IEEE Photonics J. 8, 1-14, (2016).

[45] S. Zhu, M. Li, X. Wang, N. Hua Zhu, and W. Li, "1 × N hybrid radio frequency photonic splitter based on a dual-polarization dual-parallel Mach Zehnder modulator," Optics Comm. 431, 10-13, (2019).

[46] G. Li, Y. Xiang and S. Pan, "Wideband optical cancellation of RF interference with phase change," 2017 16th International Conference on Optical Communications and Networks (ICOCN), Wuzhen, 2017, pp. 1-3.

[47] T. Li, E. H. W. Chan, X. Wang, X. Feng and B. Guan, "All-optical photonic microwave phase shifter requiring only a single DC voltage control," IEEE Photonics J. 8, 1-8, (2016).

[48] E. H. W. Chan, W. Zhang, and R. A. Minasian, "Photonic RF phase shifter based on optical carrier and RF modulation sidebands amplitude and phase control," J. Lightwave Technol. 30, 3672-3678 (2012).

[49] X. Wang, T. Niu, E. H. W. Chan, X. Feng, B. Guan and J. Yao, "Photonics-based wideband microwave phase shifter," IEEE Photonics J. 9, 1-10, (2017).

[50] C. Porzi, G. Serafino, M. Sans, F. Falconi, V. Sorianello, S. Pinna, J. E. Mitchell, M. Romagnoli, A. Bogoni, and P. Ghelfi , "Photonic integrated microwave phase shifter up to the mm-wave band with fast response time in silicon-on-insulator technology," J. Lightwave Technol. 36, 4494-4500, (2018).

[51] J. Dai, Z. Zhao, Y. Zeng, J. Liu, A. Liu, T. Zhang, F. Yin, Y. Zhou, Y. Liu, and K. Xu, "Stabilized optoelectronic oscillator with enlarged frequency-drift compensation range," IEEE Photon. Technol. Lett. 30, 1289-1292, (2018).

[52] T. J. Hall and M. Hasan, "Universal discrete Fourier optics RF photonic integrated circuit architecture," Optics Exp. 24,7600-7610 (2016).

[53] M. Hasan, D. Sun, P. Liu and T. J. Hall, “Towards a universal RF photonic integrated circuit architecture for microwave applications,” 37th Progress in Electromagnetics Research Symposium (PIERS), Shanghai, China 8-11 August (2016).

[54] M. Hasan, G. M. Hasan and T. J. Hall, “Experimental realization of a universal RF photonic integrated circuit,” submitted to Optics Communication (2020).

[55] M. Hasan, M. Rad, G.M. Hasan, P. Liu, P. Dumais, E. Bernier and T. J. Hall, “Ultra-high resolution wideband On-chip spectrometer,” IEEE Photonics J. 12, 1-17 (2020).

[56] M. Hasan, and T. Hall, “Cascade photonic integrated circuit architecture for electro-optic I-Q / SSB modulation or frequency conversion,” Opt. Lett. 40, 5038-5041 (2015).

[57] M. Hasan, O. Jafari, X. Guan, L. A. Rusch, S. Larochelle, and T. J. Hall, “Experimental demonstration of SSB modulation/ frequency conversion using cascaded silicon MZM,” IEEE Photon. Technol. Lett. 32, 1147-1150 (2020).

[58] M. Hasan and T. J. Hall, “Complex modulation using tandem polarization modulators,” J. Mod. Opt. 64, 2268-2272 (2017).

[59]W. Bogaerts, D. Pérez, J. Capmany, D. A. B. Miller, J. Poon, D. Englund, F. Morichetti, and A. Melloni, “Programmable photonic circuits,” Nature 586, 207–216(2020).